MACRO- AND MICRO-MECHANICS OF MIXED-MODE DYNAMIC FRACTURE OF CONCRETE

PART I
MICRO-MECHANIC ANALYSIS

Chang-Te Yu
Zhikai Guo
A.S. Kobayashi
Department of Mechanical Engineering
University of Washington
Seattle, WA 98195

Neil M. Hawkins
Department of Civil Engineering
University of Illinois at Urbana-Champaign
Urbana, IL 61801-2397

Prepared for

Air Force Office of Scientific Research
Bolling Air Force Base
Washington, D.C. 20332-6448

Final Report on AFOSR Contract 91-0128

February 14, 1993

Distribution Unlimited:

REPORT DOCUMENTATION PAGE

Form Approved
OMB No. 0704-0188

1. AGENCY USE ONLY (Leave blank)	2. REPORT DATE	3. REPORT TYPE AND DATES COVERED
	14 February 1993	Final Report 15 Dec.'90 thru 14 Dec.'92

4. TITLE AND SUBTITLE
Macro- and Micro-Mechanics of Mixed-Mode Dynamic Fracture of Concrete, Part I Micro-Mechanic Analysis

5. FUNDING NUMBERS
AFOSR
91-0128

6. AUTHOR(S)
Chang-Te Yu, Zhikai Guo, A.S. Kobayashi and N.M. Hawkins

7. PERFORMING ORGANIZATION NAME(S) AND ADDRESS(ES)
University of Washington
Deptment of Mechanical Engineering
Seattle, WA 98195

8. PERFORMING ORGANIZATION REPORT NUMBER
UWA/DME/TR 90-1

9. SPONSORING/MONITORING AGENCY NAME(S) AND ADDRESS(ES)
AFOSR/NA
Building 410
Bolling AFB, DC 20332-6448

10. SPONSORING/MONITORING AGENCY REPORT NUMBER

11. SUPPLEMENTARY NOTES

12a. DISTRIBUTION/AVAILABILITY STATEMENT
Unclassified/Unlimited

12b. DISTRIBUTION CODE

13. ABSTRACT (Maximum 200 words)

A hybrid experimental-numerical procedure was used to analyze the micro-mecnanics of the mixed-mode, static and dynamic fracture of a concrete three-point bend specimen with an offset precrack. Four/two beam moire interferometry was used to record simultaneously separating horizontal and vertical displacements associated with stable/rapid growth. An elasto-static/elasto-dynamic finite element code was executed in its propagation mode with assumed crack closure stress (CCS) versus crack opening displacement (COD) and crack shearing stress (CSS) versus crack sliding displacement (CSD) relations which were adjusted to match the computed and measured COD's and CSD's. The resultant CCS versus COD and the CSS versus CSD relations were then used to compute the dissipated energy in the FPZ. This energy dissipation rate in the FPZ accounted for about 80% of the total energy release rate throughout the dynamic fracture process. This study also showed that the strain energy released at the crack tip and the dissipated energy in the fracture process zone after crack kinking are due mainly to mode I crack tip deformation.

14. SUBJECT TERMS
Concrete fracture, mixed-mode dynamic fracture, fracture process zone, moire interferometry, dynamic finite element analysis.

15. NUMBER OF PAGES

16. PRICE CODE

17. SECURITY CLASSIFICATION OF REPORT	18. SECURITY CLASSIFICATION OF THIS PAGE	19. SECURITY CLASSIFICATION OF ABSTRACT	20. LIMITATION OF ABSTRACT
Unclassified	Unclassified	Unclassified	Unlimited

Research sponsored by the Air Force Office of Scientific Research, Air Force Systems Command, USAF, under grant number, AFOSR 91-0128. The US Government is authorized to reproduce and distribute reprints for Governmental purposes notwithstanding any copyright notation thereon.

ABSTRACT

A hybrid experimental-numerical procedure was used to analyze the micro-mechanics of the mixed mode, dynamic fracture of concrete. For comparison purposes, a static analysis was undertaken simultaneously with the dynamic analysis of mixed mode fracture of three-point bend concrete specimen with an offset precrack. For static analysis, four beam moire interferometry was used to record simultaneously the horizontal and vertical displacements associated with stable crack growth. Due to the limited resolution of the IMACON 790 ultra-high speed camera with an exposure of 2 μs and a framing rate of 100,000 frames/sec., two-beam dynamic moire interferometry was used to record eight sequential moire patterns of either the horizontal or vertical displacements in the dynamic analysis of rapid crack growth. The fracture event, which lasted about 1.5 ms, was represented by a composite record of nine identical dynamic fracture tests with various time delays in triggering the ultra-high speed camera. An elasto-static or elasto-dynamic finite element code was executed in its propagation mode with assumed crack closure stress (CCS) versus crack opening displacement (COD) and crack shearing stress (CSS) versus crack sliding displacement (CSD) relations which were adjusted to match the computed and measured COD's and CSD's. The resultant CCS versus COD and the CSS versus CSD relations were used to compute the dissipated energy in the FPZ. This energy dissipation rate in the FPZ accounted for about 80% of the total energy release rate throughout the dynamic fracture process. This study also showed that the strain energy released at the crack tip and the dissipated energy in the fracture process zone after crack kinking are due mainly to mode I crack tip deformation.

TABLE OF CONTENTS

LIST OF FIGURES

page

page

LIST OF TABLES

page

CHAPTER 1
INTRODUCTION AND OBJECTIVES

1.1 Introduction

Since Hillerborg first advanced the concept of a cohesive zone trailing a growing crack in a concrete fracture specimen [1] to explain the behavior observed for such specimens, this concept has gained in popularity during the past decade [2-5]. This cohesive zone concept, which derives its origin from an idealization of the plastic zone preceding the crack tip in a ductile metal, was based on a postulated fracture process zone (FPZ) where microcracks form and coalesce ahead of a growing traction-free macrocrack. Later studies have, however, related that cohesive zone to the fracture surface immediately behind the crack tip and where aggregate bridging in concrete fracture and grain bridging in fracture of monolithic ceramics restrict crack opening. For mode I fracture, this resistance can be characterized by a crack closure stress (CCS) versus crack opening displacement (COD) relationship, which were inferred from cyclic load and unload tests in the strain-softening portion of a direct tension test [2, 3]. When incorporated into a finite element model, these CCS versus COD relations can be used not only to predict the overall fracture strength but also to simulate the progressive damage process in a concrete structure [5]. Most of the above studies [1,2,4] involved an inverse analysis where a postulated CCS versus COD relation was varied until the computed and measured remote loading parameters, such as the applied load and load-line displacement, coincided. These remote parameters are, however, relatively insensitive to small changes in the CCS versus the COD relation as will be shown later in this report. Experimental studies involving direct measurements of the crack tip parameters are relatively few since the COD in the vicinity of the crack tip is difficult to measure [4, 5, 6] and the CCS cannot be determined directly.

The authors and their colleagues have used a hybrid experimental-numerical procedure to analyze the FPZ associated with stably and rapidly propagating cracks in concrete fracture specimens under a previous AFOSR grant* [5, 7]. For the previous work of the static concrete fracture, a non-singular FPZ model, which assumes no stress singularity at crack tip, was utilized and the maximum tensile strength was used as a fracture criterion. Yon et al [7] recently proposed a singular FPZ model, which assumes a combined K_I — FPZ model. This singular FPZ model was verified by a parabolic crack opening shape observed from moire

* AFOSR Grant 86-0204, 15 June 1986 through 14 December 1989.

interferometry. The results using the singular FPZ model were reported in numerous proceedings and journal publications and will be referred to throughout this report.

Experimental evidences show that mixed mode, i.e. combined modes I and II, crack extension is not possible in brittle metals and polymers. However, aggregate bridging and interlocking forces, which act on the crack surfaces trailing the crack tip, in concrete, influence the otherwise dominant mode I crack tip state of stress and could result in mixed mode crack extension. For example, Swartz et al [8] measured the average total fracture energy under mixed mode concrete fracture and showed that it was "eight to ten times those obtained for mode I tests on the same size concrete beam." On the other hand, Jenq and Shah [9,10] compared the theoretically predicted failure angles using maximum circumferential stress, maximum energy release rate and minimum strain energy density criteria, all of which are based on linear elastic fracture mechanics (LEFM), with those measured experimentally in three-point bend and four point shear mixed mode tests of concrete fracture specimens and concluded that the differences were indistinguishable. LEFM with modification was also used by Davies [11] to study shear fracture of symmetrically notched mortar cubes and by Wong and Miller [12] to study mixed mode fracture of early aged concrete beam specimens. Their results indicated that mode I crack propagation prevailed in *concrete fracture* specimens with mixed modes I and II loading. Using mixed-mode fracture tests of double-edge notched concrete specimens, Nooru-Mohamed and van Mier [13] observed shear softening thus contradicting Walraven [14] and Reinhardt and Walraven [15] who reported increased interface shear with increased slip in concrete.

In all of the foregoing studies, the starter crack was a machined notch which was subjected to either pure mode I or mixed modes I and II loading. Aggregate bridging and interlocking in the fracture process zone (FPZ), which trails the natural crack tip, would only be possible after growth of the crack from the machined notch. Without the influence of the FPZ, the crack would otherwise propagate under the dominant influence of the mode I crack tip stress field as shown by Liaw et al. [16].

The most common mixed mode type fracture in concrete structures is the diagonal tension failure of a reinforced concrete beam. That cracking usually develops from flexural cracks generated by fracture along the tension edge of the beam. Those initial cracks extend perpendicularly from the edge of the beam, with their depths depending on the applied moments, and then kinks only after extending beyond the reinforcement. Since aggregate bridging and interlocking exist in these crack prior to kinking, the kinking angle as well as

subsequent crack extension could be influenced by the resultant interfacial crack closing and shearing forces.

For the past decade, two of the authors have conducted diagonal tension fracture research of concrete beams. The objective of this research was to simulate the fracture in reinforced concrete beams. Such fracture results in kinking or curving cracks. Consequently, mixed mode fracture was generated in these diagonal tension fracture tests.

Finally, dynamic loading of concrete may occur as a result of an airplane landing on a runway, impact loading of a concrete structure by a missile, waves, gas explosions, winds and earthquakes. The dynamic fracture properties of concrete have been studied by many researchers [17-30]. Some researchers [19,20,31,32] suggested that dynamic fracture of concrete, in the absence of crack curving, closely mimics dynamic ductile tearing which reduces the crack driving force and hence the crack velocity in metals and polymers. Such similarity studies suggest that the intense plastic deformation in metals and polymers can be replaced by microcracking, aggregate interlocking and crack bridging in concrete.

1.2 Objectives

The objective of this research is to develop an appropriate experimental and numerical procedures for studying mixed mode dynamic fracture in concrete. This goal was achieved by the following tasks of:

1. Developing an experimental setup for conducting mixed mode dynamic fracture test.
2. Developing a finite element model for simulating dynamic fracture of concrete.
3. Quantifying the energy dissipation mechanisms during mixed mode dynamic fracture.
4. Comparing the static and dynamic fracture behaviors of concrete.
5. Relating crack kinking to the mode I and mode II fracture parameters.

CHAPTER 2
LITERATURE REVIEW

For ideally linear elastic brittle materials, the fracture toughness is a material constant. However, concrete, which exhibits a nonlinear fracture response does not usually yield a constant value of fracture toughness. The nonlinear response of concrete is observed through its well known strain softening response.

In this review, the nonlinear fracture behavior of concrete is first discussed. Mixed mode fracture of concrete and dynamic fracture test methods are then examined. Finally, the displacement, strain, and crack velocity measurement techniques are reviewed.

2.1 Fracture Process Zone (FPZ)

The fracture toughening mechanisms of concrete can be mainly divided into the frontal process zone and the trailing process zone. The irreversible energy dissipation processes occurring in front of the advancing crack include crack deflection and multiple microcracking. The trailing process zone is where force is transferred between crack faces by aggregate interlocking and crack bridging mechanisms behind the crack tip. The trailing process zone is the fracture process zone (FPZ) discussed in this report. Normally the FPZ is modeled by the constitutive relation between crack closure stress and crack opening displacement. The actual fracture behavior of concrete is highly nonlinear [33]. The nonlinear behavior is due to the development of debonding between the aggregates and cement, and the progressive cracking within the cement matrix. Even before the load is applied, there are considerable amount of microcracks existing due to the hydration process and dry shrinkage of the hardened concrete.

A typical load-displacement curve of a three-point bend concrete fracture specimen is shown in Figure 1. A meaningful stress-deformation relation is difficult to obtain from a direct tension test since the measured average deformation of the tensile specimen has little physical significance in the presence of the localized fracture zone. After reaching the peak load, the load curve drops smoothly in contrast to a linear elastic fracture mechanics (LEFM) behavior of a fracture specimen, where the load drops suddenly. This nonlinear behavior is called strain softening in contrast to the strain hardening curve of metal which is also shown in Figure 1. Actually, "softening" may be a misnomer, for it is this mechanism that provides "toughening" to the material's fracture resistance.

Cedolin and his co-workers [34] found that concrete failed at a low average strain but that locally high strains existed in the specimen due to a non-uniform strain distribution.

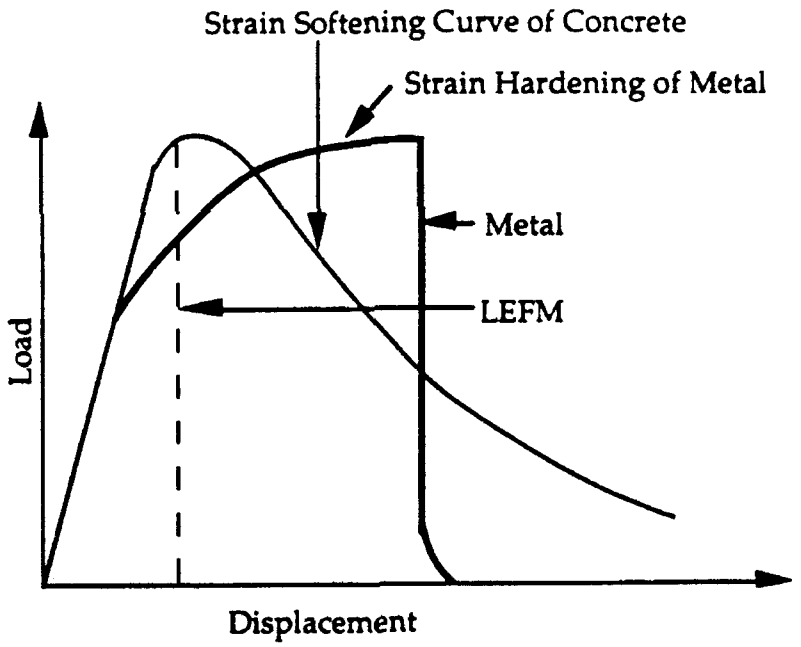

Figure 1. Comparison of the Load-Displacement Curves for a Strain Softening Concrete (Fine Line), Metal (Thicker Line), and LEFM (Dash Line).

2.2 Fracture Models

Kaplan [35] conducted a pioneering fracture experimental study of concrete and found that the crack extension force was twelve times as large as that estimated from the surface energy. He attributed the variance of the crack extension force to slow crack growth before fracture. Glucklick [36] extended Kaplan's work and reasoned that the crack extension force was much larger than the surface energy because fracture of concrete was not limited to a single crack propagation. Instead, a multitude of microcracks formed in the highly stressed zone, and therefore the true fracture surface area was much greater than the apparent one. Glucklick also showed that aggregates in concrete acted as crack arrestors because they increased the energy demand or diverted the crack under higher energy. The slope of fracture energy versus crack length curve increased until a critical crack length was reached. This suggests that the microcracking process zone had to be fully developed before unstable crack propagation occurred.

2.2.1 Micro Crack Softening Model

Hillerborg [37] was the first to suggest that the actual flexural behavior of concrete could be attributed to the following four process zones as shown in Figure 2:

1. Elastic zone where linear elastic mechanics is applicable.
2. Microcracking zone where the stiffness of the fracture zone decreases suddenly due to increasing microcracks.
3. Microcrack branching zone where multiple microcracks coalesce into one macro-crack and the stiffness of the fracture zone decreases slowly.
4. Traction free zone where no stress transfer occurs across the fracture surface.

Using this micro-crack softening model, Hollerborg then reproduced the load versus displacement curve with strain softening in a concrete specimen.

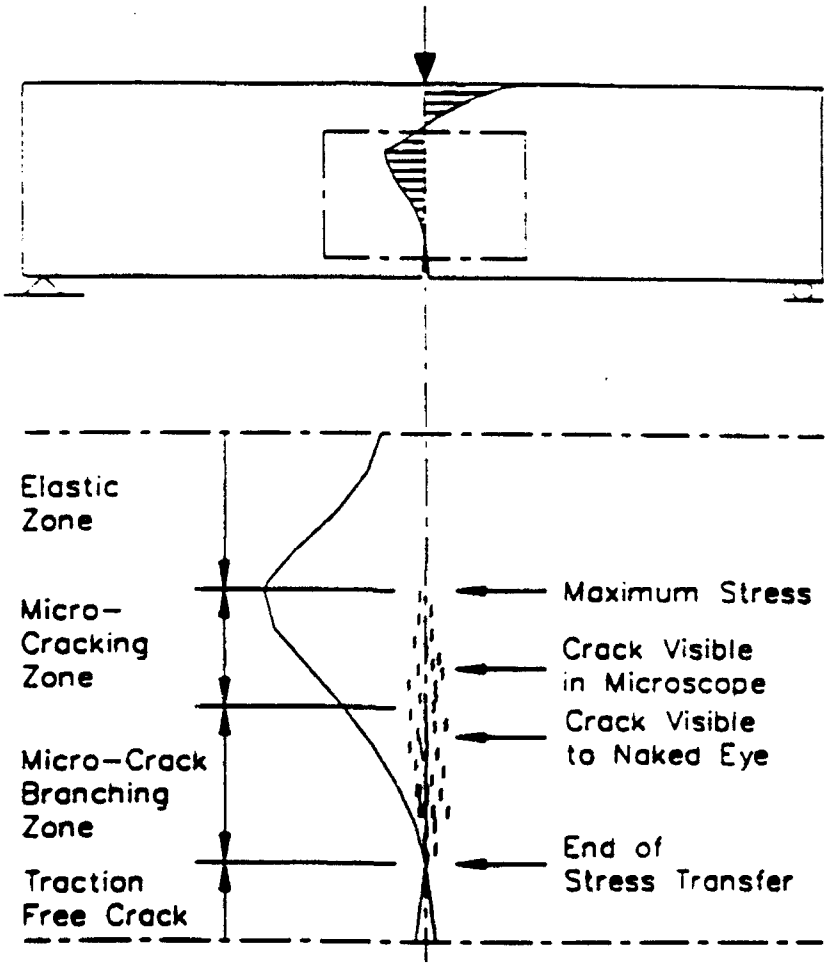

Figure 2. The Stress Distribution in the Fracture Zone of Concrete Beam [37].

2.2.2 Smeared Crack Band Model

Bazant and his co-workers [38-44] developed a smeared crack band model based on finite element model of a concrete fracture specimen. In this model, microcracks were modeled as a blunt smeared crack band. This band caused a zone of stress relief in the surrounding concrete as well as at the crack front. The stress and strain tensors remained uniform throughout the band width and an assumed stress-strain relationship was applied to smear the crack band elements. Bazant described the smeared crack band theory as a fracture theory for a heterogeneous aggregate material which displayed a gradual strain softening due to microcracking. In his model, the material fracture properties were characterized by three parameters: the fracture energy, the tensile strength, and the width of the smeared crack band. The strain softening modulus was a function of these parameters. They suggested that the optimum value of the crack band was three times the aggregate size.

This model was also applied to the analysis of reinforced concrete members by using an energy release rate criterion [39-45]. Later, the non-local smeared crack model [46, 47] was introduced to overcome spurious mesh sensitivity in finite element analysis. The same approach was used by Rots et al. [48, 49] and by Borst [50] who incorporated dissipative bulk behavior and triaxial effects.

Although the smeared crack band models have been successfully applied to describe the global responses of certain concrete specimens, they lack a theoretical foundation. There is no direct experimental evidence that a constant crack band width of uniform strain exists in concrete. Furthermore, the band width does not have any physical significance, since the numerical predictions are essentially insensitive to band width.

2.2.3 FPZ Model

As mentioned previously, the region where forces are transferred through the crack faces is called the fracture process zone (FPZ). The first FPZ model, which was modified from the Dugdale-Barenblatt model [51, 52], was proposed by Hillerborg and his co-workers [1]. Following Hillerborg, considerable variations of the Dugdale-Barenblatt model were suggested [53-61]. These models differed in fracture criteria, experimental procedures for determining the FPZ, and the assumptions regarding the constituency of the FPZ.

Hillerborg, Modeer, and Petersson [1] assumed that the stress did not fall to zero immediately as the crack opens, but decreased with increasing crack width. Tensile

strength of the concrete specimen was used as a fracture criterion. The concrete was assumed to be isotropic and linear elastic outside the FPZ. Inside the process zone, a constitutive relation governed the crack opening displacement, w, and crack closure stress, σ_{ccs}, as

$$\sigma_{ccs} = f(w) \tag{1}$$

The descending portion of the stress with increasing strain was called stress-softening curve and was assumed to be a material property. They also defined a characteristic length L_{ch} to characterize the brittleness of the materials as:

$$L_{ch} = \frac{G_C E}{f_t^2} \tag{2}$$

where G_C is the energy absorbing rate, E is the elastic modulus and f_t is the tensile strength of the concrete. They concluded that the maximum COD for FPZ was less than $0.2L_{ch}$.

The amount of energy absorbed per unit crack area in widening the crack from zero to w_1 is

$$G_C = \int_0^{w_1} \sigma_{ccs} dw \tag{3}$$

Standard test procedures for the experimental determinations of the fracture energy density of concrete were discussed by Hillerborg and Mindess [55-57]. The total external energy needed to quasi-statically fracture a specimen was simply the fracture energy density of concrete times the surface area of the crack that was formed.

Later, the same model was applied to design the concrete pipes and beams by Gustafsson and Hillerborg [58]. A similar model was proposed by Visalvanich and Naanman [59] for fiber reinforced concrete. Ingraffea and Gerstle [60] utilized the FPZ model to study mixed mode fracture problems. Wecharatana and Shah [3] fitted the computational results to the measured crack mouth opening displacement with FPZ model. In Reinhardt's model [61], the crack closure stress was described by a power function, which was independent of crack opening displacement.

Carpinteri and his co-workers [62, 63] numerically analyzed the effect of parameters involved in FPZ model. After inspecting the influences of elastic moduli, tensile strength, fracture energy, specimen depth and initial crack length, they suggested the use of a dimensionless number to describe the brittleness of the material. That number is

$$S_E = \frac{G_C}{f_t d} \tag{5}$$

where d is the specimen depth.

Wecharatana and Chiou [64] introduced a simple test specimen for observing the post-peak uniaxial tensile response of concrete. The test was conducted by using a closed-loop strain control and a simple self-interlocked grip. The complete load-displacement curve was monitored until the post-peak stress dropped to zero. The value of the maximum post-peak displacement, which was assumed to be the critical COD, was used for normalizing the post-peak stress-displacement relation. This normalized stress-displacement relationship was observed to be unique and might be considered a material property. The fracture energy was also calculated and seemed to be a specimen-dependent. They implied that this direct FPZ measurement method was not consistent.

Li and his co-workers [65-67] developed an indirect procedure to determine the crack closure stress versus crack opening displacement curve. The relation between crack closure stress and J integral derived by Rice [68] was utilized, although the applicability of J integral on concrete is still uncertain.

FPZ model was also used by Kobayashi, Hawkins and their co-workers [5,69-72]. The constitutive relation between CCS and COD was developed through a hybrid experimental-numerical analysis and an inverse procedure. The FPZ model was applied to crack line wedge loaded, double cantilever beam (CLWL-DCB) specimens and three point bend (3-PB) specimens. Both singular and non-singular FPZ models were proposed. The normal stress distribution around the FPZ for a singular model is shown in Figure 3. The area in front of the crack tip is the elastic deformation zone. The stresses right of the crack tip possesses a $\frac{1}{\sqrt{r}}$ singularity. The fracture surface behind the crack tip is divided into the microcracking zone, transition zone, aggregate bridging zone and traction free zone. The boundaries of the transition zone are not well defined. The maximum crack closure stress in the FPZ is less than the tensile strength of the concrete. That means there is a sudden drop of stress past the crack tip. Both static and dynamic mode I fracture were investigated using this FPZ model. Mixed mode I and mode II, quasi-static fracture was also studied by imposing a diagonal compressive loading on the CLWL-DCB specimen. They concluded that the energy dissipated in the trailing FPZ was a major sink in the fracture process of concrete.

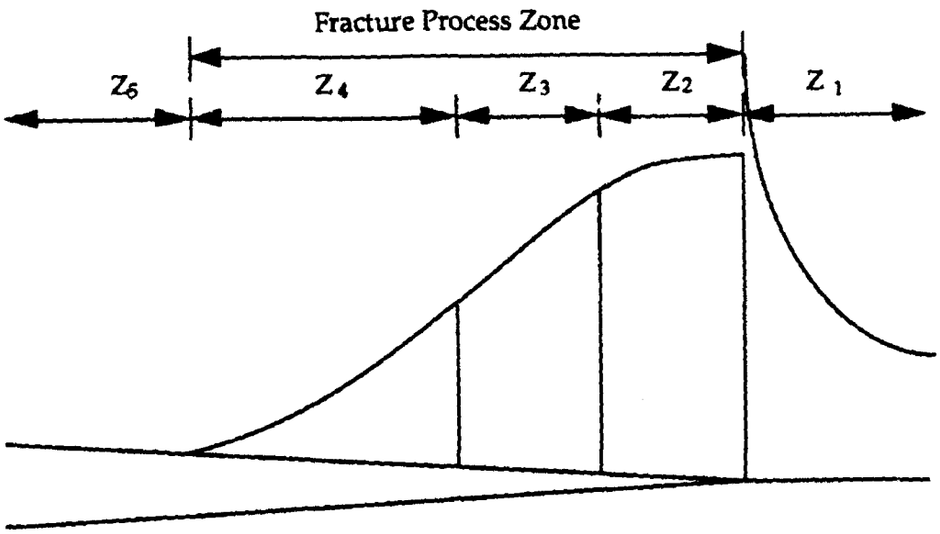

Z_1: Elastic Deformation Zone
Z_2: Microcracking Zone
Z_3: Transition Zone
Z_4: Aggregate Bridging Zone
Z_5: Traction Free Zone

Figure 3. Normal Stress Distribution Around Fracture Process Zone for the Singular Model.

2.3 Dynamic Fracture of Concrete

Dynamic fracture mechanics has been a subject of active research for the past two decades. Most of these studies have been confined to traditional metallic structures or polymeric materials. Although only limited researches were done on dynamic fracture of concrete [17-30], there is an increasing interest in studying the effects of strain or loading rate on the strength and fracture of concrete. Experimental evidences [73-76] indicates that the apparent strength of concrete increases with an increase in loading rate.

2.4 Mixed Mode Fracture of Concrete

Various models, such as maximum circumferential stress; maximum strain energy release rate; minimum strain energy density etc., have been proposed to predict the direction of crack propagation under mixed mode loading. Existing mixed mode fracture criteria are based on linear elastic, ideally homogeneous materials and a mixed mode fracture criterion for concrete-like heterogeneous material is not available.

Swartz et al. [77] measured the average total fracture energy under mixed mode fracture and showed that it was eight to ten times those obtained for mode I fracture. Jenq and Shah [78,79] compared the theoretically predicted failure angles of crack kinking under combined modes I and II loading using the maximum stress, the maximum energy release rate and the minimum strain energy density criteria with those measured experimentally in three-point and four point bend and shear, mixed-mode fracture tests and concluded that the differences were indistinguishable. Astro-Montero et al. [80] utilized the center-notched, diametrically loaded disc specimens to investigate the mixed mode FPZ in mortar. They defined the FPZ as the zone of deviation from linearity exceeding 60 microstrains and found the size of the FPZ in mixed mode was smaller that in mode I for short crack lengths. For longer crack lengths, after the crack adopted a straight line trajectory, the FPZ in the mixed mode specimen approached the dimension of the FPZ in mode I.

Maji et al. [81,82] studied crack propagation in rectangular blocks of mortar containing a central notch and subjected to uniaxial compression. Holographic interferometry was used to observe crack initiation and propagation, and to measure crack opening and sliding displacements (COD and CSD). Crack initiation theories were employed to study their relative merits for predicting crack initiation angles and loads. They found that while crack initiation was predicted well by some of the theories, it was necessary to account for the traction forces on the crack surface before any propagation criterion could be identified. They concluded that the Maximum Hoop Stress Criterion was reasonable and K_I stress intensity factor at the crack tip was dominant in the failure mechanism.

Carpinteri et al. [83] studied the single edge notched specimen subjected to four point shear. They showed that energy dissipation on the curvilinear fracture surface prevailed over energy dissipation in the bulk cementitious material, due to permanent deformation, friction and interlocking, when relatively small aggregates and large structural elements were considered. Mixed mode fracture energy was 16% higher than

mode I fracture energy with small aggregates and 33% higher with large aggregates. They attributed this increase in fracture energy to the additional energy dissipation by friction and interlocking, which was higher with larger aggregates, at the crack surfaces. They also observed that the interlocking effect increased with decreasing specimen size.

Mier et al. [84,85] studied mixed mode fracture tests of double-edge notched concrete specimens and found that the crack grew under mode I, even when the external loading was of mixed mode. Shear softening was also observed in their experiments.

Liaw et al. [16] used a crack line wedge loaded-double cantilever beam (CLWL-DCB) specimen subjected to diagonal compression loading to develop crack closure-shear transfer model of the FPZ of concrete. The model was used to predict the maximum load-carrying capacity and post fracture behavior of concrete specimens in which the cracks kinked under mixed-mode loading. The mode I FPZ was characterized by a trilinear crack closure stress (CCS) versus COD relationship, with the value of the maximum CCS at the physical crack tip equaled to the concrete tensile strength. To account for shear transfer in mixed-mode fracture, a linear regression analysis was performed on the published data. Their finite element computations showed that the effect of incorporating shear-transfer model on the global deformations and forces predicted for the CLWL-DCB was negligible. This may be due to the specimen geometry and loading condition, which generated straight crack trajectory. For a straight crack, slip on the rough crack surfaces is reduced since the crack opens through mode I displacements. For a curved crack, pure mode I opening cannot exist along the entire crack surface and the transfer of shear forces is inevitable. The simulation model was applied to Ingraffea and Gerstle's data [60], and showed that shear-transfer effects must be considered for certain loading and crack configurations.

In all of the above mentioned studies, the starter crack was a machined notch which was subjected to either pure mode II or mixed modes I and II loading. Aggregate interlocking in the FPZ, which trails a stably extending crack, would only be possible after growth of the FPZ crack tip, thus reducing the influence of FPZ on the crack which would otherwise propagate under the dominant influence of the mode I crack tip stress field. The FPZ and the associated energy dissipation in a concrete fracture under mixed modes I and II loading have been studied by Guo et al. [72]. The constitutive equations, which governs the fracture process zone, were represented in terms of the CCS versus COD and crack shearing stress (CSS) versus crack sliding displacement (CSD). They found that the dissipated energy rate at the FPZ increased with increased interlocking force despite the fact that the kinked crack propagated primarily as a mode I fracture. The

dynamic extension of the above mixed mode FPZ analysis in concrete fracture was studied in this AFOSR research grant.

2.5 Dynamic Fracture Test Methods

2.5.1 Charpy Impact Test

The Charpy impact test, in which a pendulum with a tup swings through a notched bar specimen, is recommended as standard impact testing of metal [86]. The total energy absorbed in fracturing a specimen is measured by the height of the pendulum before and after the impact. This method can not yield the very useful properties such as ultimate strength or fracture toughness. Furthermore, Abe et al. [87], while testing rate-insensitive silicon-carbide specimens with a detailed energy balance, have shown that energy absorbed by the specimen was only of the order of 30 percent of the total energy recorded in the Charpy test.

The instrumented impact test, which was introduced by Hibbert [88], is able to show the continuous load and energy histories. More recently, Shah and his co-workers [89-91] have conducted a series of tests on plain concrete and fiber reinforced concrete specimens with the modified instrumented impact test.

2.5.2 Split Hopkinson Bar Test

The pressure Hopkinson bar was originally designed to obtain compressive dynamic stress strain curves. The tension Hopkinson bars have been developed [92-95]. In the split Hopkinson bar test, the specimen is sandwiched between two coaxial elastic bars. The input stress wave pulse is normally generated by air gun or explosion. Upon impact of the two bars, compressive waves propagate away from the impact face in either direction. The compressive wave reflects in tension from the free ends. The force acting on the specimen is calculated by measuring the pulse at two points on either side of the specimen, and the strain in the specimen is measured by means of strain gages mounted on the specimen. This method is able to provide a large range of strain rate. Reinhardt et al. [96] and Jawed et al. [97] employed this method to study the strain rate effects in concrete. Jawed found that the ultimate stress increased with increasing strain rate first and then reached a plateau value at a strain rate of about 250 sec^{-1}.

2.5.3 Constant Strain Rate Test

The constant strain rate test is usually performed by a servo-controlled loading machine. Although it is limited by the conventional machine loading speed, this method has been used for some dynamic fracture tests at intermediate strain rates. K. Kobayashi and Cho [98] used displacement-controlled constant strain rate tests to obtain load-deflection curves for polyethylene fiber reinforced concrete beams. They observed that the loading velocity affected both the peak load carrying capacity and the corresponding deflection. Yon et al. [99] also used a displacement-controlled machine to conduct constant strain rate tests on three-point bend and CLWL-DCB concrete specimens. The strain rate sensitivity of concrete was fully discussed.

2.5.4 Drop-Weight Test

The drop-weight test has been recommended by the American Concrete Institute (ACI) committee 544 for evaluations of the impact resistance of fiber reinforced concrete [100]. The impact force and energy are determined by the drop weight and height. But similar to the problem of the Charpy impact test, this energy alone cannot provide enough information on fracture toughness. Therefore, the instrumented drop-weight test was introduced to measure the load, deflection, strain and energy histories during the impact event. With these data, the energy absorbed and dynamic fracture toughness can be derived.

2.6 Measurement Techniques

The popular optical methods for determining the dynamic stress intensity factors at room temperature, such as photoelasticity [101] and caustics [102], cannot be used for concrete due to the opaqueness and low Poisson's ratio, respectively. As for crack length measurements, the traditional photographic and crack gage techniques for monitoring crack propagation are inaccurate due to the small crack opening displacement in concrete. These physical constraints require a better fracture testing procedure which can circumvent some of the above difficulties in characterizing the fracture responses of brittle composites. The moire technique with its high sensitivity seems to fit in very well.

Moire interferometry is an attractive tool for whole-field displacement measurement. In addition to the wide application range, moire interferometry has following advantages [103]: high sensitivity; excellent fringe contrast; high spatial

resolution; extensive range; and real time response. Therefore, this method was utilized in the dynamic fracture tests in this research to determine the whole field displacement field.

The term moire comes from a France word referring to the visual interference effect of watered silk. In optics, moire refers to a phenomenon that occurs when two repetitious patterns are superimposed and deformed in relation to each other. A series of black and white bands termed "moire fringes" is then formed. Typically one grating (the specimen grating) is deformed while the other grating (the reference grating) is undeformed [104]. Moire is the interference between the specimen grating and reference grating or more generally between two set of lines. These lines can be generated by geometrical bar-and-space gratings or optical interference. The former is called geometrical moire [105], and the later is called moire interferometry [103]. The moire interferometric technique was used in this research for the experimental measurements.

Due to the previously mentioned advantages of moire interferometry, especial the whole-field information, real time response, and high sensitivity, this technique was used in mixed mode dynamic concrete test. Reference grating of 1200 lines/mm was used in this dynamic concrete tests, and the dynamic moire pattern was recorded.

2.6.1 Four Beam Moire Interferometry

In two beam moire interferometry, a virtual reference grating of two times of the specimen grating was obtained by interfering the $\pm$ first order diffractions from this specimen grating. The relation between the displacement, u, and the fringe order, N, is

$$u = \frac{N}{F} \tag{6}$$

where F is the virtual grating frequency.

Two beam moire is only good for a single direction displacement measurement. For mixed mode fracture analysis, both u and v directional displacements are necessary. A u-v mirror set, which was designed by M. Tuttle[1] and modified by F. X. Wang[2], was used to generate moire interferometry. As shown in Figure 4 (a) two beams from the horizontal mirrors interact to generate the u displacement moire pattern. Similarly in Figure 4 (b) another two beams at vertical positions are used to generate the v displacement moire pattern. These two patterns both diffract to the central mirror and then reflect to the

1. M. Tuttle: Professor in Mechanical Engineering Department, University of Washington.
2. F.X. Wang: Visiting Scientist in Mechanical Engineering Department, University of Washington, 1986-1991. Professor of Nan Chang Institute of Aeronautical Technology.

camera. u- and v-displacement moire patterns can be separated optically, but at the time these tests were conducted, the technique had not been developed yet. Therefore, u- and v- field patterns were recorded separately. The u-displacement and v-displacement fields were recorded at different delayed time and for different specimens. It was thus necessary to test many specimens in order to provide sufficient data for analysis.

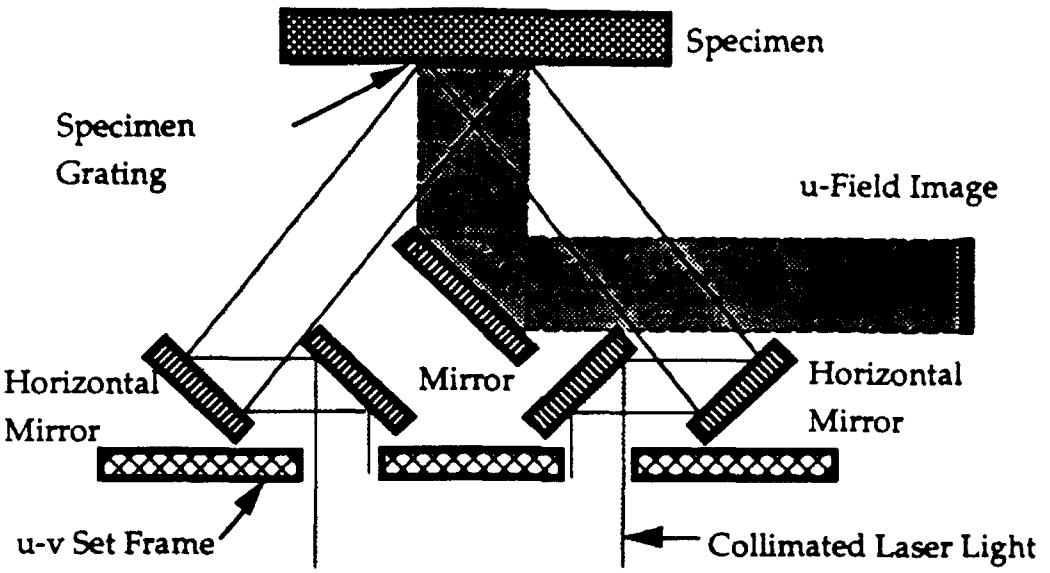

(a) Top View

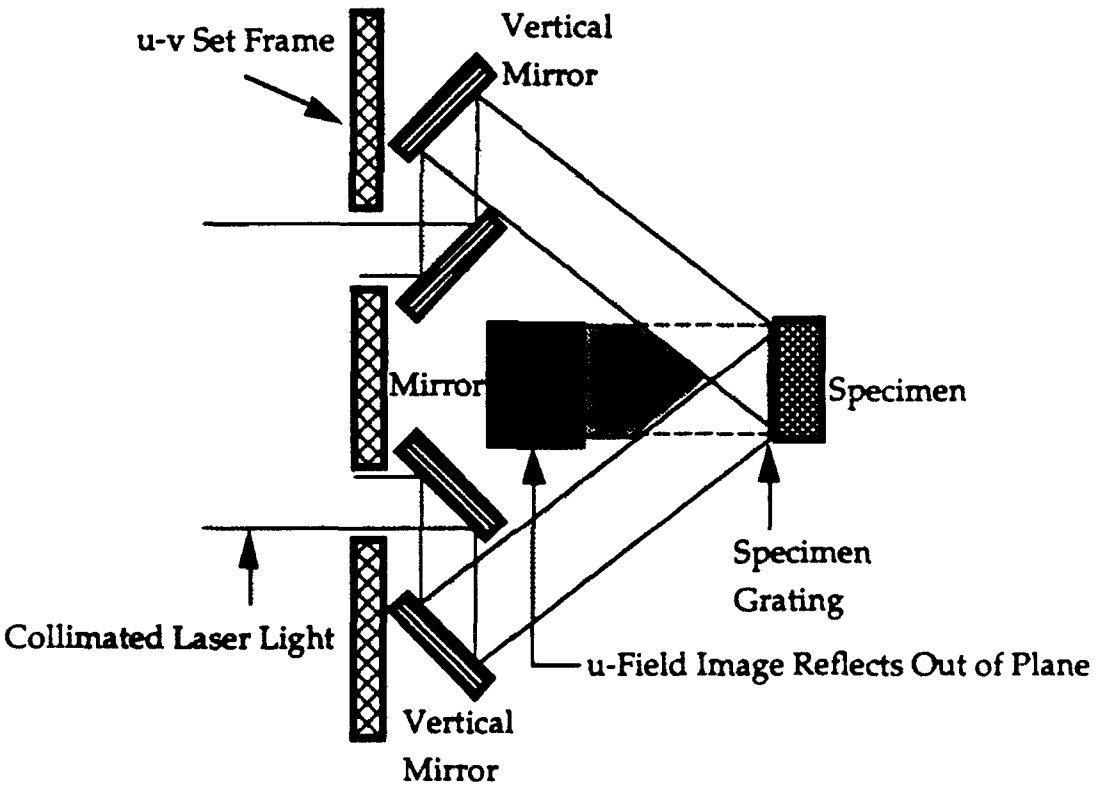

(b) Side View

Figure 4. u-v Mirror Set: Top View and Side View.

CHAPTER 3

EXPERIMENTAL AND NUMERICAL PROCEDURES

As mentioned previously, the main objectives of this concrete research are to analyze the mixed mode static and dynamic fracture of concrete and to identify the dominant energy dissipation mechanism. The procedure for mixed-mode, dynamic concrete fracture analysis are as follows:

1. Cast 3-point bend concrete specimens.
2. Cut a machine notch of 0.75 inch (19.1 mm).
3. Precrack the specimens to 1.25 inches (31.8 mm) length by using mode I static fracture.
4. Offset the load of the specimen for generating a mixed mode static/dynamic fracture test.
5. Run an inverse finite element analysis to determine the constitutive relations in FPZ.
6. Compute the energy release rate and energy dissipation rate in the FPZ.
7. Verify the crack kinking criterion in mixed mode fracture.

The details of each step of the above are described in subsequent sections.

3.1 Specimen Preparation

All the specimen used in this research were cast in the University of Washington, Department of Civil Engineering shop. The same cement, sand, water and aggregate gradation are used for all specimens for uniformity. Table 1 shows the average gradations for coarse and fine aggregates. The cement is a type III, high early strength Portland cement, and the sand and gravel were obtained locally. The same mix proportions shown in Table 3 were used for all specimens.

Table 1: Average Gradation of Aggregate

Sieve Size	No. 4	No. 8	No. 16	No. 30	No. 50	No. 100
% Left	1.50	15.79	28.87	43.88	78.54	97.50

Table 2: Concrete Mix Proportion by Weight

Cement	Sand	Gravel	Water
1.0	3.0	2.0	0.4-0.5

The specimens were cast in a horizontal position in an oil-lubricated, steel form. Each specimen was compacted with a mechanical form vibrator that moves across the top of the specimen. Control cylinders were also cast with each batch of fracture specimens, and each control cylinder was fabricated in three layers, where each layer was compacted with an one inch diameter electric immersion vibrator. The average compressive strength of concrete from the cylinder tests was 47.2 MPa. The estimated average tensile strength was 3.14 MPa.

Right after casting, the specimens and cylinders were covered with polyethylene sheets and stored at room temperature. The forms were stripped two days later, steel inserts were carefully removed from the specimens, and then both specimens and cylinders were immediately placed in a moist room. The surface of the specimen was manually polished with a carborundum stone at the early age of curing. This polishing step is necessary for transferring the moire grating and bonding the strain gages.

All the specimens were kept in the moist room for at least 28 days before testing. The specimen was removed from the moist room three days before testing. After it was dried for one night, the specimen was then notched by a slicing machine with a six inch diamond blade. The machine notch was 0.75 inch (19.1 mm) deep. After machining, the specimen was then cleaned and dried for another half day. Before the specimen grating was transferred, a layer of PC-10 cement was put on the specimen surface to fill out all the surface holes. One day later, the procedure described in [103] was used to transfer an orthogonal diffraction grating of 600 lines/mm to the specimen surface.

3.2 Static Precrack for Dynamic Analysis

The specimen was precracked to form a sharp precrack from the machine crack. An u-v mirror set shown in Figure 5 was utilized to generate the u and v field moire interferometry patterns. A manual screw driven loading fixture (Figure 6), designed by F. X. Wang, was used for mode I static precracking. Four beam moire interferometry as shown in Figure 4 was utilized during static precracking. The moire interferometry pattern on the specimen, which was recorded by a Nikon F-3 camera , was used to locate

the crack tip position. The static precrack length was 0.5 inch (12.7 mm) and the total initial crack length was thus increased to 1.25 inches (31.8 mm). The moire pattern prior to static precracking also provided the information for the determining of static modulus of elasticity.

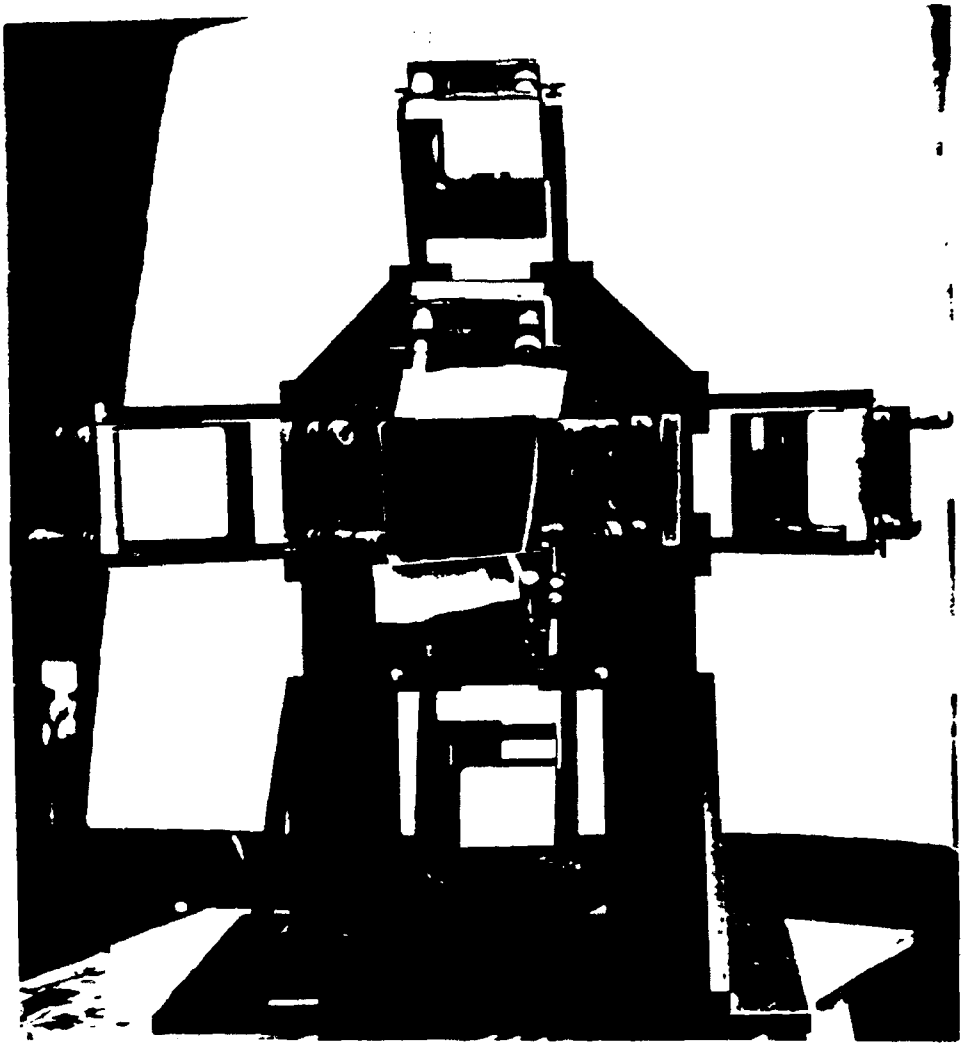

Figure 5. u-v Mirror Set

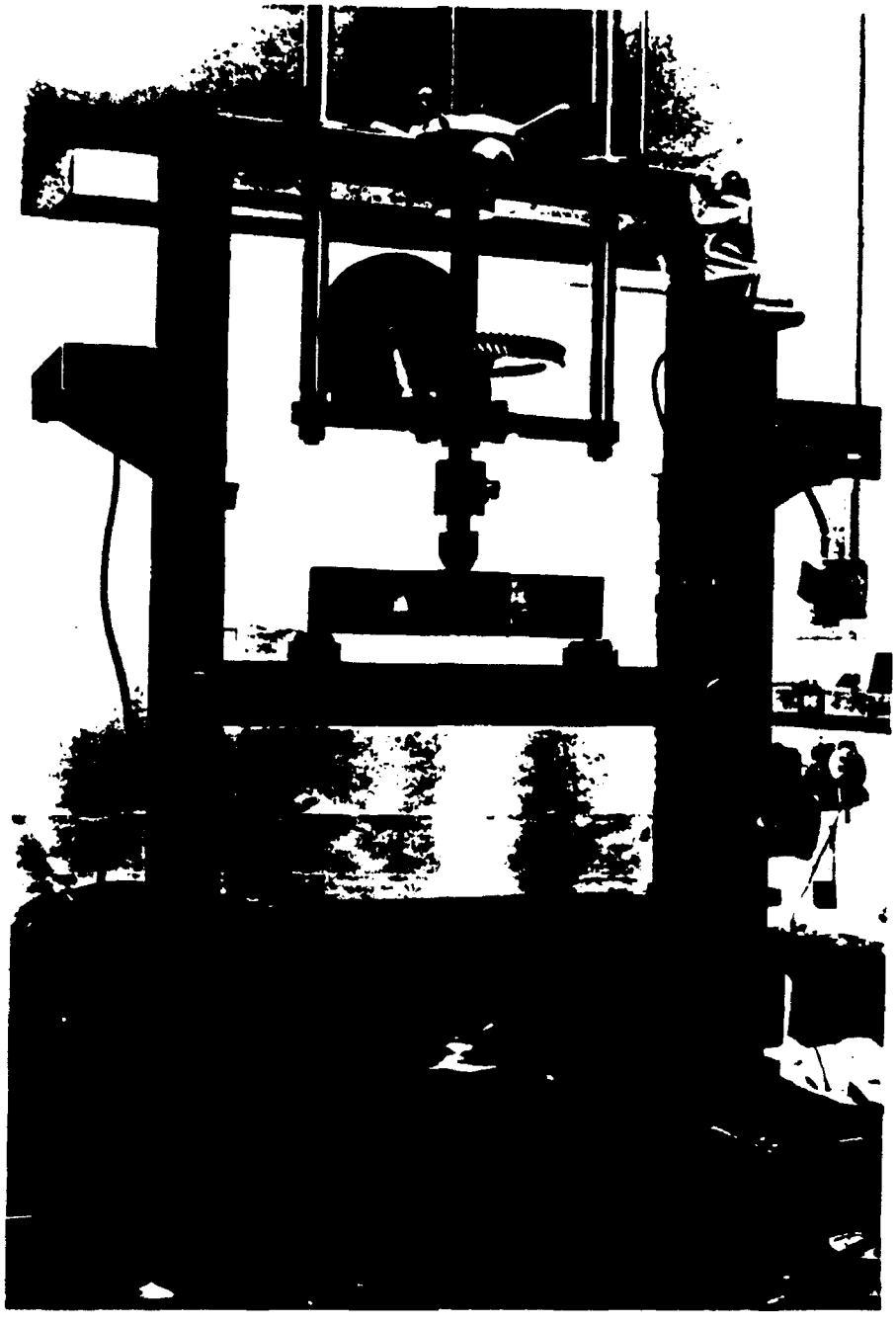

Figure 6. Loading Fixture for Precracking.

3.3 Test Procedure for Static Analysis

Mixed mode loading was then applied by rearranging the loading points in Figure 6 so that the notch was offset from the central loading point by 50.8 mm. The test procedure consisted of applying an incrementally increasing load-point displacement, photographing the moire fringes by two Nikon F-30 cameras and recording the applied load and displacements. The four beam moire interferometry setup, described previously, was used to record the horizontal, u, and the vertical, v, displacements in a 95 x 95 mm area surrounding the stably growing crack. The reflected first order diffraction from the oblique incident light of 18° provided a fringe multiplication of two and thus an effective sensitivity of 1200 lines/mm was achieved in this setup. The crack opening and crack sliding displacements (COD and CSD) along the slanted crack were computed from the moire patterns corresponding to the horizontal and vertical displacements. Load-point displacements were increased until the microcrack tip, which was located using the moire fringe pattern, had almost penetrated through the depth of the specimen.

3.4 Drop Weight Test for Dynamic Analysis

After the precrack, three strain gages were mounted along the predicted crack path to verify the crack velocity obtained from the moire interferometry patterns. The strain data prior to the passage of crack tip, provided the information for computing the dynamic modulus of elasticity.

The strain gages and associate instrumentation were selected for a frequency response of 70 KHz. The setup consisted of the following:

1. An IMACON 790 ultra speed camera and 1/5 T plug-in with a framing rate of 100,000 frames per second and an exposure time of 2 μsec. for dynamic analysis.
2. A high speed electric shutter (acousto-optic modulator) with an exposure time of 7 msec to shield the image tube of the camera from prolonged exposure to the argon laser light source.
3. A five watt argon ion laser from Spectral Physics.
4. A triggering circuit to initiate data acquisition.
5. A dynamic non-contact displacement gage.
6. A dynamic load cell with power supply.
7. A dynamic strain gage conditioner for three strain gages.
8. Three oscilloscopes to record the loading history, the load point displacement and dynamic strains.

9. A Macintosh IIci personal computer for data processing and storage.
10. A drop weight loading fixture as shown in Figure 7.

The impactor weighs 98.8N and the height of drop was 0.4 m. A specimen grating of 600 lines/mm and a reference grating of 1,200 lines/mm were utilized for moire interferometry. The incident angle of the two collimated laser beams are about 18 degree.

The entire dynamic system setup is shown in Figure 8. The same u-v mirror set used in precracking was utilized to produce a moire pattern. When the impactor hit the top of the load block, it closed a circuit and sent a signal to the trigger box, which delivered three triggering signals. The first triggering signal was sent to a delay generator. After a specified delay time, another signal was generated by the delay generator and triggered the IMACON 790 camera. The second signal was sent to the oscilloscopes to record the load history, load point displacement, and three dynamic strain data. The last signal was sent to acousto-optic modulator (AOM) driver. The AOM worked like a shutter of the laser for protecting the image tube of the high speed camera from long exposure to a laser light.

For each three-point bend test, the following experimental results were obtained:

1. Horizontal displacement or vertical displacement from the moire patterns.
2. Crack velocity from the sequence of moire patterns.
3. Load history.
4. Load-line displacement history.
5. Three strain histories at three strain gage locations.

The data measured by the oscilloscopes were later transferred to a Macintosh IIci personal computer for data manipulation and storage. A program developed by L. G. Deobald and modified by Z. K. Guo and the author was utilized to transfer the data. The program is written in Quick Basic. The commercial program Excel[3] and DeltaGraph[4] were used for data manipulation and plotting, respectively.

---

[3] Microsoft excel for Apple Macintosh, Microsoft Corporation, One Microsoft Way, Redmond, WA 98052-6399

[4] DeltaGraph, DeltaPoint, Inc., 200 Heritage Harbor, suite G Monterey, CA 93940

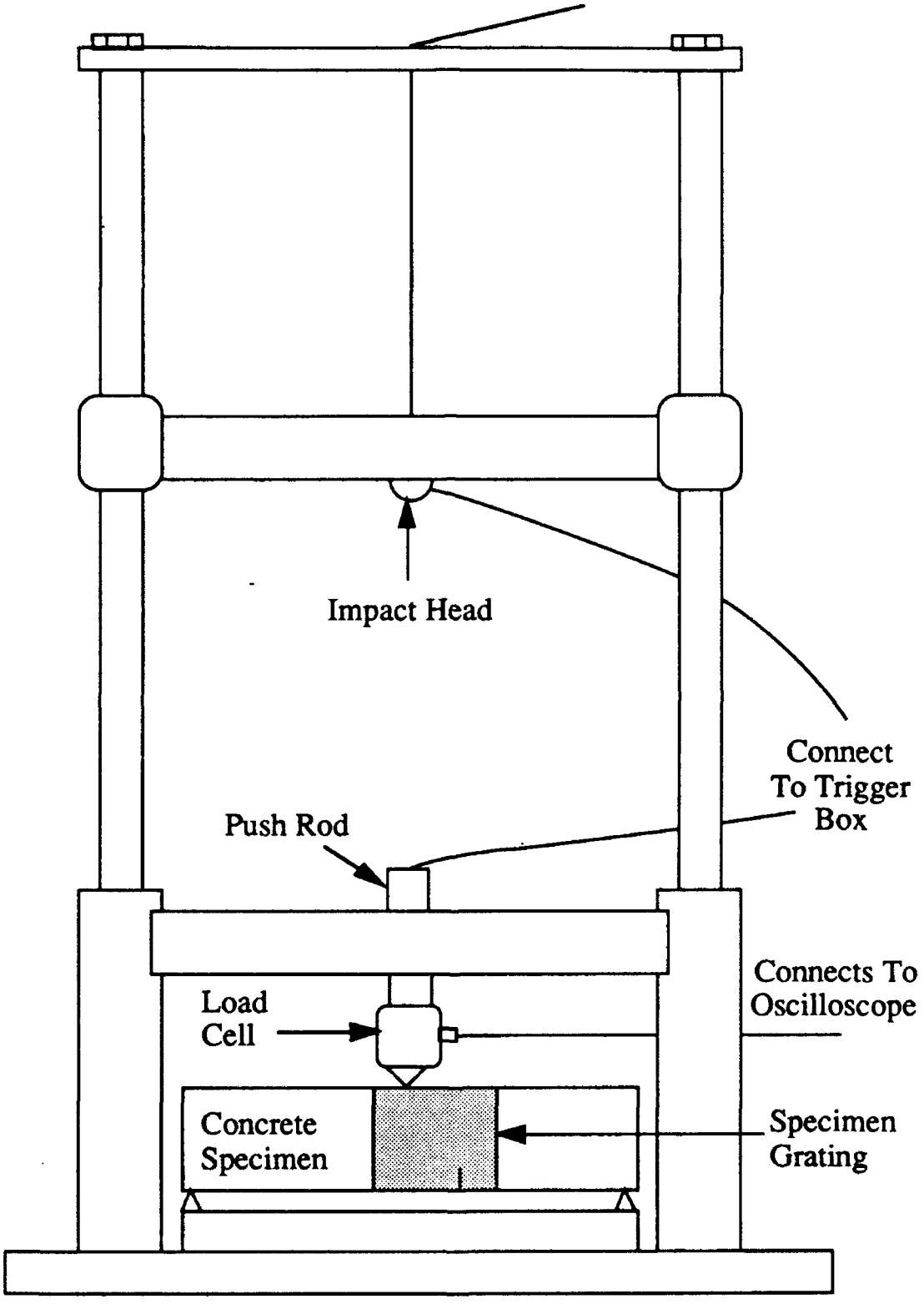

Figure 7. Drop Weight Loading Fixture.

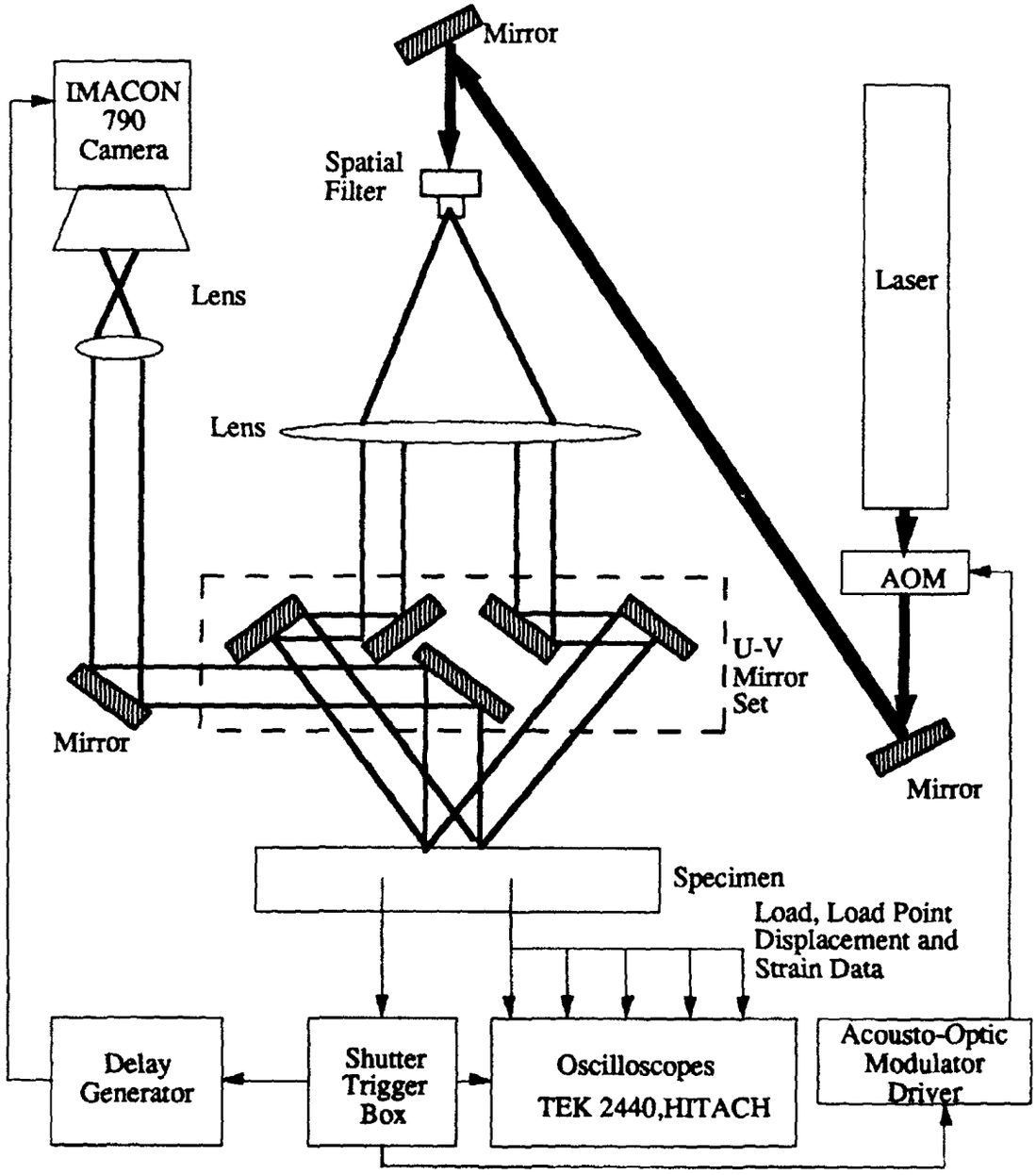

Figure 8. System Setup for Dynamic Concrete Tests.

3.5 Dynamic Moire Interferometry

As mentioned before, one of the merits of moire interferometry is its real time response which is suitable for dynamic fracture tests. The technical challenge is to record the dynamic moire pattern in a very short time. An IMACON 790 ultra high speed camera was utilized in this experiment for recording. With the 1/5 T plug-in, the camera had the ability to take pictures at the speed of 100,000 frames per second for an exposure time of 2 μsec per frame. Using a five watt argon ion laser and appropriate triggering circuit, the dynamic moire interferometry patterns were recorded.

Since the exposure time is short, a high power argon ion laser was necessary to provide the necessary light intensity. The appropriate triggering system was also very important for recording the crack propagation process at the right moment.

The number and size of the images are restricted by the camera where larger number of frames result in smaller picture size. IMACON 790 can record four to twenty frames per positive photo sheet. For good resolution and a sufficiently long period of recording, eight frames were taken per specimen during a period of 70 μsec. Different period of recording time can be chosen by using a delay generator. By combining all the data from different specimens for different delayed time, a composite picture of the fracture process in a concrete specimen was obtained.

CHAPTER 4
FINITE ELEMENT ANALYSIS

4.1 Hybrid Experimental-Numerical Analysis

A hybrid experimental-numerical analysis [106] was used to determine the constitutive relations of CCS versus COD and CSS versus CSD. The load history and crack velocity from the experiment were used as input to a two-dimensional finite element model of a concrete 3-point bend specimen. The boundary conditions plus the assumed constitutive relations were also part of the model. An inverse analysis was used to compare the computed, which was based on assumed constitutive equations governing the FPZ, with experimental COD's and CSD's. A flow chart for this inverse analysis is shown in Figure 9.

4.2 Finite Element Modeling

A 2-D finite element model was used to simulate mixed mode dynamic fracture of concrete. Figures 10 and 11 shows the model mesh and boundary conditions. Finer triangular elements are used along the average crack path.

4.3 Static Analysis

The entire specimen had to be modeled for this mixed mode fracture analysis, as in the analysis by Liaw et al [16], due to the lack of symmetry in the loading geometry. Since the boundary conditions were completely prescribed from the experimental data, the solution to this finite element boundary value problem should have provided the desired answers directly as in the analysis by Guo et al. [72]. In practice, the relative displacement field obtained from the finite-sized moire grating did not provide the absolute displacements which had to be prescribed along the FEM model of the kinked crack. Thus the time consuming inverse analysis was used in this study.

The numerical procedure then was used to determine the crack closing stress (CCS) due to aggregate bridging and the crack shearing stress (CSS) due to aggregate interlocking under a prescribed load. Through a trial and error process, the computed COD's and CSD's during the kinked crack extension were matched with their measured counterparts. The resultant CCS versus COD and the CSS versus CSD relations are the constitutive relations which govern the FPZ trailing the tip of the stably growing crack. The sum of the work done by the CCS acting on the COD and the CSS acting on the CSD for unit crack extension represents the energy dissipation rate in the FPZ.

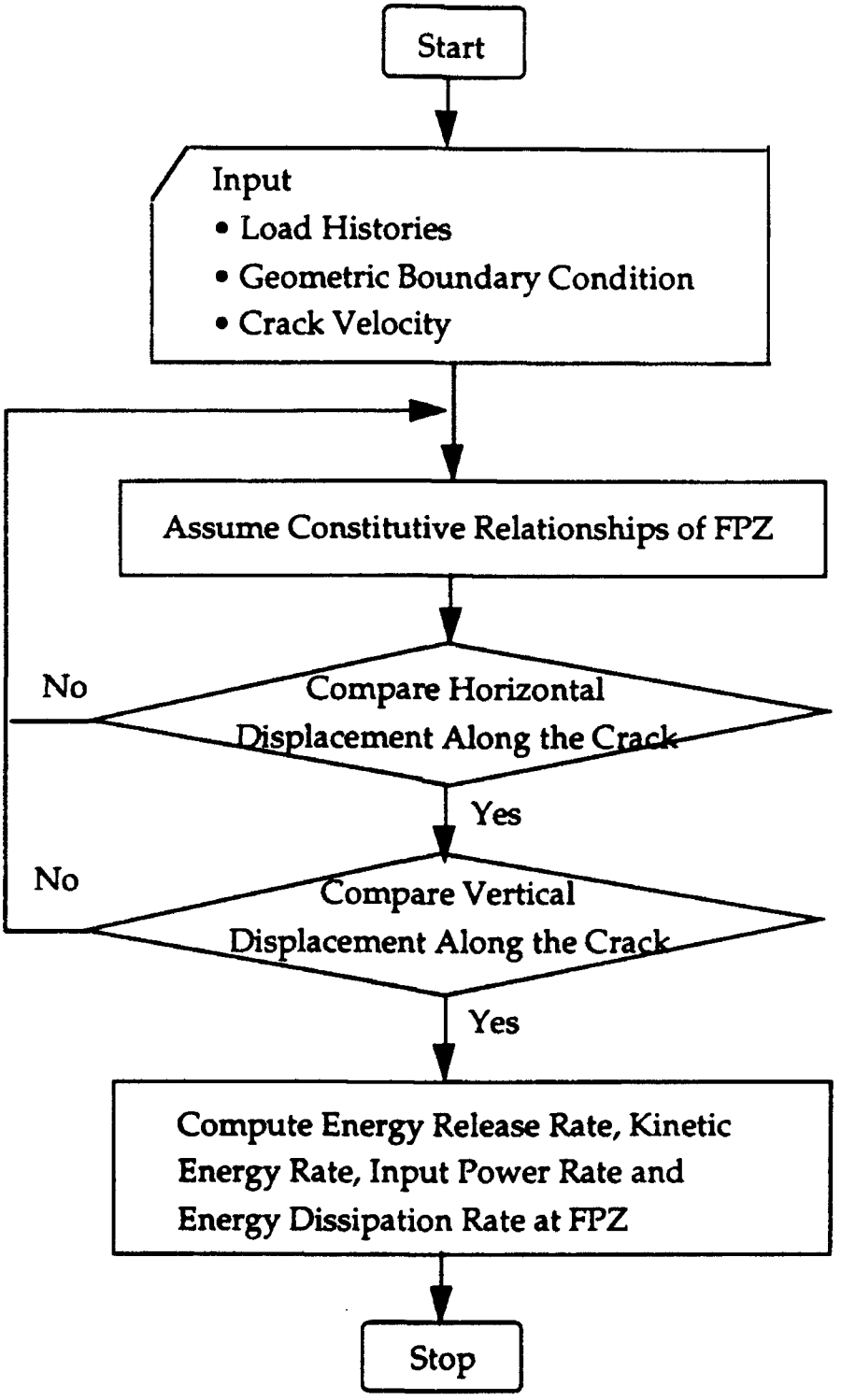

Figure 9. Analysis Flow Chart.

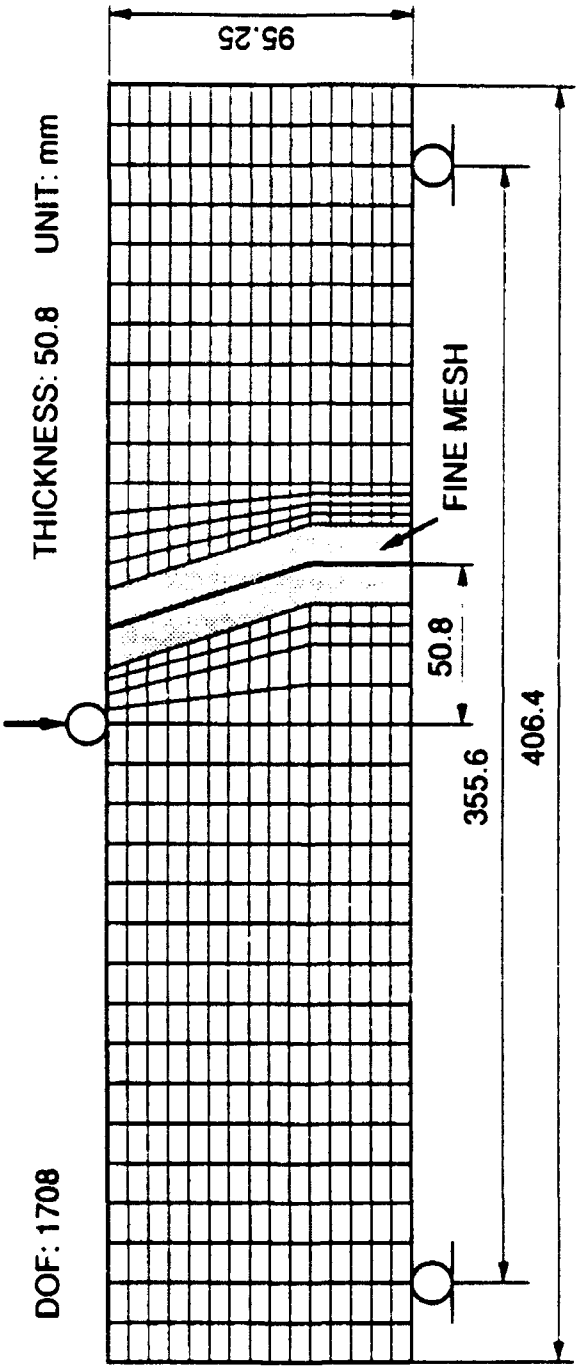

Figure 10. 2-D Finite Element Model of Concrete Specimen.

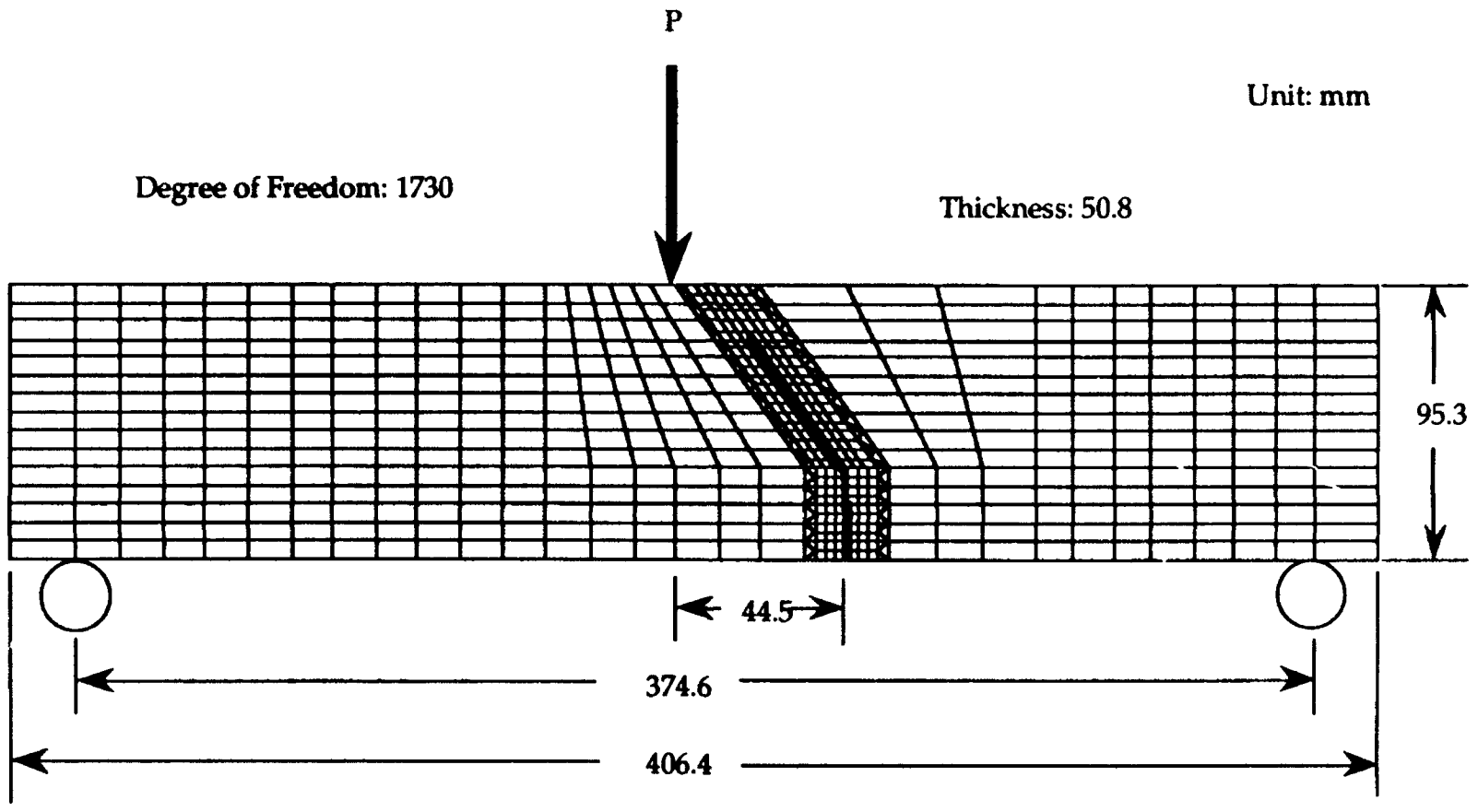

Figure 11. 2-D Finite Element Model of Concrete Specimen Used for Dynamic Analysis.

The energy release rate was computed directly by incrementing the crack tip one finite element node and then computing the difference in elastic energies stored in the specimen prior to, and after, that incremental crack extension.

The modes I and II stress intensity factors, K_I and K_{II}, were computed from the strain energy release rate and the crack tip COD and CSD. First, the finite element model was numerically calibrated for accurate stress intensity factor determination by using known K_I and K_{II} solutions. Then the strain energy release rate, G, was obtained from finite element analysis. This G is related to K_I and K_{II} by

$$\frac{K_I^2(1-v^2)}{E} + \frac{K_{II}^2(1-v^2)}{E} = G \tag{7}$$

where E and v are the modulus of elasticity and Poisson ratio, respectively.

K_I and K_{II} are also related to the crack tip COD and CSD through

$$\frac{K_I}{K_{II}} = \frac{COD}{CSD} \tag{8}$$

These two equations were used to compute the resistance curves for K_I and K_{II} or the cnanges in K_I and K_{II} with stable crack growth.

4.4 Dynamic Analysis

There are total 783 node points, 645 four point elements, 90 three point elements, and 52 spring elements in the FEM model used in dynamic analysis. Inputs to the finite element model include loading history, measured crack velocity, and assumed constitutive relations in FPZ. Nonlinear spring elements are used to model the FPZ as in the FEM model for ceramics. The difference is that the mixed mode I and mode II fracture requires the use of two sets of springs for each pair of fracture nodes in the concrete model. One set of spring models the crack closure stress, and the other set models the crack shearing stress. Both sets of springs had negative stiffnesses of decreasing reaction force with increasing displacement.

The quasi-static and rapid crack extensions were controlled by using a user defined subroutine to release the multi-points-constrains at specified time. Another subroutine was implemented to provide a function for gradual release of nodal force. Otherwise, sudden release of two nodal constrains will generate an impulse of stress waves. The time dependent nodal force release mechanism involves linearly decreasing the nodal

force from the tensile strength to zero as crack propagates to next node point. This mechanism smoothed the crack propagation process and removed the unrealistic fluctuating stress waves.

The outputs of finite element program included histories of COD's, CSD's, and various energy contributions.

4.5 Fracture Process Zone Characterization

The FPZ in mixed mode dynamic fracture consists of two constitutive relations. One is the CCS versus COD, and the other is the CSS versus CSD. Both closure stress and shear stress are the products of crack bridging and aggregate interlocking. In the 2-D finite element modeling, the FPZ is simulated by two sets of nonlinear springs. Due to crack kinking, a local coordinate system is necessary for applying the crack closure stress and shear stress at the right directions. The energy dissipated in the FPZ then can be calculated numerically by using the two constitutive relations and the crack opening shape.

4.6 Fracture Resistance Curve

One of the advantages of the hybrid experimental-numerical analysis is that a wealth of information is obtained through a single analysis. This analysis provides the history of the changes in energy partition with crack extension. The change in the driving force is obtained through the total energy release rate.

Energy balance per unit thickness in dynamic fracture can be written in terms of kinetic energy as

$$G = \frac{dF}{da} - \frac{dU}{da} - \frac{dT}{da} \tag{9}$$

$$R = \frac{dW}{da} \tag{10}$$

$$G = R \tag{11}$$

where G and R denote the crack driving force and the crack resistance, respectively; F is the external work done on the specimen; U is the elastic energy; T is the kinetic energy in the component; and W denotes the energy required for crack extension. All F, U and T can be calculated by the finite element method. Therefore, the fracture resistance, R, can be determined numerically.

Note that the value of G for rapid crack propagation does not correspond to a unique value of K as in the static case, where R depends upon crack speed $R = R(V)$. According to Broberg [107], if the surface energy is negligibly small, the crack will nucleate from an infinitesimally small microcrack and will achieve the limiting velocity immediately. However, a crack velocity curve including a rising portion, a peak value, and a dropping portion was observed and used in this research.

Freund [108], using the energy flow rate formulation developed by Atkinson and Eshelby [109], related the energy release rate with the dynamic stress intensity factor for dynamic crack propagation. This relation can be written as

$$G_D = \frac{1+\nu}{E} K_D^2 A(V) \tag{12}$$

where A is a geometry-independent function of crack velocity, V. While Freund's solution is based on a linear elastic condition with an unloaded crack propagating at a constant velocity, no solution is available for a crack with a varying velocity and an accompanying FPZ. Therefore, the crack resistance curve in this mixed mode dynamic concrete fracture is reported in terms of energy release rates and not in terms of the dynamic stress intensity factor.

CHAPTER 5
EXPERIMENTAL RESULTS

5.1 Static Results

A total of five concrete specimens were tested for stable crack growth under mixed mode fracture. The kinked crack paths for the first batch of two concrete specimens differed from those for the second batch of three specimens as shown in Figure 12. This difference was attributed to the longer crack extensions generated during the mode I loading of the second batch of specimens. The undulations in the crack paths, which is not normally observed in metal fracture specimens, are caused by the aggregates dispersed throughout the thickness of the specimen. For the same reason differences of about one aggregate diameter were observed between the crack paths for the front and the back specimen surfaces. For FEM modeling, the averaged crack paths, as indicated by the broken lines in Figure 12, were used in the numerical analysis. The concrete strength at the time of the test, as determined from tests on 150 x 300 mm cylinders, was 48 MPa.

Figure 13 shows the averaged measured load versus computed load-line displacement relations for the two batches of specimens. It was necessary to use the computed rather than the measured load-line displacements since the latter, which was recorded on one side of the specimen only, did not represent the actual deflections because there was uneven local crushing at the load point that twisted the displacement device.

Figure 14 shows a typical pair of moire interferometry patterns corresponding to the horizontal and vertical displacement fields of u_x and u_y, respectively of a kinked crack in a three point bend specimen. Figure 15 is a composite figure showing the averaged COD and averaged CSD variations along the initial and kinked crack with increasing crack extensions for the second batch of test specimens. The COD's and CSD's are plotted in term of the averaged distance measured along the vertical and kinked crack paths. Similar relations were obtained for the first batch of two specimens with an averaged kinking angle of 30°. The curves in this figure are the averaged displacements obtained from moire interferometry results and the circles are computed results obtained from FEM modeling. The CSD's along the kinked portion of the crack are negligible, but are appreciable along the vertical portion of the crack. The constant CSD's for a given crack length in this region indicates a vanishing ε_{yy} in this free corner of the specimen.

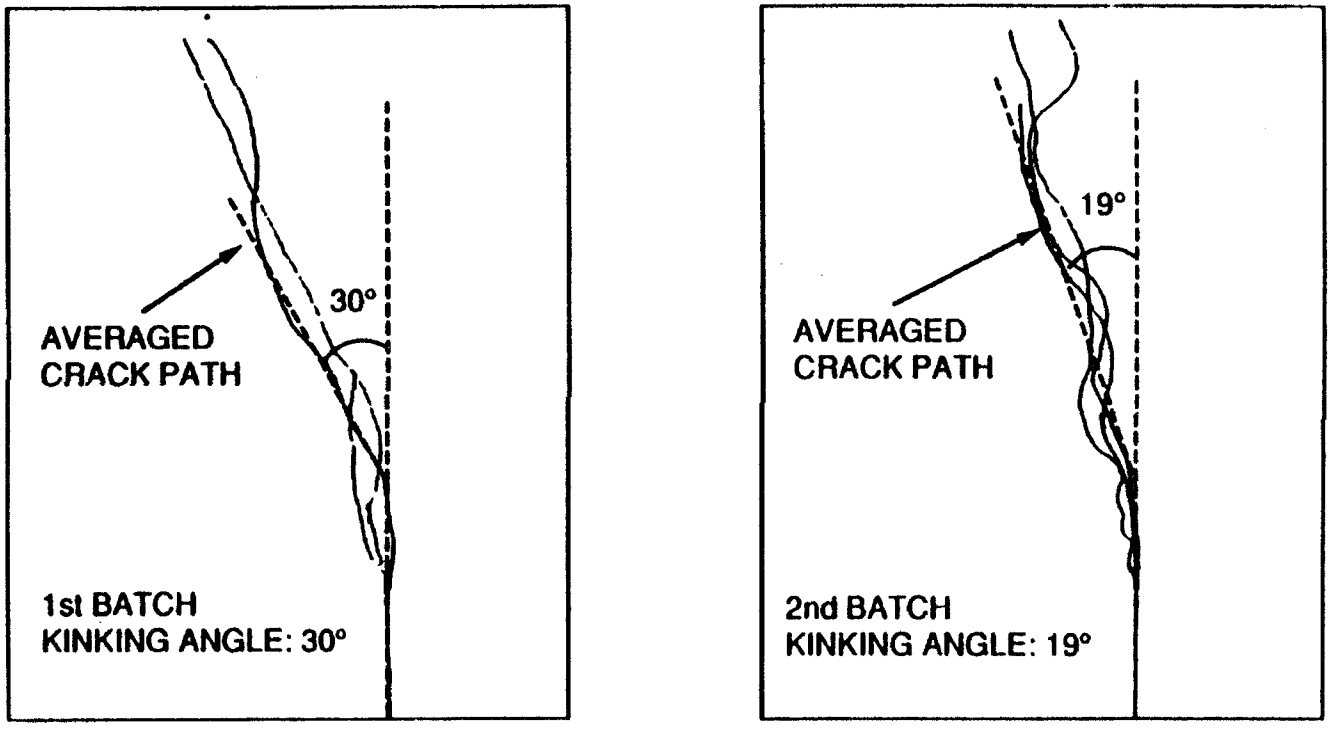

Figure 12. Kinked Crack Paths in Five Concrete Fracture Specimens.

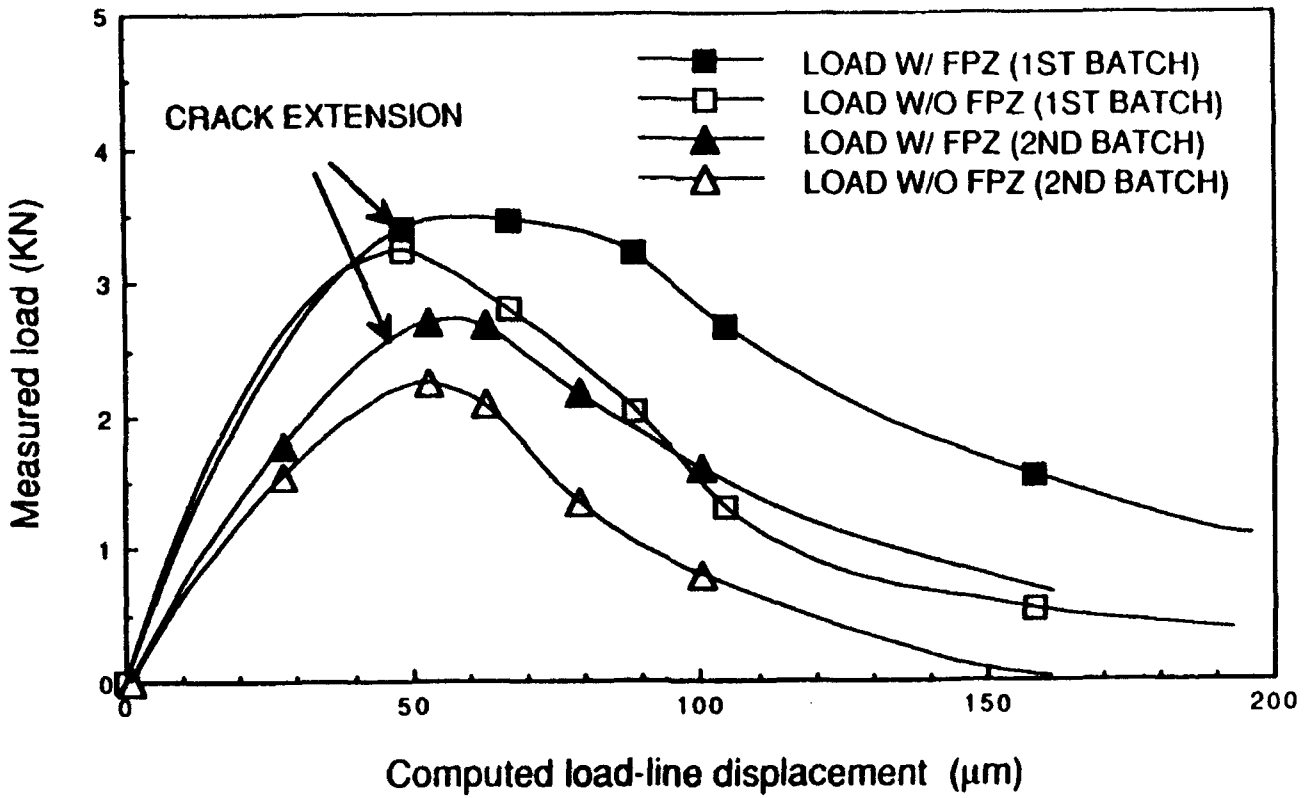

Figure 13. Averaged Load and Displacement Variations with Kinked Crack Extension.

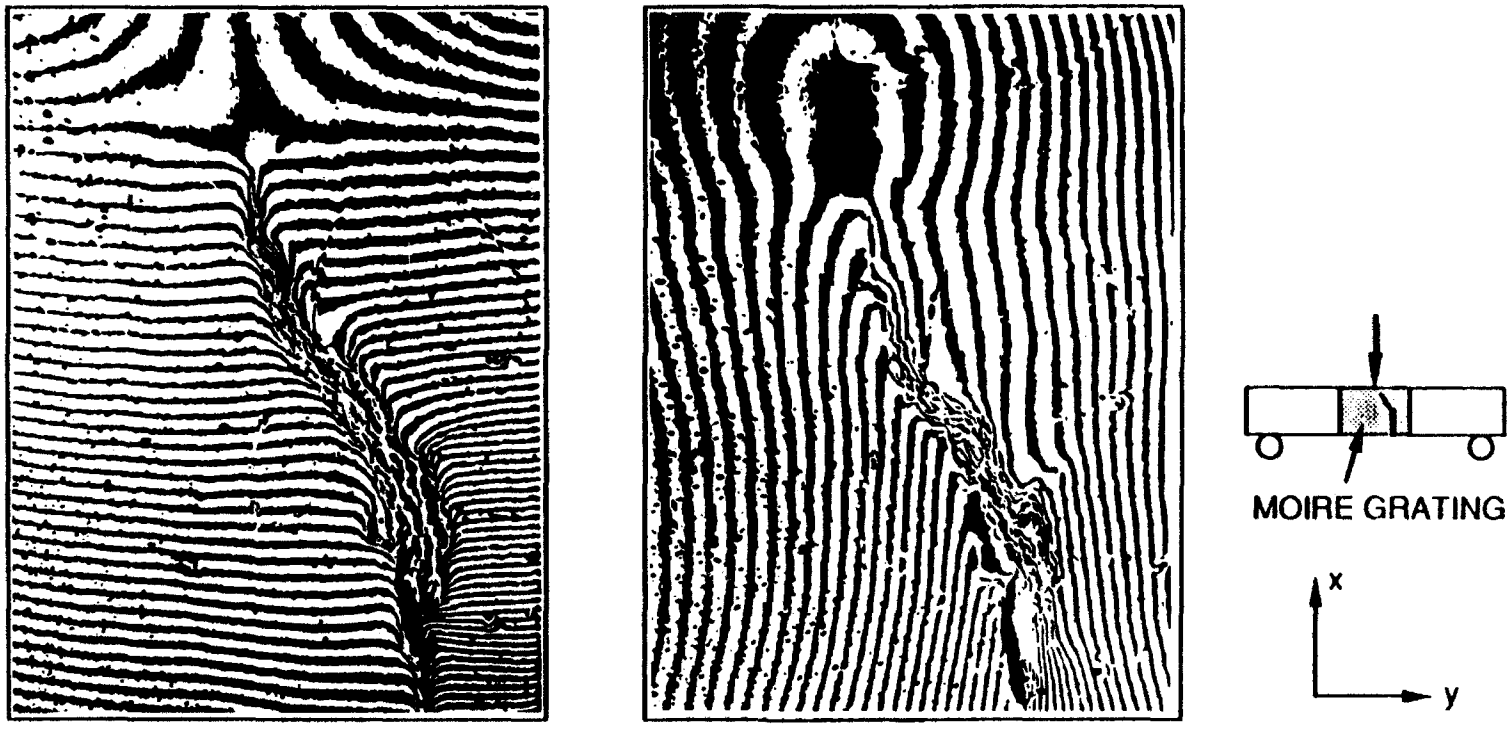

Figure 14. Typical u_x- and u_y-Moire Patterns.

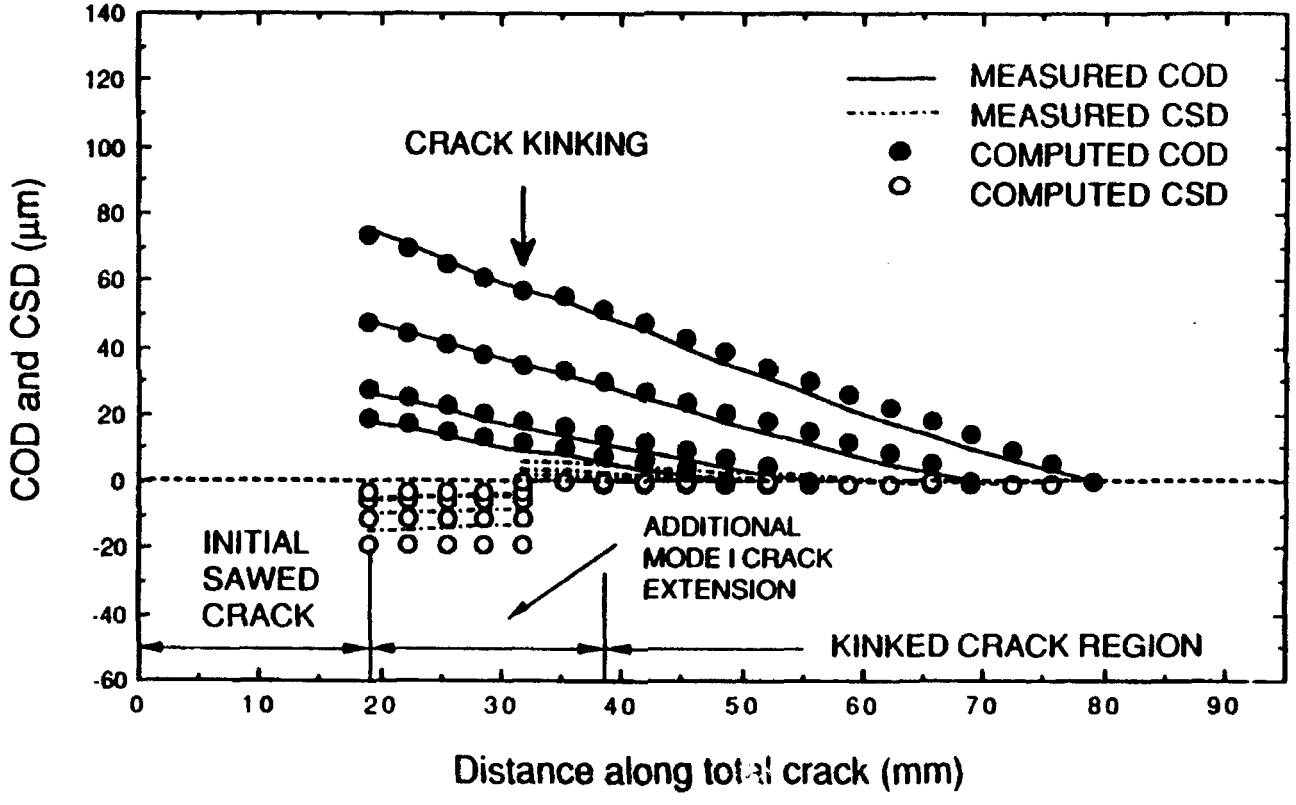

Figure 15. Measured and Computed Crack Opening (COD) and Sliding (CSD) Displacements in 2nd Batch of Specimens.

5.2 Dynamic Results

Although a considerable number of specimens were tested, only a handful of tests provided the complete test information necessary for data reduction. Thus the horizontal displacements in six 3-point bend concrete specimens and the vertical displacement data of three 3-point bend specimens were recorded.

Only a short period of the total fracture process in concrete could be recorded in each test due to the restricted number of high speed photography frames available per dynamic test. In addition, the tolerable minimum frame size limited the recording event to eight frames per test when the IMACON 790 ultra speed camera was used. The eight frames of moire patterns translated into a recording period of 70 μsec for each test. Thus a total of 20 specimens were tested at different delay times in order to record the whole fracture process. Six out of sixteen specimens were used to calculate the horizontal displacement, and three out of four specimens were used to compute the vertical displacement. The unused test results in each batch had to be discarded due to poor quality of the high speed photography or failure in the strain and load line displacement recording. Figure 16 and Figure 17 show a typical sequence of moire patterns corresponding to horizontal and vertical displacements in mixed mode fracture. The dark area in the picture is a target to locate the crack tip and calibrate the length. The experimentally determined vertical and horizontal displacements along the crack are shown in Figures 18 and 19. The distance along the crack, *l*, is defined as the distance from the crack mouth. At the crack tip, *l* is equal to the crack length, a. Figure 19 is the superposition of six specimens where the horizontal displacements along the crack were determined and Figure 19 is the superposition of the other three specimens where the vertical displacements along the crack were determined. All specimens were loaded under the same condition but recorded at a different delay time. The combination of Figures 18 and 19 provides a complete picture of the displacements along the crack during dynamic crack propagation.

The loading history was recorded by a dynamic load cell. Figure 20 shows the loading history of each specimen and the average loading history curve. The average load was used as part of the finite element input.

Another input condition is the crack velocity. Figure 21 shows the crack velocities obtained from moire interferometry. The scattering of the data is moderate considering that Figure 21 is a compilation of data from seven specimens. There are two reasons for the data scatter. Microscopically, concrete is not a homogeneous material. Aggregates in

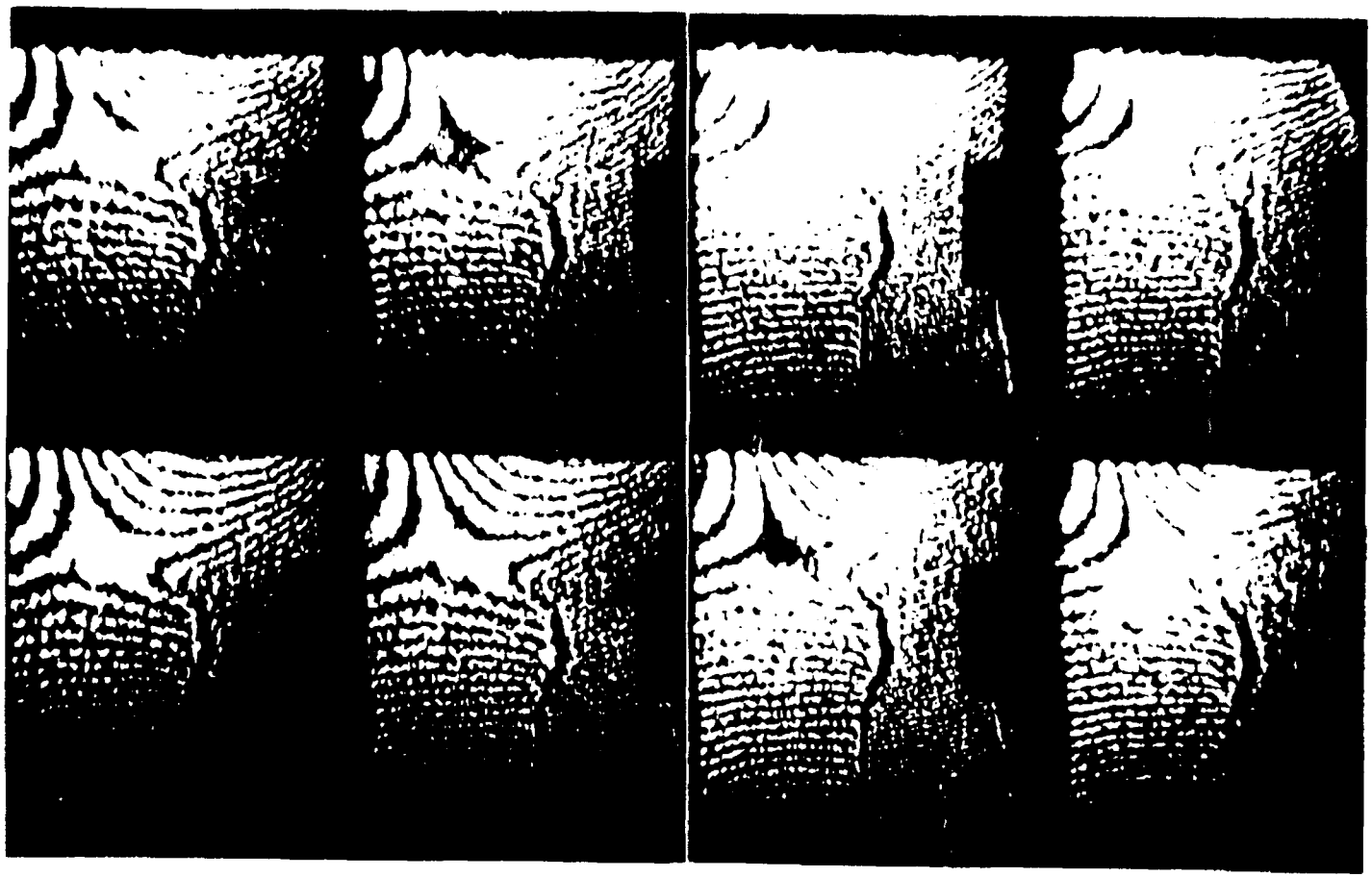

Figure 16. Sequence of Moire patterns from IMACON 790 Camera (Horizontal Displacement). Specimen MB2-4.

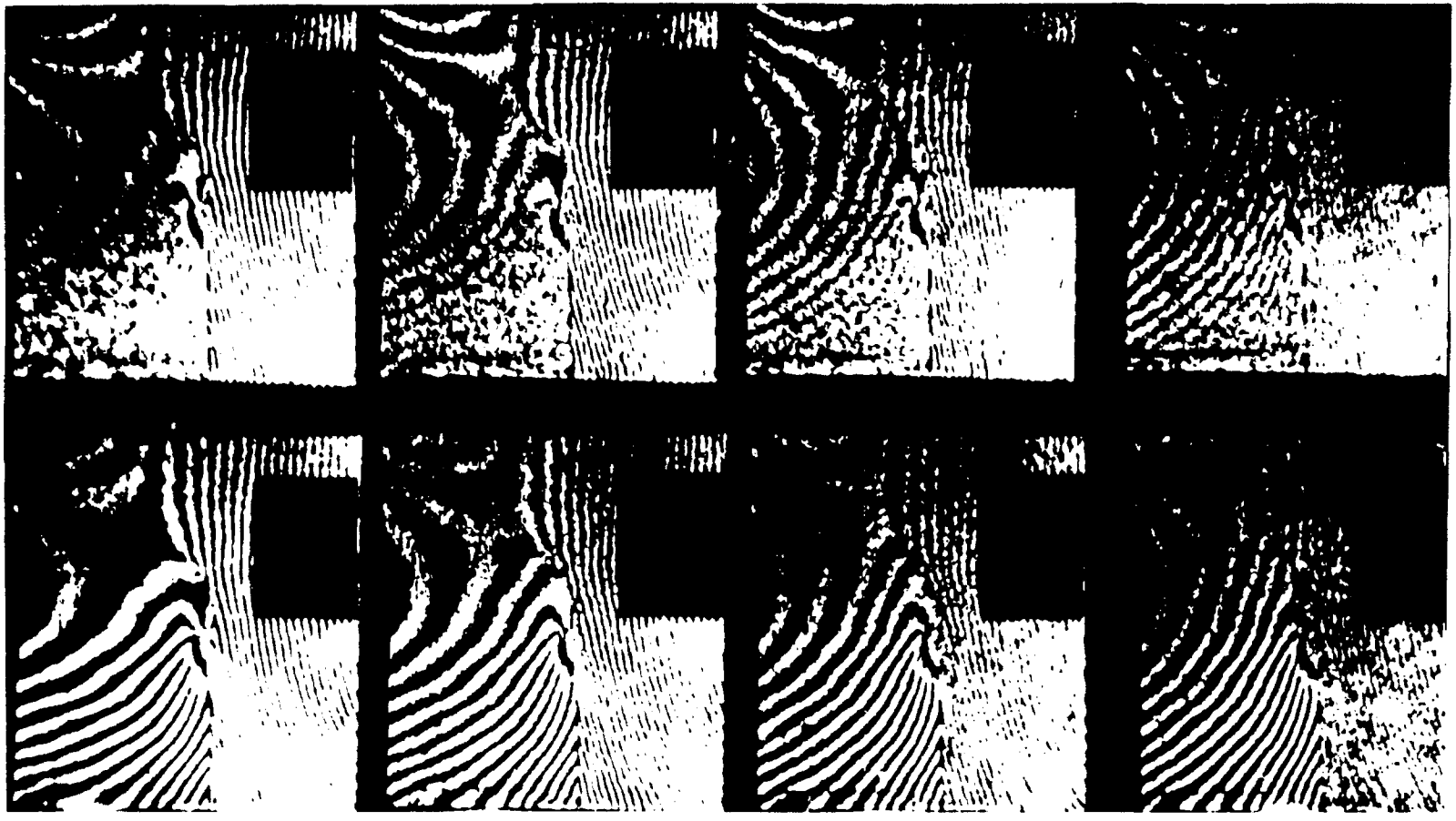

Figure 17. Sequence of moire patterns from IMACON 790 Camera (Vertical Displacement). Specimen MB2-20.

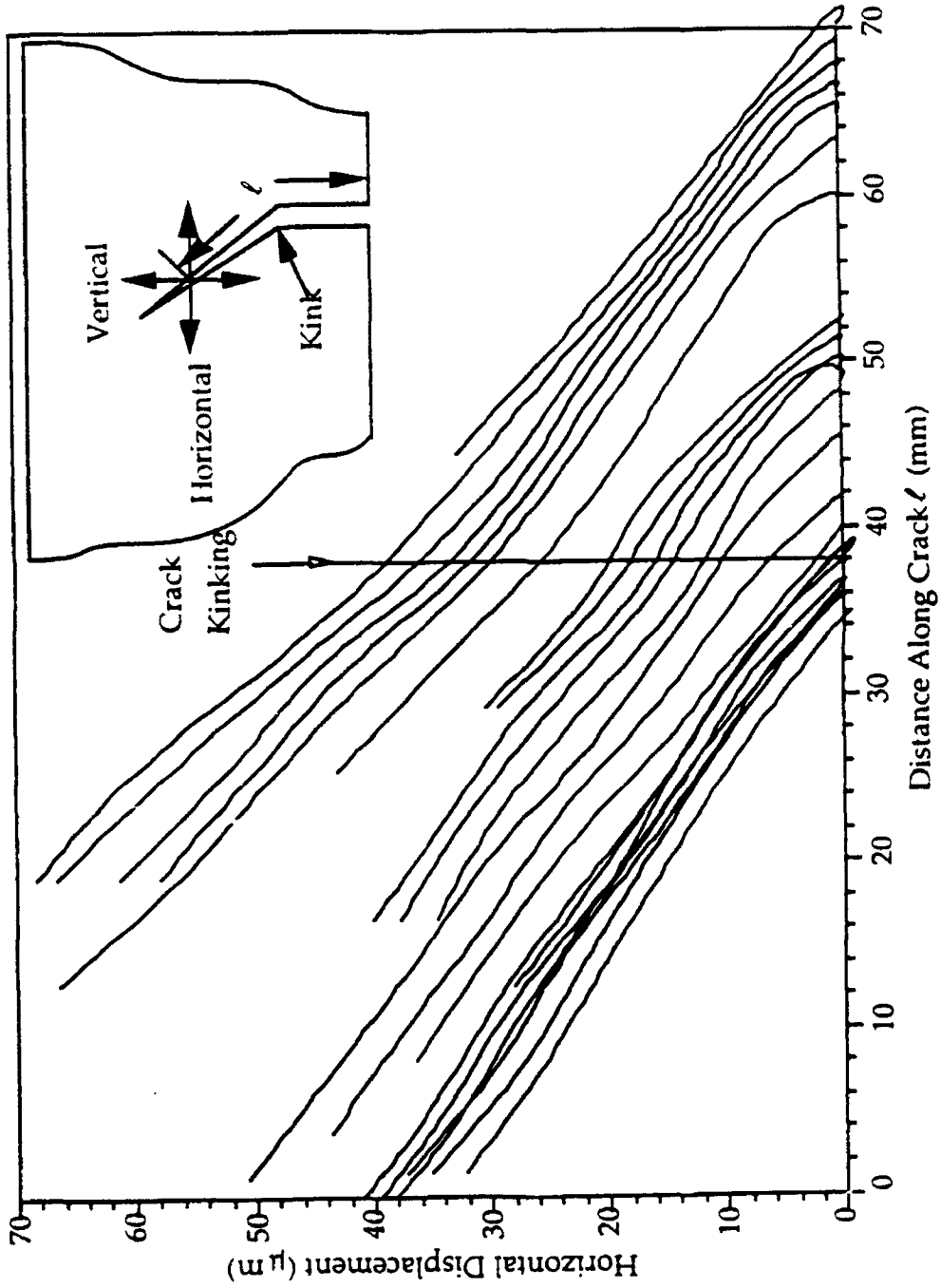

Figure 18. Sequence of Horizontal Displacement Along the Crack of Mixed Mode Dynamic Concrete Fracture

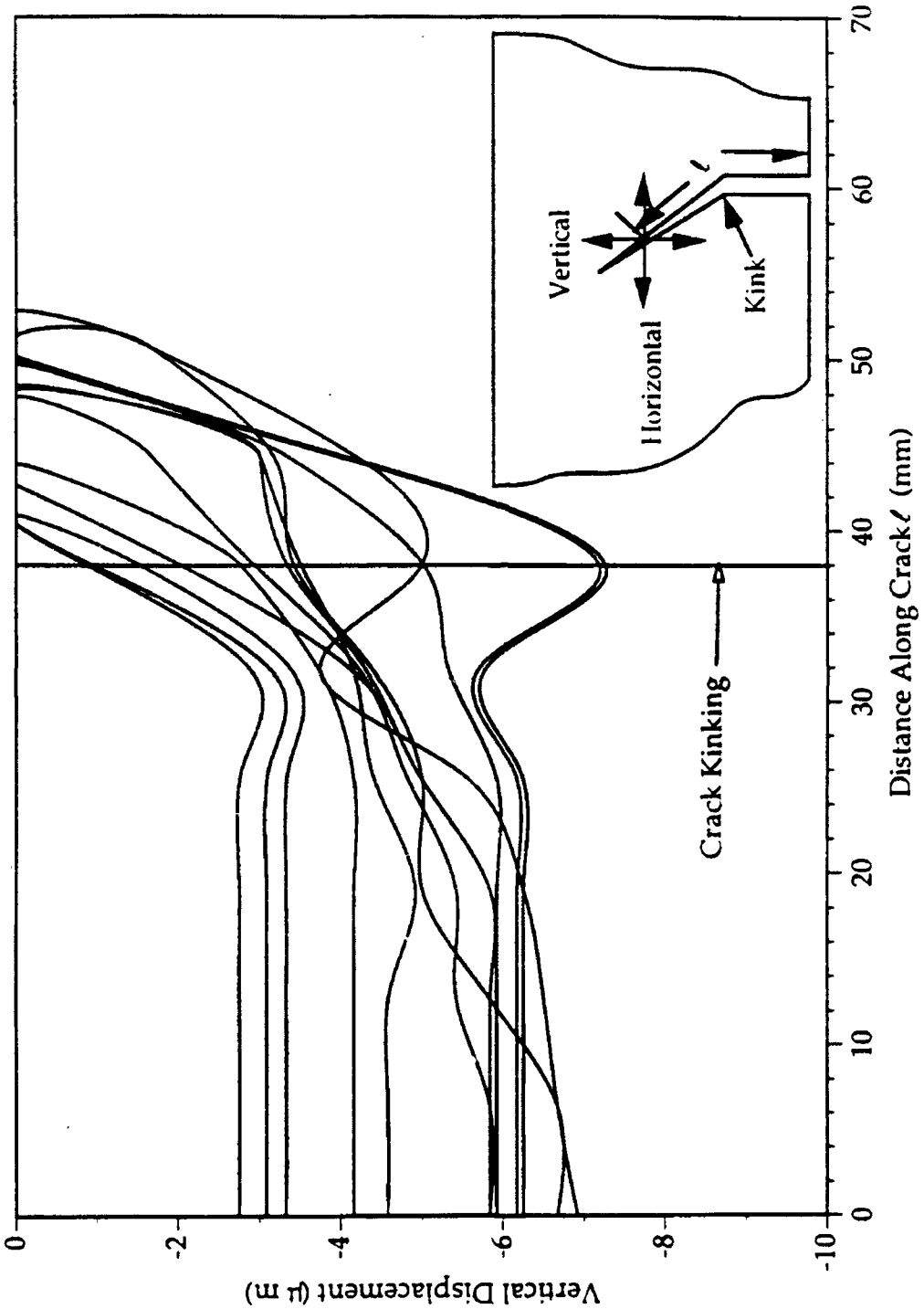

Figure 19. Sequence of Vertical Displacement Along the Crack of Mixed Mode Dynamic Concrete Fracture

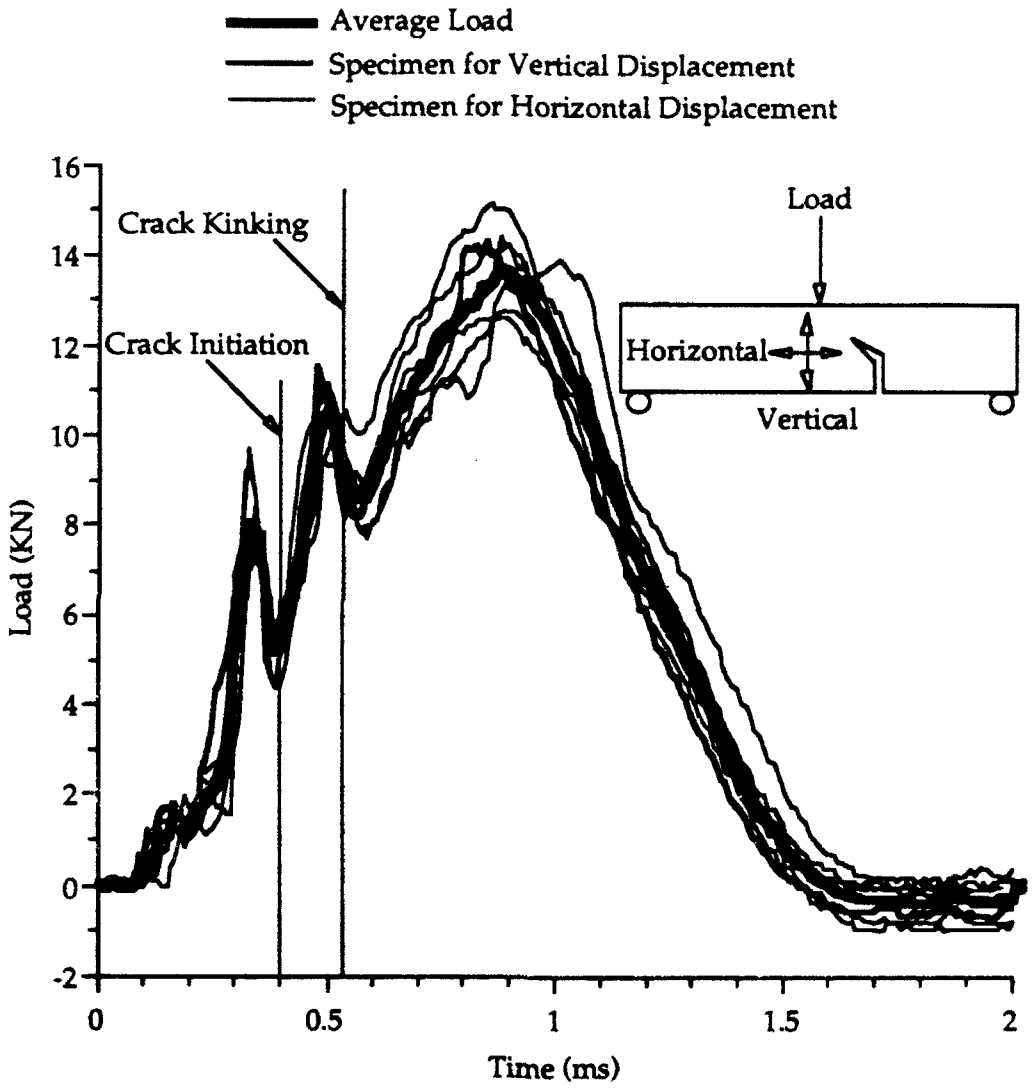

Figure 20. Loading History of Mixed Mode Dynamic Fracture Tests of Concrete.

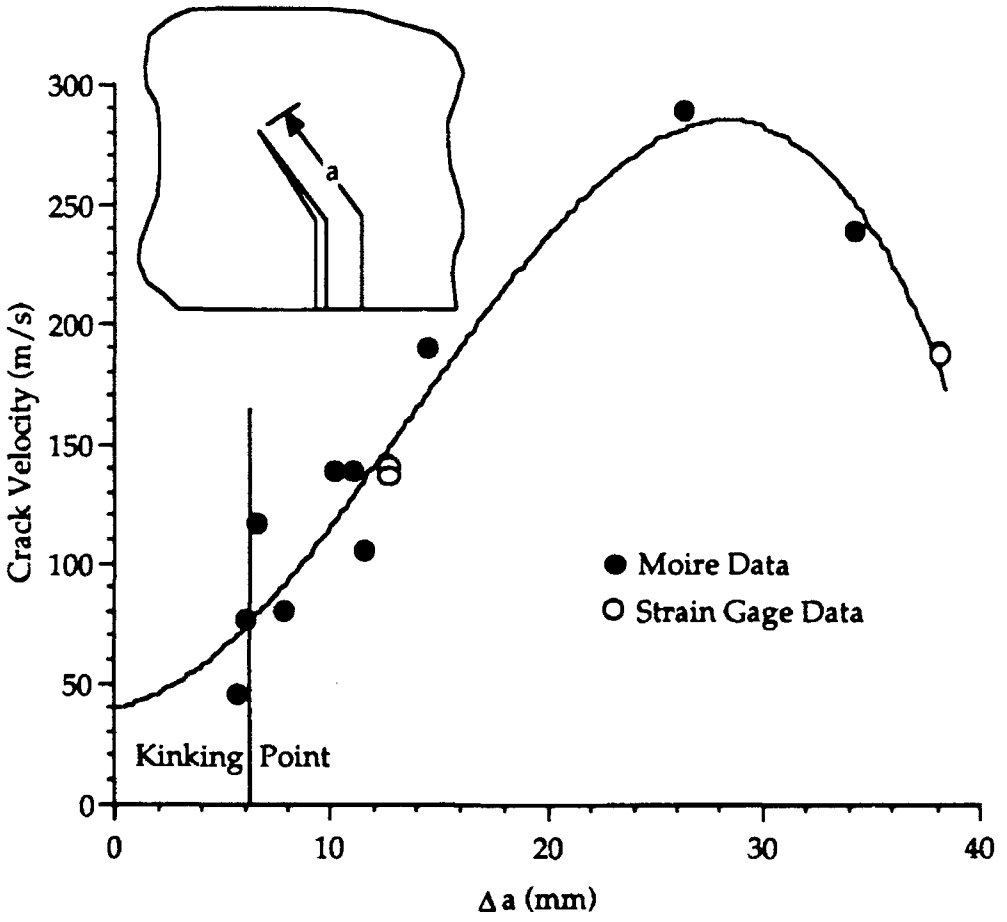

Figure 21. Experimental Crack Velocities.

the crack path can retard or deflect the propagating crack thus resulting in varying crack velocities during the fracture event. The exact precrack length is hard to control and thus mixed mode fracture is initiated at a slightly different precrack length. As a result, the kinking angle for each specimen is slightly different and affects the crack velocity. Despite this discrepancy, Figure 22 shows that the crack paths of all specimens fall into a narrow band width. The average kinking angle, 30.7° as shown in Figure 22, was thus used in the finite element analysis. Figure 21 shows tnat after kinking, the crack velocity reached a peak value and then dropped as the crack tip approached the compression side of the three point bend specimen. The curve fitted through all crack velocity measurements, as shown in Figure 22, was thus used to drive the dynamic crack propagation in the FEM model.

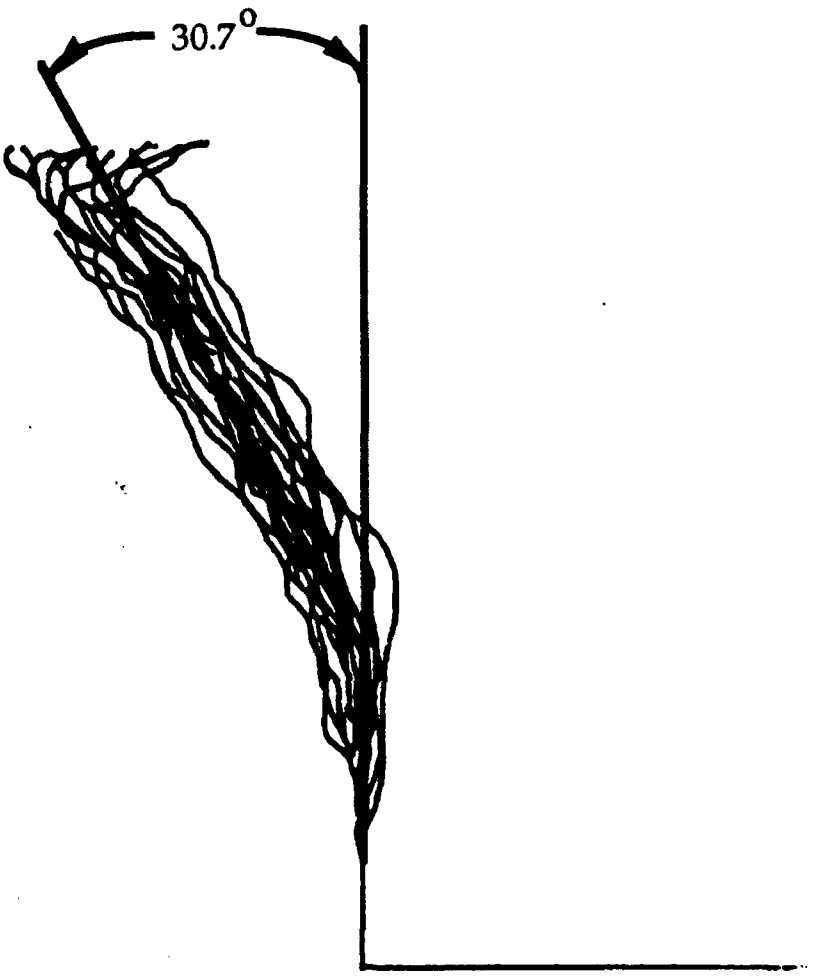

Figure 22. Mixed Mode Crack Paths.

CHAPTER 6
NUMERICAL RESULTS

6.1 Static Analysis

Figure 23 shows the CCS versus COD and the CSS versus CSD relations (constitutive relations) which provided the best fit between the measured and the computed COD's and CSD's. The corresponding computed COD's and CSD's are the circular data points in Figure 15. Also shown in Figure 23 is the CCS versus COD relation obtained from identical concrete fracture specimens which were tested under mode I loading. The CCS increased with increasing CSS for the first batch of fracture tests while a corresponding increase was not observed for the second batch of specimens with a less severely kinked crack and a lesser CSS versus CSD relation. It thus appears that there is additional friction generated by the interlocking force for a more severely kinked crack path that increases the CCS.

The mode II CSD versus CSS relation, which, as apparent from Figure 23, was far from complete due to the short FPZ in the three-point bend specimen, shows that the interlocking forces increased with increasing kinking angle. The decreasing CSS versus CSD relation contradicts the results of Walraven [14] and Reinhardt et al [15], in which an increasing relation was obtained.

Both K_I and K_{II} were computed separately for the first and second batches of fracture tests. Despite the differences in the average loads and the CSS versus CSD relations between the two batches of specimens, the stress intensity factors for the two batches practically coincided and thus single curves of K_I and K_{II} are presented in Figure 24. Figure 24 also shows that the K_I, which was determined previously by Guo et al [72] for Mode I loading, approaches the K_I of this study and suggests a unique K_I resistance curve for this concrete fracture specimen under mode I or mixed mode loading.

Figure 25 shows the energy partitions in the five three-point bend concrete specimens. The differences in the crack kinking angles in the two batches of concrete specimens resulted in the differences in the input work and hence in the partitioned energies. However, the dissipated energies in the fracture process zones and the slopes of the released energies in the two batches of specimens coincided.

Figure 26 shows the energy release and dissipation rates with crack extension in the five specimens. This energy dissipation rate relates only to the FPZ and does not include rates due to other energy sinks, such as micro-cracking ahead of the crack tip, crushing at the load and support points and aggregate-mortar debonding. The energy release rate Figure

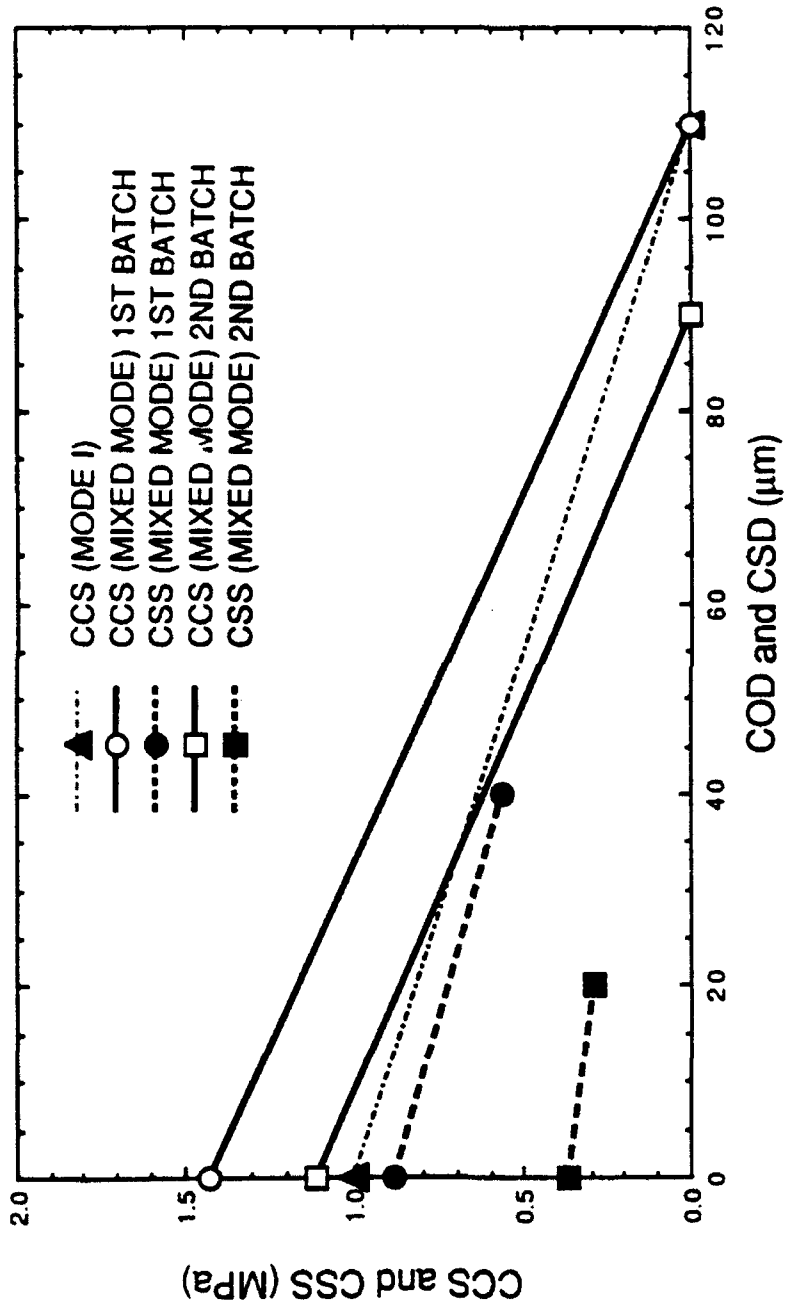

23. Constitutive Relations Governing the Fracture Process Zone

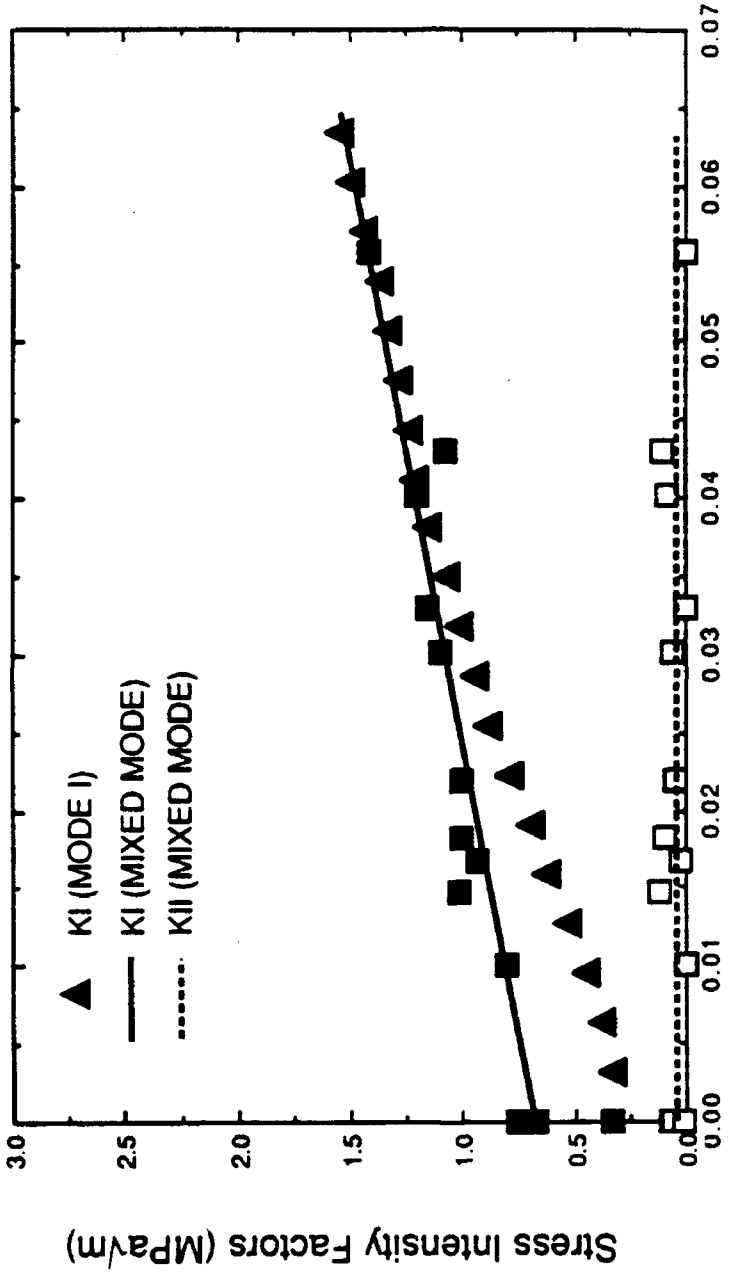

Figure 24. Variations in Stress Intensity Factors with Crack Extension

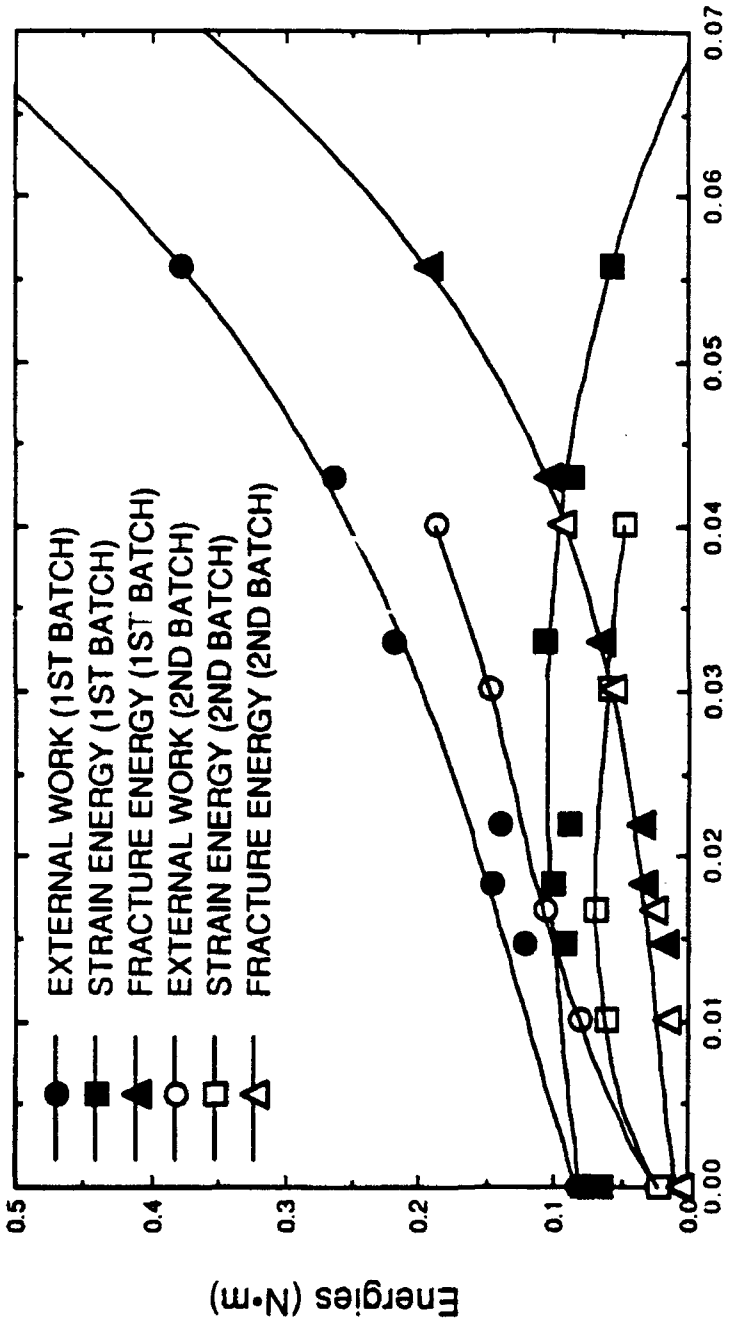

Figure 25. Energy participation in Concrete Bend Specimens

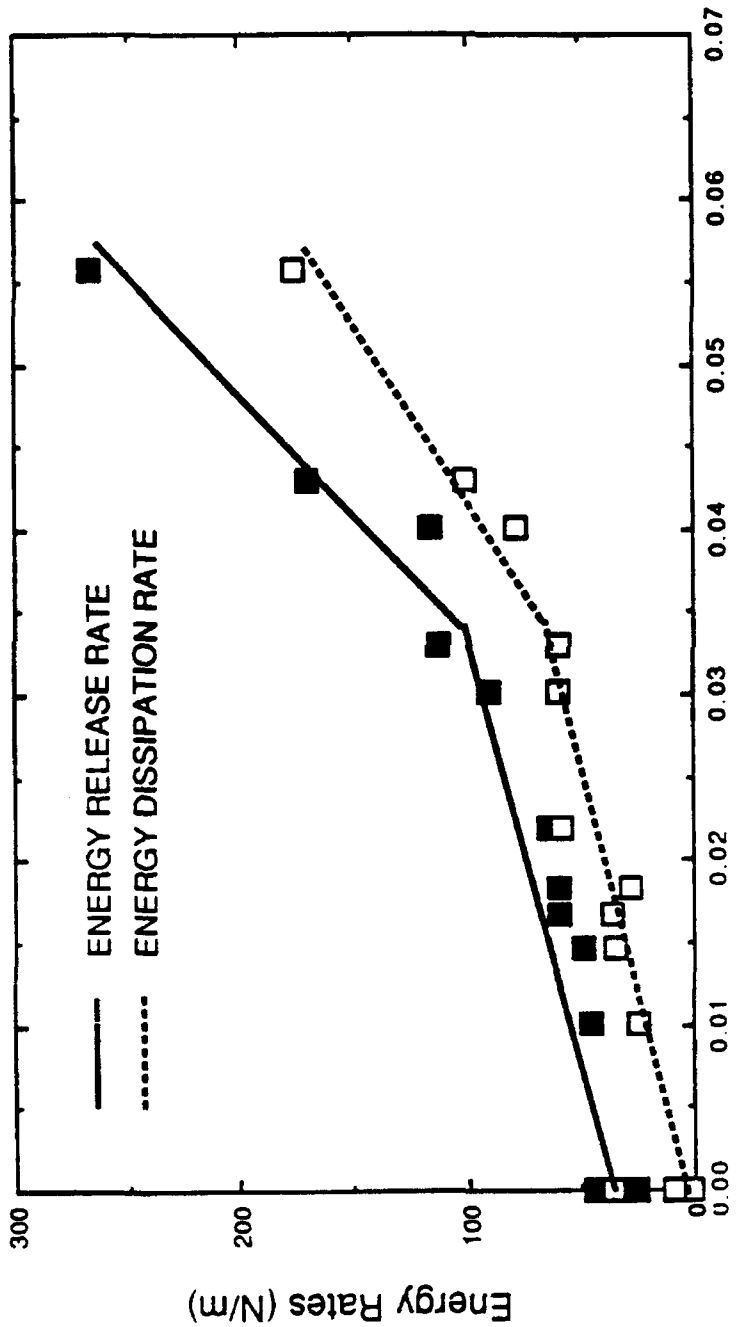

Figure 26. Energy Rates in Three-point Bend Concrete Specimens

represents the resistance curve for this mixed mode fracture process. Using the identical concrete fracture specimens, Guo et al [110] showed that the energy dissipation rate should remain constant after the FPZ is fully developed. Figure 26 shows that this not the case. As shown by Guo et al. [110] or mode I concrete fracture, the energy dissipation rate at the FPZ continues to be the dominant component of the energy release rate in mixed mode concrete fracture.

Figure 13 shows two load versus load-line displacement curves for each batch of specimens, one with and one without an FPZ. The correct curve, of course, is that with the FPZ included in computing the load-line displacement. For comparison purposes, the computation was repeated with the computed load-line displacement applied to the concrete specimen without the FPZ. Figure 13 shows that the resultant load carrying capacity for a given load-line displacement is reduced twenty percent for the peak load and in excess of fifty percent for the strain softening region when the FPZ is not included as compared to when the FPZ is included. This result underscores the additional role of the FPZ in increasing the load carrying capacity and post-peak stiffness of a fractured concrete beam.

The stress intensity factors in Figure 24 were used to predict the crack kinking angle in the presence of mixed mode loading. As shown in Table 3, the maximum circumferential stress criterion [111] provided a reasonable estimation of the crack kinking angle.

Table 3. The measured and predicted kinking angles of concrete specimens

	First batch specimens	Second batch specimens
Measured Kinking angle	30°	19°
Predicted kinking angle	31°	21.9°
Error	3.3%	15%

6.2 Dynamic Analysis

The dynamic finite element program computes COD and CSD with rapid crack extension. Figures 27 and 28 show the computed horizontal and vertical displacements along the crack. Due to crack kinking, a coordinate translation is necessary to convert the data to real crack opening and crack sliding displacements as shown in Figures 29 and 30, respectively

A complex and tedious inverse analysis procedure shown in Figure 9 was used to determine the constitutive relations in the FPZ. The final CCS versus COD curve and CSS versus CSD curve are shown in Figure 31. The maximum COD for FPZ is 160 μm. The maximum CCS is 3 MPa, and maximum CSS is 2 MPa.

The dynamic finite element analysis provided the total external work, strain energy, and kinetic energy. By using the constitutive relations, the energy dissipated in the FPZ can be computed. Figure 32 shows the energy partition during crack propagation. The energy rates can be obtained by differentiating the energy curves with respect to crack length for unit crack width. Figure 33 shows that all the energy rates are rising except the strain energy rate. The FPZ energy dissipation rate is over 80% of the energy release rate throughout crack propagation. This implies that the FPZ acts as the major energy sink during the mixed mode dynamic fracture of concrete.

One of the disadvantages of inverse analysis is that uniqueness of the solution is not guaranteed. Thus, in the following, a procedure for validating the mixed mode FPZ model is presented.

6.2.1 Strain Gage Data

The advantage of the hybrid experimental-numerical analysis is that it provides more information than needed. Some of the FEM output data were used to validate the concrete fracture model used in the analysis. For example, the strain gage data measured in the experiments were compared with the computed strains and thus served to verify the FEM model.

Three strain gages were mounted on the predicted crack path as shown in Figure 34 in the dynamic concrete fracture test. A very sharp rise in strain gage signal indicated the passage of the crack through the gage. The crack velocity was calculated by measuring the spacing between the strain curves, since the slopes of the sharp rising strain curves are almost parallel before the strain gages were broken. Unfortunately, due to triggering setup errors, only few useful strain gage data from the three point bend

concrete specimens were obtained. Despite the scatter in crack velocities due to grain boundary effect, the velocities obtained from the moire interferometry and strain gage data fell within the same scatter band. The crack velocities obtained from strain gage data by Du [5], Yon [7], and Guo [112] who used the same type of specimen, are of the same order of magnitude and are qualitatively similar, as shown in Figure 35. The differences can be attributed to the fact that all these tests involved only mode I fracture, in contrast to the mixed mode fracture involved in this study. The strain data from Guo's tests (open square) show the same trend of crack velocity change although the magnitude and location of the peak point are different from those of this research. The differences are caused by the different off-set distances of 3-point bend impact tests.

6.2.2 Strain Histories

The strain data were also compared with the LEFM dynamic finite element computation. The strains, before the crack propagated through the gages, were calculated by the FEM model and were interpolated to provide strains at the same locations as strain gages. Figure 36 shows the FEM and experimental strain curves at two strain gage locations for mixed mode dynamic concrete fracture. Although the crack initiation times are quite different, the shapes of the experimental and FEM strain data are generally similar. The difference is due to the average value in the FEM input data and the scatter in the experimental data.

The distance between the two strain curves represents the period of time the crack propagates between the gages. As shown in Figure 36, T_1, which is the crack propagation time obtained from FEM, is fairly close to T_2, which is obtained from experimental data. In short, the two sets of curves are qualitatively and quantitatively similar, which validates the crack velocity used in the analysis.

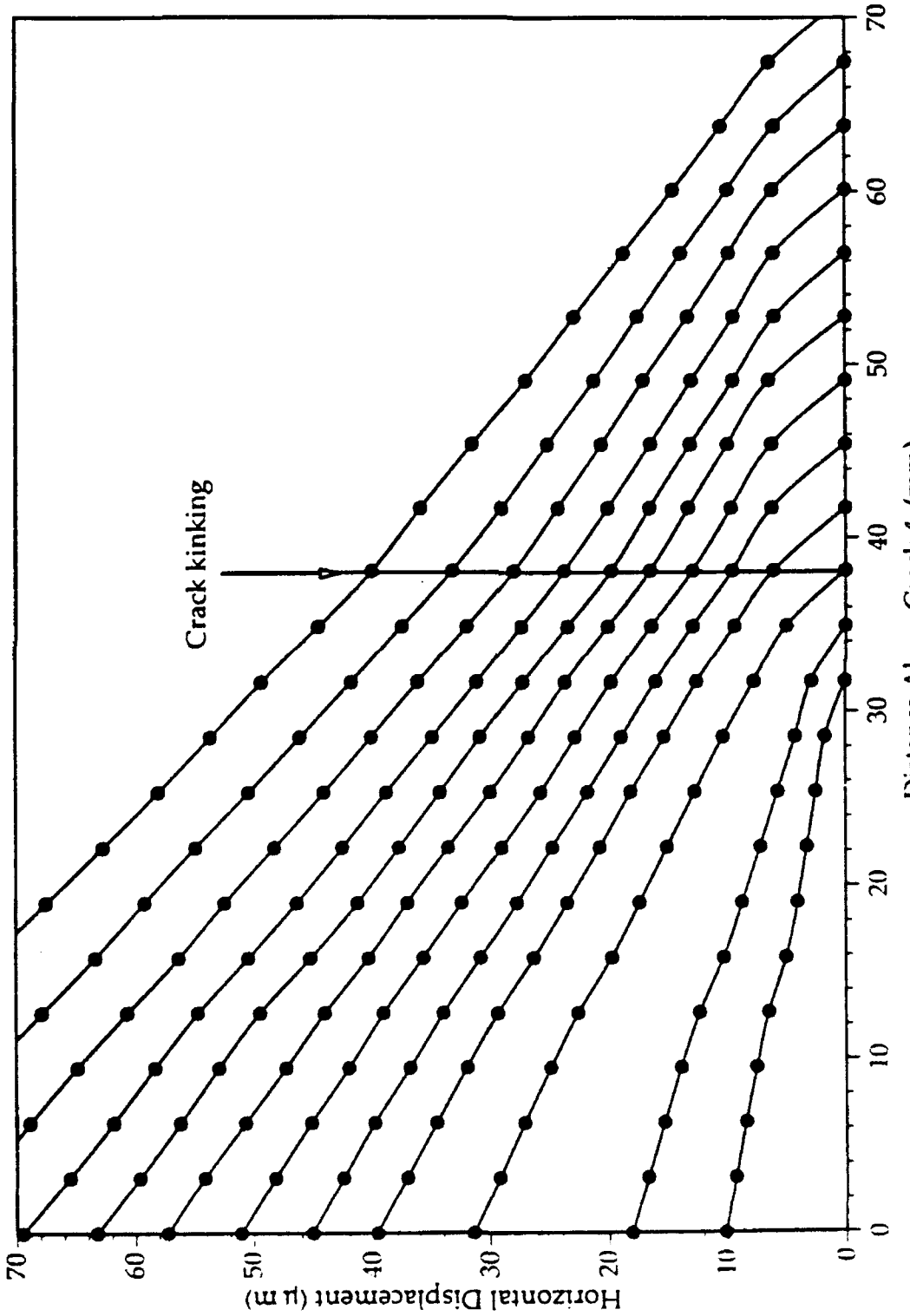

Figure 27. Computed Horizontal Displacement Along the Crack of Mixed Mode Dynamic Concrete Fracture.

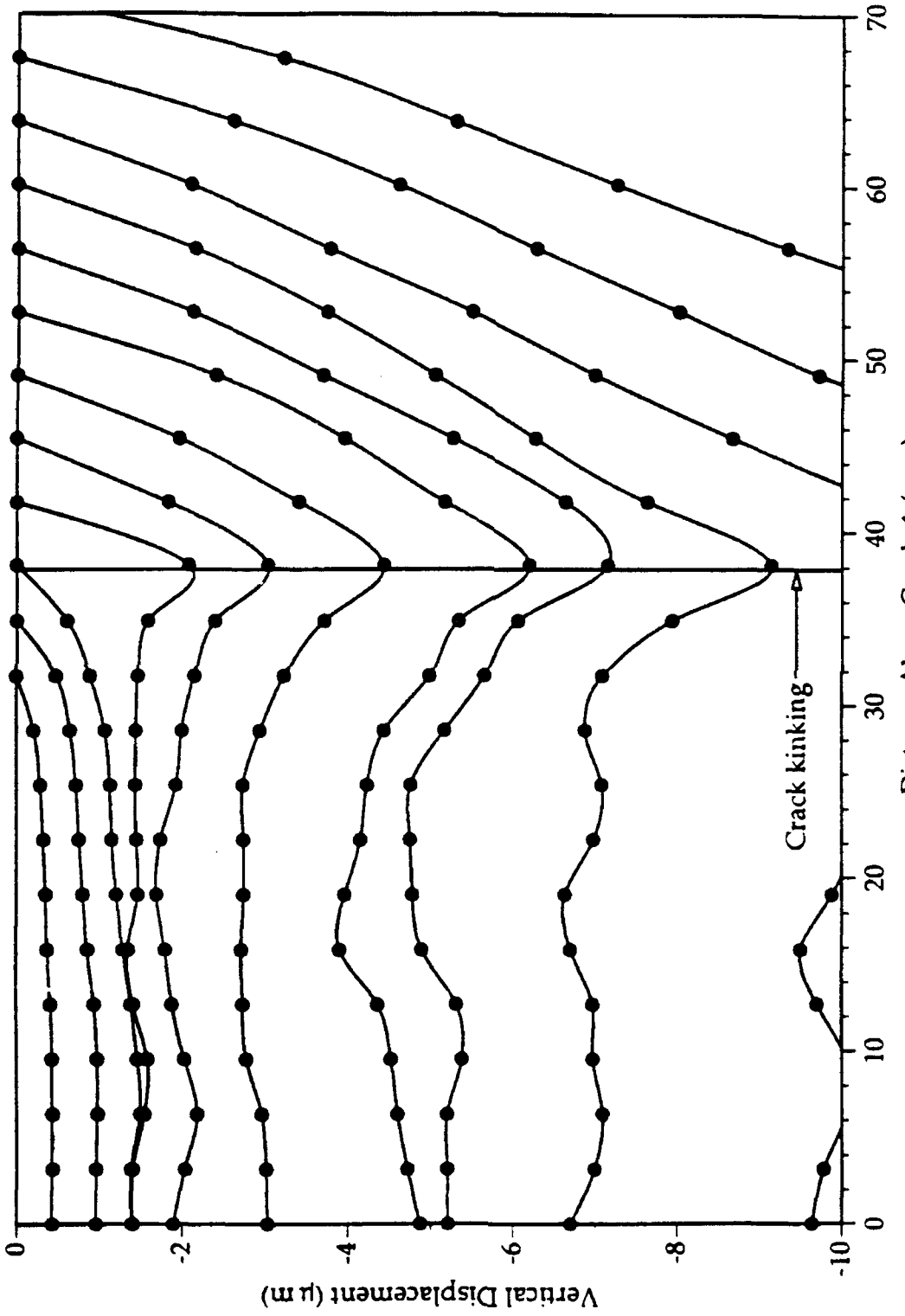

Figure 28. Computed Vertical Displacement Along the Crack of Mixed Mode Dynamic Concrete Fracture.

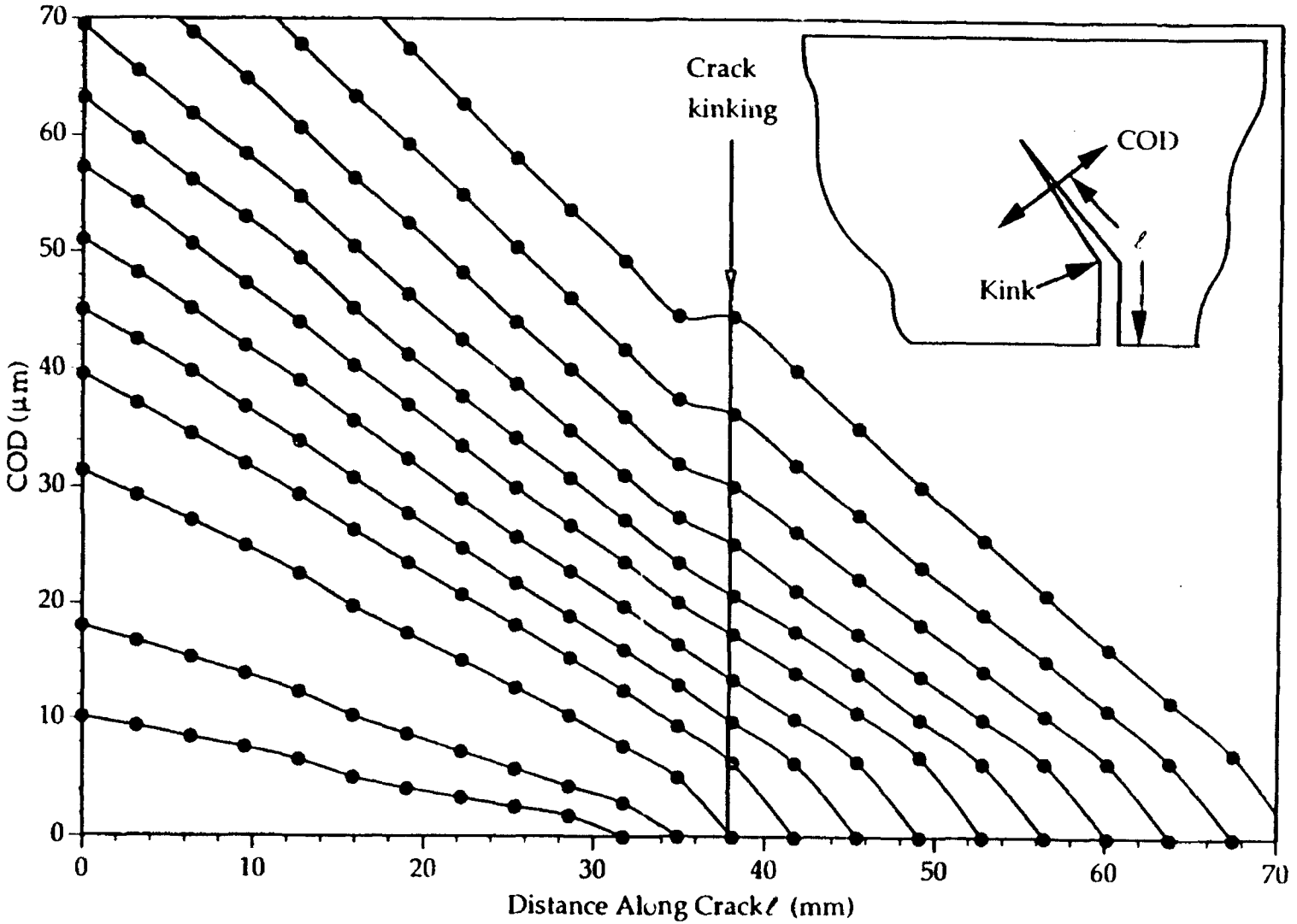

Figure 29. COD Along the Crack of Mixed Mode Dynamic Concrete Fracture.

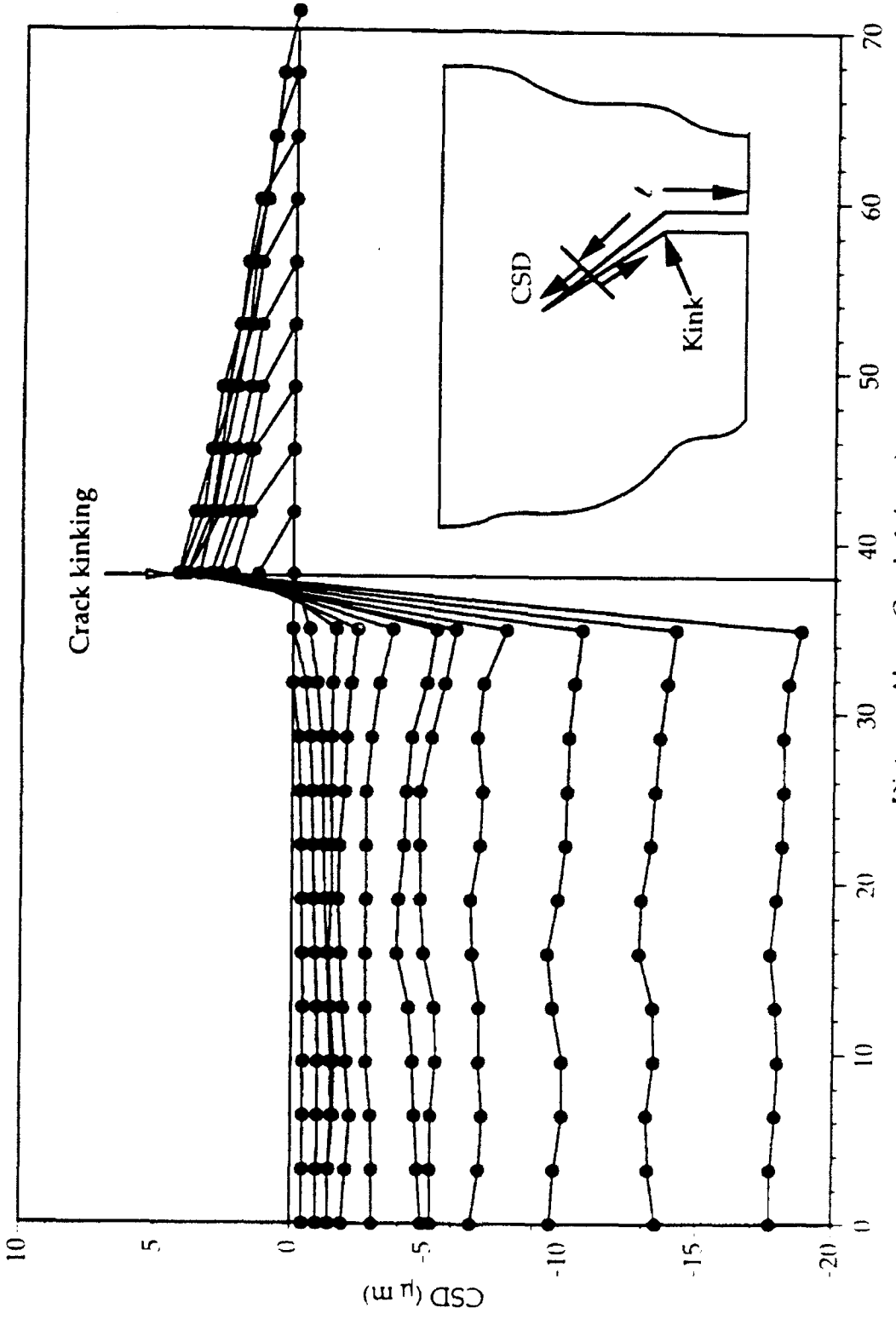

Figure 30. CSD Along the Crack of Mixed Mode Dynamic Concrete Fracture.

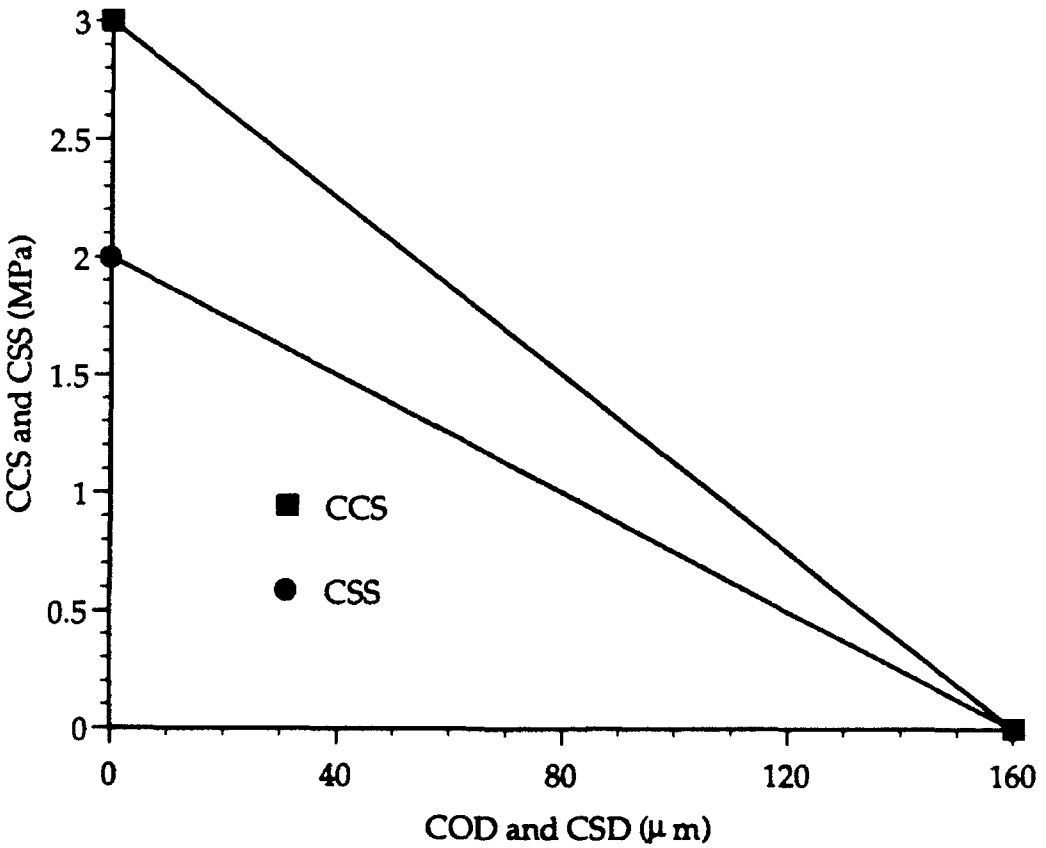

Figure 31. Crack Opening and Crack Sliding Constitutive Relations.

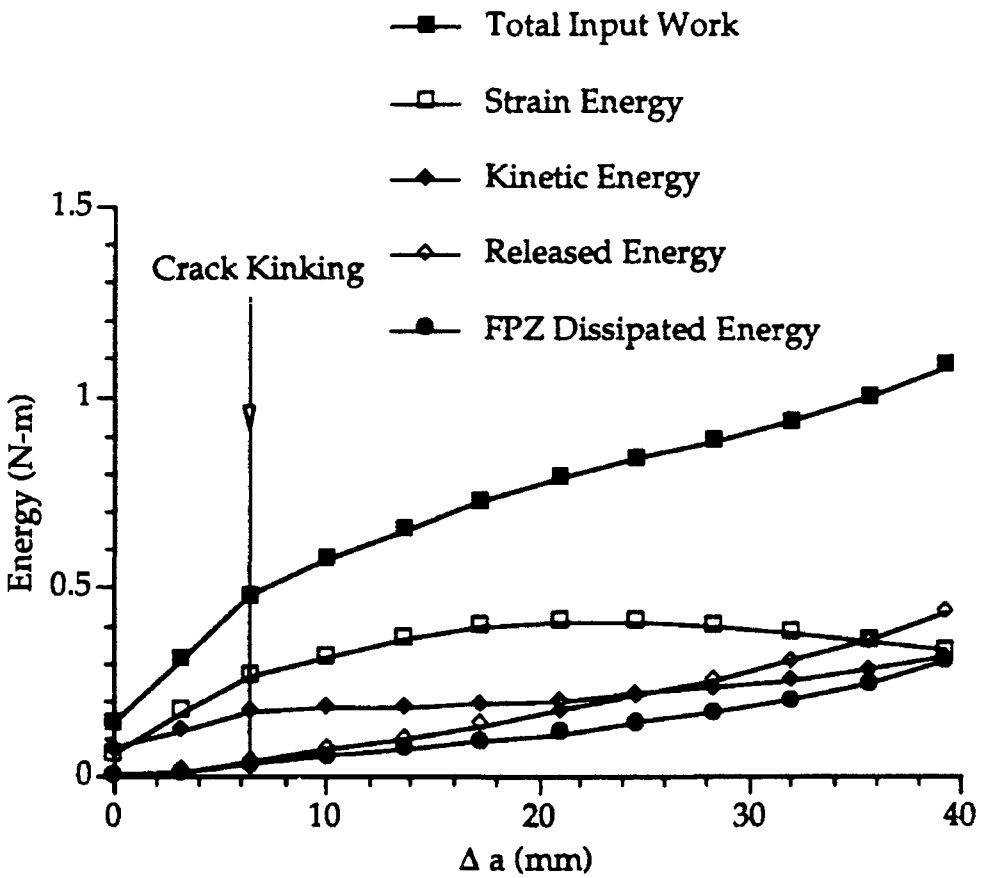

Figure 32. Energy Partition During Dynamic Crack Propagation.

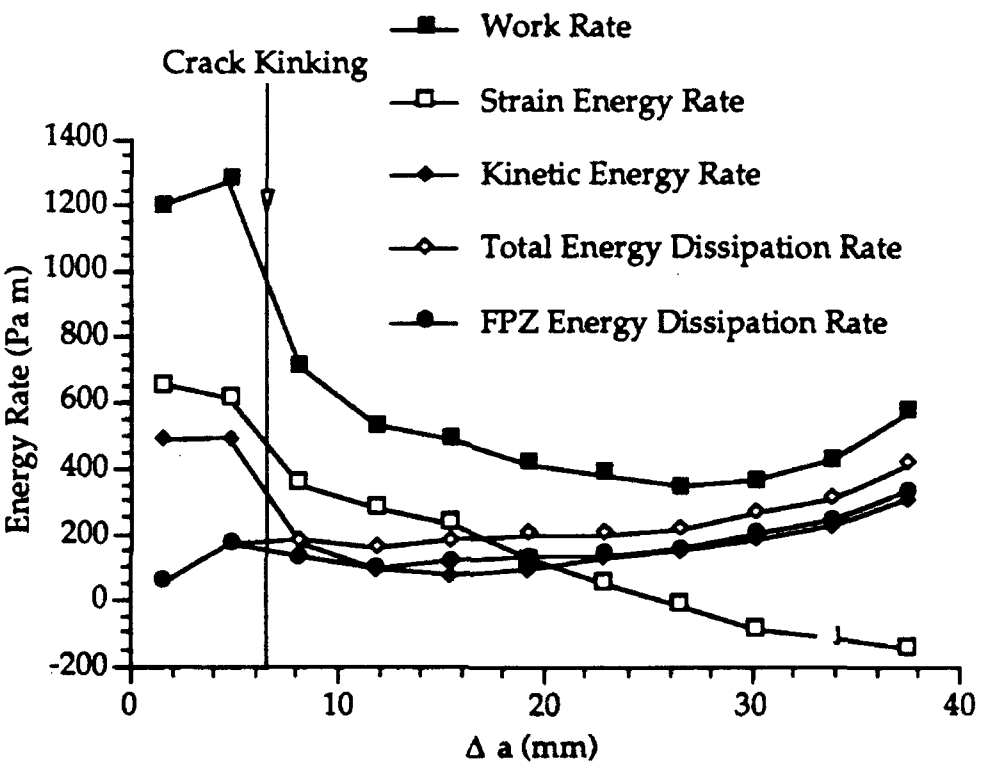

Figure 33. Energy Rates for Mixed Mode Dynamic Concrete Fracture.

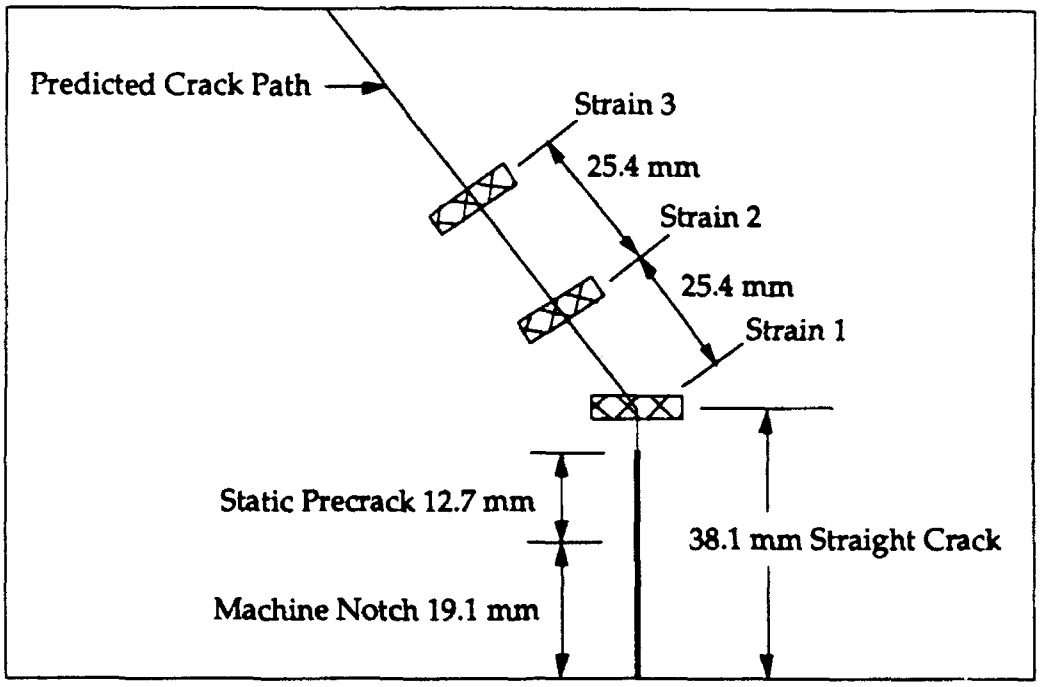

Figure 34. Locations of Strain Gages.

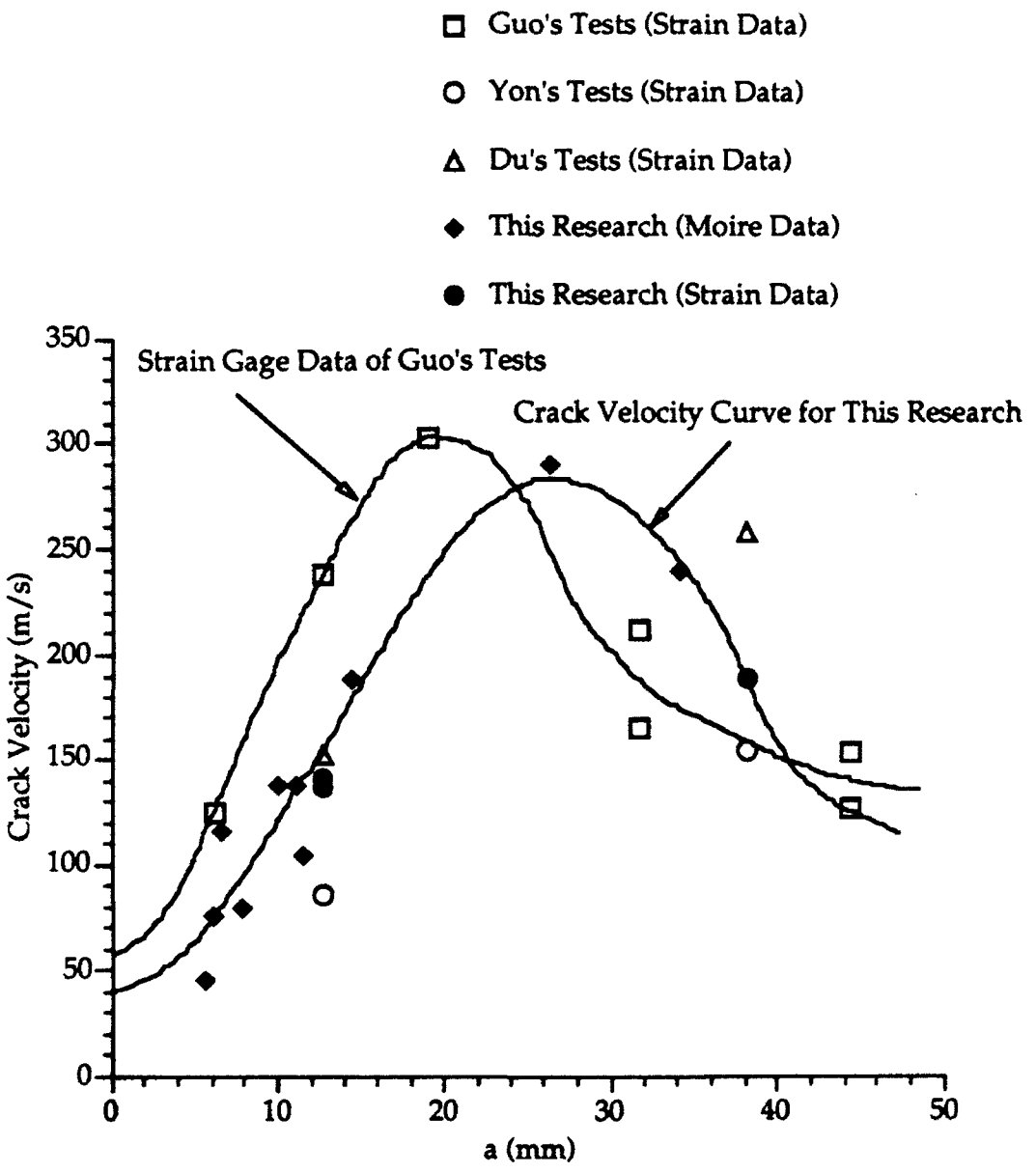

Figure 35. Comparison of Crack Velocities.

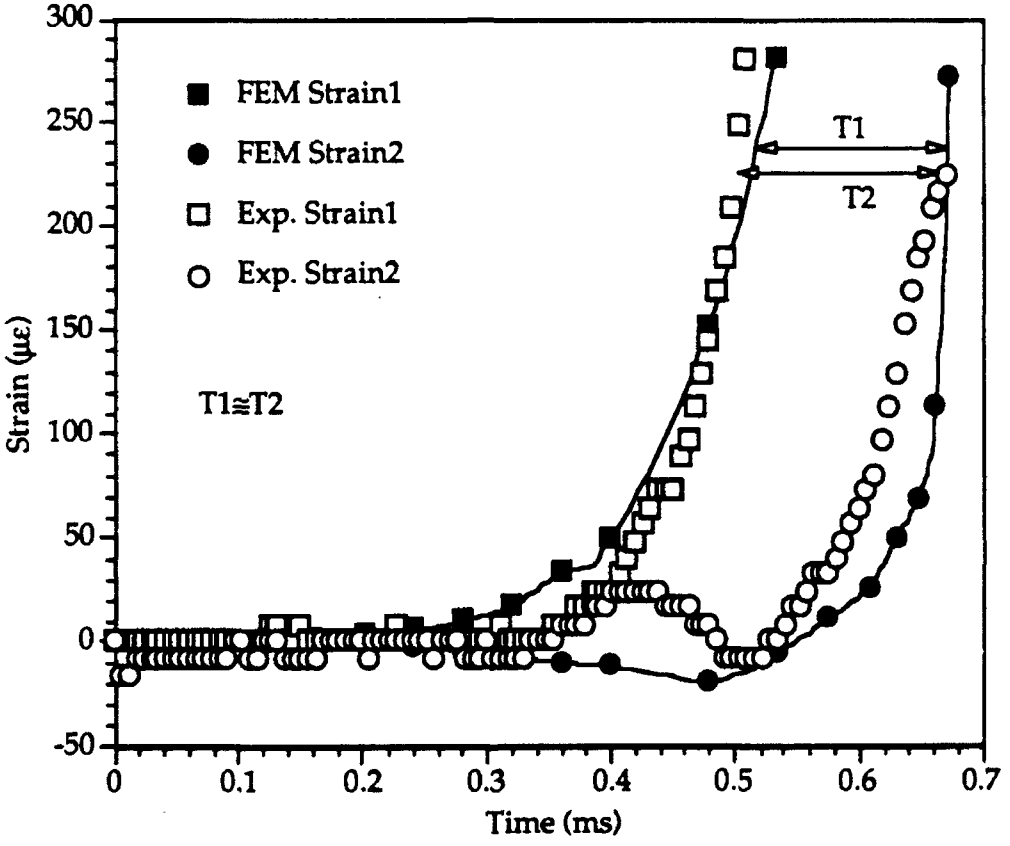

Figure 36. Comparison of Experimental and FEM Strain Curves.

CHAPTER 7
DISCUSSION

The constitutive relations of FPZ obtained from this analysis are compared with experimental results previously obtained. Figure 37 shows the constitutive relationships for the same mix proportion of concrete but of different tests. The solid symbols with solid lines are obtained from dynamic fracture tests and open symbols with dashed lines are from static tests. The square symbols are for CCS and circle symbols are for CSS in mixed mode fracture. The diamond symbols arc for the pure mode I tests. The dynamic fracture tests show higher maximum CCS and CSS than those of the static tests. The CCS curve of mixed mode static test is higher than that of mode I case probably because the contact pressure on the frictional surface increased with the sliding displacement. While the maximum CCS of dynamic mixed mode is lower than that of pure mode I case, the maximum COD of this research is higher than that of pure mode I. The total effect of FPZ is higher in mixed mode case due to the same reason as of static case.

Figure 48 shows the averaged measured load versus computed load-line displacement relations for the mixed mode dynamic loading up to the point of the end of analysis. Another load history curve, which was generated by the FEM model without FPZ and with the same load-line displacement, is also shown in Figure 48. The comparison shows that the FPZ increases the load carrying capacity significantly.

In concrete, the fracture process is not completed until the material separates with no crack closing forces on the fracture surfaces. This concept explains why the traditional fracture mechanics concepts cannot be used directly for fracture analysis of composite materials and indicates the nature of the model that must be developed for this kind of structural material.

It was found that the influences of FPZ characteristics of ceramic matrix composite and concrete was very similar. The fracture energy dissipation mechanism of concrete looks like an enlarged dissipation mechanism of ceramic matrix composite. Both the ceramic matrix and the hardened cement paste are brittle materials. The microcrackings in concrete are similar to the debondings between matrix and whiskers. The grains and whiskers in ceramic matrix composite work like the aggregates in concrete. They both generated the CCS behind the crack tip throughout the fracture surface interlocking. The nonlinear behavior of ceramic composites and concrete can both be explained by using the

constitutive relationship of FPZ. This similarity suggests the commonalty in FPZ phenomenon of semi-brittle structure composites.

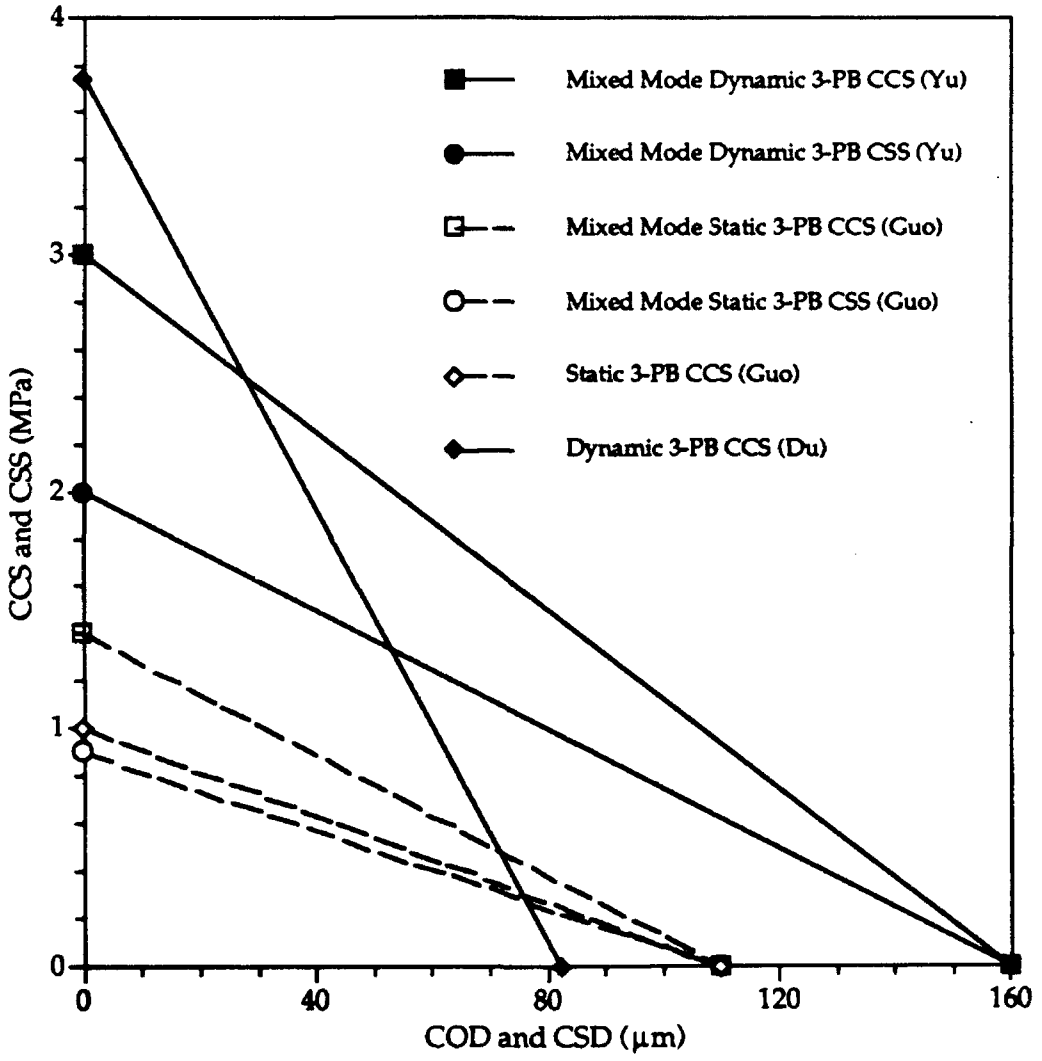

Figure 37. Constitutive Relations in FPZ.

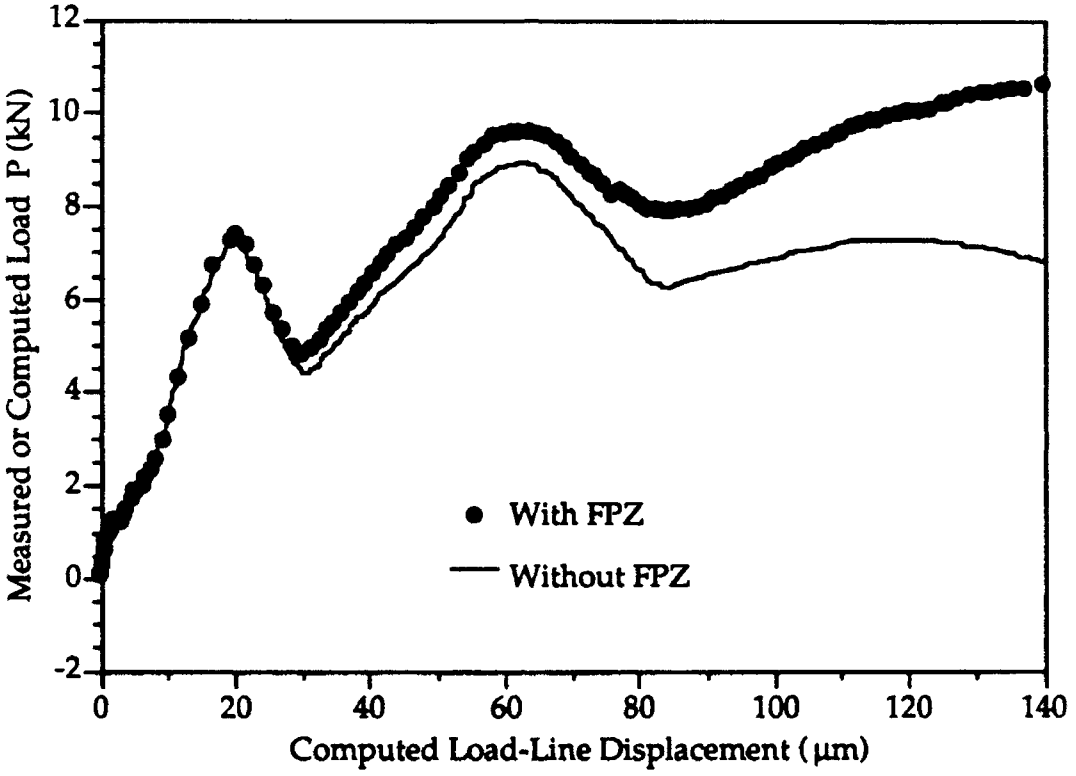

Figure 38. Load Versus Load-Line Displacement Curves

CHAPTER 8
CONCLUSIONS AND RECOMMENDATIONS

8.1 Static Analysis

1. Constitutive relations for crack bridging and interlocking in off-set three-point bend concrete specimens were obtained.
2. For given crack opening displacements, the crack closing stress increased with increased crack shearing stress.
3. The dominant energy dissipation mechanism in concrete fracture is crack bridging and interlocking in the fracture process zone.
4. For these off-centered single-edged precracked specimens the crack extends under Mode I crack opening with vanishing K_{II}.
5. The presence of a fracture process zone increased the load carrying capacity of the concrete fracture specimen at a given displacement compared to that predicted for the same specimen without such a zone.

8.2 Dynamic Analysis

The results of the mixed mode dynamic fracture analysis of concrete can be summarized as follows:

1. The dynamic moire technique was successfully applied to record the dynamic event of mixed mode dynamic fracture of the three point bend concrete specimens.

2. A two dimensional FEM model for mixed mode dynamic fracture of concrete was developed.

3. A hybrid experimental-numerical analysis procedure was developed to extract the dynamic fracture properties of concrete.

4. The CCS versus COD curve and CSS versus CSD curve in FPZ were obtained through the inverse analysis.

5. A dynamic fracture model with FPZ for explaining the nonlinear behavior of concrete was successfully developed.

8.3 General Conclusions

From the conclusions obtained through static and dynamic analyses of concrete fracture, the following general conclusions can be drawn:

1. The energy dissipation rate in FPZ gradually became the dominant energy dissipation mechanisms of concrete fracture as the crack extended.

2. The CCS effect of mixed mode concrete fracture is more prominent than that of mode I case, implying that the CCS-COD and CSS-CSD relations are interrelated.

3. The fracture process of brittle structure composites includes microcrack, macrocrack, and interlocking mechanisms in FPZ. The traditional fracture mechanics concepts cannot be applied directly.

8.4 Recommendations

Based on the present study, the following possible improvements and further investigations are recommended:

1. Apply the modified four-beam optical system to record the horizontal and vertical displacements simultaneously using some image separating set up.

2. Run more tests using a wide range of delay times to cover the fracture process from initiation to complete failure.

3. Apply two non-contact displacements gages to both sides of the concrete specimen to obtain the averaged load point displacement and filter out the error caused by tilting.

4. Apply more strain gages at strategic positions to check the velocity change through the whole fracture process.

5. Run dynamic tests with a different drop weight and drop height to investigate crack resistance as a function of loading rates.

6. Systematically change the offset distance of the precrack, and check the influence of mode II fracture on crack kinking angle and dissipation energy.

7. Examine the fracture surface of broken concrete specimens to study the influence of the fracture surface morphology on crack resistance.

8. Design an analysis to study the interrelation of CCS versus CSD and CSS versus COD.

REFERENCES

1 A. Hillerborg, M. Modeer, and P. E. Petersson, "Analysis of Crack Formation and Crack Growth in Concrete by Means of Fracture Mechanics and Finite Elements," *Cement and Concrete Research*, 6, 773-782 (1976).

2 H. W. Reinhart, A. W. Cornelissen, and D. A. Hordjik, "Tensile Tests and Failure Analysis of Concrete," *ASCE J. of Struct. Eng.*,112 (11), 2462-2477, (1986).

3 M. Wecharatana, and S. P. Shah, "Prediction of Non-linear Fracture Process Zone in Concrete," *ASCE J. Eng. Mech.*,109 (5), 1231-1246 (1983).

4 S. Cedolin, S. D. Poli, and I. Iori, "Experimental Determination of the Fracture Process Zone in Concrete," *Cement and Concrete Research*, 13, 557-567 (1983).

5 J. J. Du, A. S. Kobayashi, and N. M. Hawkins, "Fracture Process Zone of a Concrete Fracture Specimen," *Proceeding of SEM-RILEM International Conference on Fracture of Concrete and Rock*, ed. S. P. Shah and S. E. Swartz, Springer-Verlag,199-204 (1989).

6 R. A. Miller, S. P. Shah, and H. I. Bjelkhagen, "Crack Profiles in Mortar Measured by Holographic Interferometry," *Experimental Mechanics*, 28 (4), 388-394 (1988).

7 J.-H. Yon, N. M. Hawkins, Z.-K. Guo, and A. S. Kobayashi, "Fracture Process Zone Associated with Concrete Fracture," *Fracture Process in Concrete, Rock and Ceramics*, eds. J. G. M. van Mier, J.G. Rois and A. Baker, E & F Spon, London, 485-494 (1991).

8 S.E. Swartz, L.W. Lu, L.D. Tang, and T.M. Refai, "Mode II Fracture Parameter Estimates for Concrete from Beam Specimens," *Experimental Mechanics*, 28, 2, 146-153 (1988).

9 Y.S. Jenq and S.P. Shah, "Mixed Mode Fracture of Concrete," *International Journal of Fracture*, vol. 38, 123-142 (1988).

10 Y.S. Jenq and S.P. Shah, "On the Fundamental Issues of Mixed Mode Concrete Crack Propagation in Concrete," *Fracture of Concrete and Rock, Recent Developments*, eds. S.P. Shah, S.E. Swartz and B. Barr, Elsevier Applied Science, 27-38 (1989).

11 J. Davies, "Study of Shear Fracture," *Fracture of Concrete and Rock, Recent Developments*, eds. S.P. Shah, S.E. Swartz And B. Barr, Elsevier Applied Science, 438-446 (1989).

12 W. Wong and R.A. Miller, "Mixed Mode Fracture at Early Age," *Micromechanics of Failure of Quasi-brittle Materials*, eds. S.P. Shah, S.E. Swartz and M.L. Wang, 166-175 (1990).

13 M.B. Nooru-Mohamed and J.G.M. van Mier, "Fracture of Concrete Under Mixed-Mode Loading," *Fracture of Concrete and Rock, Recent Developments*, eds. S. P. Shah, S.E. Swartz and B. Barr, Elsevier Applied Science, 458-467 (1989).

14 J.C. Walraven, "Fundamental Analysis of Aggregate Interlock," *ASCE Journal of Structure Division*, 107, 11, 2245-2270 (1981)

15 H.W. Reinhardt and J.C. Walraven, "Cracks in Concrete Subjected to Shear," *ASCE Journal of Structure Division*, 108, 1, 207-224 (1982).

16 B.M. Liaw, F.L. Jeang, N.M. Hawkins, and A.S. Kobayashi, "Fracture Process Zone for Mixed Mode Concrete Fracture," *ASCE Journal of Engineering Mechanics*, 116, 7, 1560-1579 (1990).

17 *Cement-Based Composites: Strain Rate Effects on Fracture*, eds. S. Mindess and S.P. Shah, Materials Research Society Symposia Proceeding Vol. 64, 1986

18 S. Mindess, "Rate of Loading Effects on the Fracture of Cementitious Materials," *Application of Fracture Mechanics to Cementitious Composites*, ed. S.P. Shah, Martinus Nijhoff Publishers, 1985, pp. 617-636.

19 A. Benton, S. Mindess, and N. Benthur, "The Behavior of Concrete Under Impact Loading: Experimental Procedures and Methods of Analysis," *Materials and Structures*, Vol. 19, no. 113, 1986, pp. 371-378.

20 S. Mindess, and A. Benton, "A Preliminary Study of the Fracture of Concrete Beam Under Impact Loading Using High Speed Photography," *Cement and Concrete Research*, Vol. 15, 1985, pp. 474-484.

21 S. Mindess, N.P. Banthia, A. Ritter, and J.P. Skalny, "Crack Development in Cementitious Materials Under Impact Loading," *Cement-Based Composites: Strain Rate Effects on Fracture*, eds. S. Mindness and S.P. Shah, Material Reserach Society Symposia Proceedings, Vol. 64, 1986, pp. 217-224.

22 A. Benton, S. Mindess, and N.P. Banthia, "The Fracture of Reinforced Concrete Under Impact Loading," ibid. loc. cit., pp. 225-234.

23 R. John and S.P. Shah, "Fracture of Concrete Subjected to Impact Loading," *Cement, Concrete and Aggregates*, ASTM CCAGDP, Vol. 8, No. 1, Summer 1986, pp. 24-32.

24 S.P. Shah, and R. John, "Rate-Sensitivity of Mode I and Mode II Fracture of Concrete," *Cement-Based Composites: Strain Rate Effects on Fracture*, eds. S. Mindess and S.P. Shah, Material Research Society Symposia Proceedings Vol. 64, 1986, pp. 21-38.

25 S.P. Shah, "Concrete and Fiber Reinforced Concrete Subjected to Impact Loading," ibid. loc. cit., pp. 181-202.

26 H.W. Reinhardt, "Tensile Fracture of Concrete at High Rates of Loading," *Application of Fracture Mechanics to Cementitious Composites*, ed. S.P. Shah, Martinus Nijhoff Publishers, 1985, pp. 459-590.

27 J. Weerheijm, and H.W. Reinhardt, "Modelling of Concrete Fracture Under Dynamic Tensile Loading," *Fracture of Concrete and Rock: Recent Developments*, eds. S.P. Shah, S.E. Swartz and B. Barr, Elsevier Applied Science, 1989, pp. 721-728.

28 M. Arzamendi, R.L. Sierakowski, and W.E. Wolfe, "Determination of the Fracture Toughness Parameters for an MDF Cement Composite," *Cement-Based Composites: Strain Rate Effects on Fracture*, eds. S. Mindess and S.P. Shah, Materials Research Society Symposia Proceedings Vol. 64, 1986, pp. 257-265.

29 N.M. Hawkins, A.S. Kobayahsi, and J.J. Du, "An Impact Damage Model of Concrete," *Cement Based Composites: Strain Rate Effects of Fracture*, eds. S. Mindess and S.P. Shah, Material Reaseach Society, Pittsburgh, 1986, pp. 203-215.

30 J.J. Du, A.S. Kobayashi, and N.M. Hawkins, "FEM Dynamic Fracture Analysis of Concrete Beams," *Journal of Engineering Mechanics*, Vol. 115, No. 10, October, 1989.

31 H. Green, "Impact Strength of Concrete," *Proc. of Inst. of Civil Engineering*, Vol. 28, pp. 361-396.

32 W. Goldsmith, M. Polivka, and T. Yang,, "Dynamic Behavior of Concrete," *Experimental Mechanics*, Vol. 6, No. 2, Feb. 1966, pp. 65-79.

33 T.C. Hsu, F.O. Slate, and G.M. Sturman, "Microcracking of Plain Concrete and Shape of the Stess-Strain Curve," *Journal of the American Concrete Institute*, Vol. 60, 1963, pp. 209-224.

34 L. Cedolin, S. Dei Poli and I. Iori, "Experimental Determination of the Stress-Strain Curve and Fracture Energy for Concrete in Tension," *Proceedings of International Conference on Constitutive Laws for Engineering Materials*, University of Arizona, 1983, pp. 393-398.

35 M.F. Kaplan, "Crack Propagation and Fracture of Concrete," *ACI Journal*, Vol. 58, No. 5, November 1961, pp. 591-610.

36 J. Glucklich, "Fracture of Plain Concrete," *Engineering Mechanics Division Journal*, ASCE, Vol. 89, No. EM6, December 1963, pp. 127-138.

37 A. Hillerborg, "Analysis of One Single Crack," *Fracture Mechanics of Concrete*, ed. F.H. Wittmann, Elsevier Science Publisher, Amsterdam, 1983, pp. 223-249.

38 Z.P. Bazant and L. Cedolin, "Blunt Crack Band Propagation in Finite Element Analysis," *Engineering Mechanics Division Journal*, ASCE, Vol. 105, No. EM2, April 1979, pp. 297-315.

39 Z.P. Bazant and L. Cedolin, "Fracture Mechanics of Reinforced Concrete," *Engineering Mechanics Division Journal*, ASCE, Vol. 106, 1980, pp. 1287-1306.

40 Z.P. Bazant and L. Cedolin, "Propagation of Crack Bands in Heterogeneous Materials," *Advanced in Fracture Research, Proceedings of 5th International Conference on Fracture*, Vol. 4, Cannes, 1981, pp. 1523-1529.

41 Z.P. Bazant, "Crack Band Model for Fracture of Geomaterials," *Proceedings of 4th International Conference on Numerical Methods in Geomechanics*, Held in Edmonton, Alberta, Canada, June 1982, Vol. 3, pp. 1137-1152.

42 Z.P. Bazant and L. Cedolin, "Finite Element Modeling of Crack Band Propagation," *Journal of Structural Engineering*, Vol. 109, No. 1, January 1983, pp. 69-92.

43 Z.P. Bazant and B.H. Oh, "Crack Band Theory for Fracture of Concrete," *Materials and Structures (RILEM)*, Vol. 16, 1983, pp. 155-177.

44 Z.P. Bazant, J.K. Kim, and P. Pfeiffer, "Determination of Nonlinear Fracture Parameters From Size Effect Tests," *Application of Fracture Mechanics to Cementitious Composites*, ed. S.P. Shah, Northwestern University, September 1984, pp. 143-169.

45 G. Pijaudier-Cabot and Z.P. Bazant, "Nonlocal Damage Theory," *Journal of Engineering Mechanics*, ASCE, Vol. 113, 1987, pp. 1512-1533.

46 Z.P. Bazant and T.-P. Chang, "Nonlocal Finite Element Analysis of Strain-Softening Solids," *Journal of Engineering Mechanics*, ASCE, Vol. 113, 1987, pp. 89-105.

47 Z.P. Bazant and F.-B. Lin, "Nonlocal Smeared Cracking Model for Concrete Fracture," *Journal of Structural Engineering*, ASCE, Vol. 114, 1988, pp. 2493-2510.

48 J. Rots, P. Nauta, G. Kusters, and J. Blaauwendraad, "Smeared Crack Approach and Fracture Localization in Concrete," *Heron*, V. 30, No. 1, 1985.

49 J. Rots, G. Kusters, and J. Blaauwendraad, "Strain-Softening Simulations of Mixed-Mode Concrete Fracture," *Fracture of Concrete and Rock*, ed. S.P. Shah and S.E. Swartz, June 1987.

50 R. de Borst, "Computational Aspects of Smeared Crack Analysis," *Constitutive Modeling of Concrete Structures*, Prineridge Press, Swansea, 1986.

51 D.S. Dugdale, "Yielding of Steel Sheets Containing Slits," *Journal of Mechanics*, Physics and Solids, Vol. 8, 1960, pp. 100-104.

52 G.J. Barenblatt, "The Mathematical Theory of Equilibribum Crack in the Brittle Fracture," *Advances in Applied Mechanics*, Vol. 7, 1962, pp. 55-125.

53 A. Hillerborg "A Model for Fracture Analysis," Lund Institute of Technology, Building Material Division, Report TVBM-3005, Lund, Sweden, 1978.

54 RILEM Recommendation, "*Determination of the* Fracture Energy of Mortar and Concrete by Means of Three-Point Bend Tests on Notched Beams," *Materials and Structures*, Vol. 18, No. 106, 1985, pp. 285-290.

55 A. Hillerborg, "The Theoretical Basis of a Method to Determine the Fracture Energy G_F of Concrete," *Materials and Structures*, Vol. 18, No. 106, 1985, pp. 291-296.

56 A. Hillerborg, "Results of Three Comparative Test Series for Determining tne Fracture energy G_F of Concrete," *Materials and Structures*, Vol. 18, No. 107, 1985, pp. 406-413.

57 S. Mindess, "The Effects of Specimen Size on the Fracture Energy of Concrete," *Cement and Concrete Research*, Vol. 14, 1984, pp. 431-436.

58 P.J. Gustafsson and A. Hillerborg, "Improvements in Concrete Design Achieved Through the Application of Fracture Mechanics," *Application of Fracture Mechanics to Cementitious Composites*, ed. S.P. Shah, Northwestern University , Sepetember 1984, pp. 487-500.

59 K. Visalvanich, and A.E. Naanman, "Fracture Model for Fiber Reinforced Concrete," *HERON*, Vol. 29, No. 2, 1984.

60 A.R. Ingraffea and W.H. Gerstle, "Non-Linear Fracture Models for Discrete Crack Propagation," *Application of Fracture Mechanics to Cementitious Composites*, ed. S.P. Shah, Northwestern University, September 1984, pp. 171-209.

61 H.W. Reinhardt, "Fracture Mechanics of an Elastic Softening Material Like Concrete," *HERON*, Vol. 29, No. 1984.

62 A. Carpinter A. Di Tommaso, and M. Fanelli, "Influence of Material Parameters and Geometry on Cohesive Crack Propagation," ed. F. Wittmann, *Fracture Toughness and Fracture Energy of Concrete*, 1985, pp. 117-135.

63 A. Carpinteri, G. Colombo, G. Giuseppetti, "Accuracy of the Numerical Description of Cohesive Crack Propagation," ed. F. Wittmann, *Fracture Toughness and Fracture Energy of Concrete*, 1985, pp. 189-195.

64 M. Wecharatana and W.J. Chiou, "Fracture Energy and the Complete Tensile Softening Response of Concrete," *Proceedings of the 1986 SEM Spring Conference on Experimental Mechanics*, New Orleans, pp. 23-30.

65 V.C. Li, "Fracture Resistance Parameters for Cementitious Materials and Their Experimental Determination," *Application of Fracture Mechanics to Cementitious Composites*, ed. S.P. Shah, 1985, pp. 431-449.

66 V.C. Li and E. Liang, "Fracture Process in Concrete and Fiber Reinforced Cementitious Composites," *ASCE Journal of Engineering Mechanics*, Vol. 112, 1986, pp. 566-586

67 V.C. Li, C. M. Chan, and K.Y. Leung, "Experimental Determination of the Tension-Softening Relations for Cementitous Composites," *Cement and Concrete Research*, Vol. 17, 1987, pp. 441-452.

68 J.E. Rice, "A Path Independent Integral and the Approximate Analysis of Strain Concentration by Notches and Cracks," *Applied Mechanics Journal*, ASME, Vol. 35, June 1968, pp. 379-386.

69 D.B. Barker, N.M. Hawkins, F.L. Jeang, K.Z. Cho, and A.S. Kobayashi, "Concrete Fracture in a CLWL Specimen," *Journal of Engineering Mechanics*, ASCE, Vol. 111, No. 5, May 1985, pp. 623-638.

70 K.Z. Cho, A.S. Kobayashi, N.M. Hawkins, D.B. Barker, and F.L. Jeang, "Fracture Process Zone of Concrete Cracks," *Engineering Mechanics Division Journal*, ASCE, Vol. 110, No. 8, August 1984, pp. 1174-1184.

71 A.S. Kobayashi, N.M. Hawkins, D.B. Barker, and B.M. Liaw, "Fracture Process Zone of Concrete," *Application of Fracture Mechanics to Cementitious Composites*, ed. S.P. Shah, Northwestern University, September, 1984, pp. 25-47.

72 Z.-K. Guo, N.M. Hawkins and A.S. Kobayashi, "Mixed Mode Concrete Fracture - An Experimental Analysis," Fracture Mechanics of Concrete Structure, ed. Z. Bazant, Elsevier Applied Sciences, 1992, pp. 695-700.

73 S. Mindess, "Rate Effects on the Fracture of Cementitious Materials," *Application of Fracture Mechanics to Cementitious Composites*, Northwestern University, September 1984, pp. 465-484.

74 F.H. Wittmann, "Influence of Time on Crack Formation and Failure of Concrete," *Application of Fracture Mechanics to Cementitious Composites*, Northwestern University, September 1984, pp. 443-464.

75 W. Suaris and S.P. Shah, "Mechanical Properties of Materials Under Impact and Impulsive Loading," *Concrete Structure Under Impact and Impulsive Loading, Interassociation (RILEM, CEB, IABSE, IASS) Symposium*, West Berlin, June 1982, pp. 33-62.

76 H.W. Reinhardt, "Strain Rate Effects on the Tensile Strength of Concrete as Predicted by Thermodynamic and Fracture Mechanics Models," *Cement-Based Composite: Strain Rate Effects on Fracture*, ed. S. Mindess and S.P. Shah, MRS Symposia proceedings, Vol. 64, 1986, pp. 1-20.

77 S.E. Swartz, L.W. Lu, L.D. Tang, and T.M. Refai, "Mode II Fracture Parameter Estimates for Concrete from Beam Specimens," *Experimental Mechanics*, Vol. 28, No. 2, 1988, pp. 146-153.

78 Y.S. Jenq and S.P. Shah, "Mixed Mode Fracture of Concrete," *International Journal of Fracture,* Vol 38, 1988, pp. 123-142.

79 Y.S. Jenq and S.P. Shah, "On the fundamental Issues of Mixed Mode Concrete Crack Propagation in Concrete," *Fracture of Concrete and Rock, Recent Developments*, eds. S.P. Shah, S.E. Swartz and B. Barr, Elsevier Appllied Science, 1989, pp. 27-38.

80 A. Castro-Montero, Z. Jia and S.P. Shah, "A Study of the Mixed Mode Fracture Using Disk Specimen," Fracture Mechanics of Concrete Structures, ed. Z. P. Bazant, Elsevier Appllied Science, 1992, pp. 701-706.

81 A.K. Maji, M.A. Tasdemir and S.P. Shah, "Mixed Mode Crack Propagation in Quasi-Brittle Materials," *Engineering Fracture Mechanics*, Vol. 38, No. 2/3, 1991, pp. 129-145.

82 M.A. Tasdemir, A.K. Maji and S.P. Shah, "Crack Propagation in Concrete Under Compressive," J. Eng. Mech. V. 116, no. 5, May 1990, pp. 1058-1076.

83 A. Carpinteri, G. Ferrara and G. Melchiorri, "Single Edge Notched Specimen Subjected to Four Point Shear: An Experimental Inverstigation," , pp. 605-614.

84 J.G.M. Van Mier, E. Schlangen and M.B. Nooru-Mohamed, "Shear Fracture in Cementitious Composites Part I: Experimental Observations," Fracture Mechanics of Concrete Structures, ed. Z. P. Bazant, Elsevier Appllied Science, 1992, pp. 659-670.

85 E. Schlangen and J.G.M. Van Mier, " Shear Fracture in Cementitious Composites Part II: Numerical Simulations," Fracture Mechanics of Concrete Structures. ed. Z. P. Bazant, Elsevier Appllied Science, 1992, pp. 671-676.

86 ASTM E23-86, "Notched Bar Impact Testing of Metallic Material," Annual Book of ASTM Standards, pp. 282-306, American Society for Testing and Materials, Philadephia, 1987.

87 H. Abe, H.C. Chandan, and R.C. Bradt, "Low Blow Charpy Impact of Silicon Carbides," *Bul. Amer. Cer. Soc.*, Vol. 57, No. 6, 1978, pp. 587-595.

88 A.P. Hibbert, "Impact Resistance of Fibre Concrete, " PhD dissertation, University of Surrey, 1977.

89 V.S. Gopalaratnam, S.P. Shah, and R. John, "A Modified Instrumented Charpy Test for Cement Based Composites," *Journal of Experimental Mechanics*, SEM, Vol. 24, 1984, pp. 102-111.

90 V.S. Gopalaratnam and S.P. Shah, "Properties of Steel Fiber Reinforced Concrete Subjected to Impact Loading," *Journal of the American Concrete Institute*, Vol. 83, 1986, pp. 117-126.

91 V.S. Gopalaratnam and S.P. Shah, "Strength, Deformation and Fracture Toughness of Fiber Cement Composites at Different Rates of Loading," eds. S.P. Shah and A. Skarendahl, *Steel Fiber Concrete*, Proceedings of U.S.-Sweden Seminar (NSF-STM), Elsevier Applied Science Publishers, U.K., 1986, pp. 299-331.

92 L.S. Costin, J. Duffy, and L.B. Freund, "Fracture Initiation in Metals Under Stress Wave Loading Conditions," ASTM STP 627, 1976, pp. 301-318.

93 J.R. Kelapckzko, "Application of the Split-Hopkinson Pressure Bar to Fracture Dynamics," *Proc. 2nd Conf. Mech. Prop. High Rates of Strain*, ed. J. Harding, Oxford, The Inst. of Phys., Vol. 45, 1979, pp. 201-204.

94 A. Marchand, J. Duffy, T.A. Christman and S. Suresh, "An Experimental Study of the Dynamic Mechanical Properties of an Al-SiCw Composite," *Engineering Fracture Mechanics*, Vol. 30, No. 3, 1988, pp. 295-315.

95 S. Suresh, T. Nakamura, Y. Yeshurun, K.-H. Yang, and J. Duffy, "Tensile Fracture Toughness of Ceramic Materials: Effects of Dynamic Loading and Elevated Temperature," *J. Am. Ceram. Soc.*, Vol. 73, No. 8, 1990.

96 H.W. Reinhardt, H.A. Kormeling, and A.J. Zielinski, "The Split Hopkinson Bar, a Versatile Tool for the Impact Testing of Concrete," *Materiaux et Constructions*, Vol. 19, 1986, pp. 55-63.

97 I. Jawed, G. Childs, A. Ritter, S. Winzer, T. Johnson, and D. Barker, "High-Strain-Rate Behavior of Hydrated Cement Pasts," *Cement and Concrete Research*, Vol. 17, 1987, pp. 433-440.

98 K. Kobayashi and R. Cho, "Flexural Behavior of Polyethylene Fibre Reinforced Concrete," *International Journal of Cement Composites and Lightweight Concrete*, Vol. 3, 1981, pp. 19-25.

99 J.-H. Yon, N.M. Hawkins and A.S. Kobayashi, "Strain Rate Sensitivity of Concrete Mechanical Properties," *Material Journal*, ACI Vol. 89, No. 2, 1992, pp. 146-153.

100 ACI Committee 544, "Measurement of Properties of Fiber Reinforced Concrete," *Journal of the American Concrete Institute*, Vol. 75, 1978, pp. 283-289.

101 A.S. Kobayashi and J.W. Dally, "Dynamic Photoelastic Determination of the a-K Relation for 4340 Alloy Steel," *Crack Arrest Methodology and Applications*, eds. G.T. Hahn and M.G. Kanninen, ASTM STP 711, 1980, pp. 189-210.

102 J.F. Kalthoff, J. Beinert, S. Winkler and W. Klemm, "Experimental Analysis of Dynamic Effects in Different Crack Arrest Test Specimens," *Crack Arrest Methodology and Applications*, eds. G.T. Hahn and M.F. Kanninen, ASTM STP 711, 1980, pp. 109-127.

103 D. Post, "Moire Interferometry," *Handbook on Experimental Mechanics*, ed. A.S. Kobayashi, Prentice Hall, Englewood Cliffs, NJ, 1987

104 J.S. Epstein, V.A. Deason, and W.G. Reuter, "Dynamic Moire Interferometry Studies of Stress Wave and Crack-Tip Diffraction Events in 1018 Steel," Fracture Mechanics: Nineteenth Symposium ASTM STP 969, ed. T.Z. Cruse, ASTM, Philadephia, 1988, pp. 482-503.

105 V.J. Parks, "Geometric Moire," *Handbook on Experimental Mechanics*, ed. A.S. Kobayashi, Prentice Hall, Englewood Cliffs, NJ, 1987.

106 A.S. Kobayashi, "Hybrid Experimental-Numerical Stress Analysis," *Handbook on Experimental Mechanics*, ed. A.S. Kobayashi, Prentice Hall, Englewood Cliffs, NJ, 1987.

107 K.B. Broberg, "The Propagation of a Brittle Crack," *Arkiv for Fysik*, Vol. 18, 1960, pp. 159-192.

108 L.B. Freund, "Crack Propagation in an Elastic Solid Subjected to General Loading-I. Constant Rate of Extension," *Jounal of the Mechanics of Physics and Solids*, Vol. 20, 1972, pp. 129-140.

109 C. Atkinson and J.D. Eshelby, "The flow of Energy into the Tip of a Moving Crack," *International Journal of Fracture Mech.*, Vol. 4, 1968, pp. 3-8.

110 Z.K. Guo, J.-H. Yon, N.M. Hawkins, and A.S. Kobayashi, "Fracture Energy Dissipation Mechanism of Concrete," To be published in *Fracture Mechanics*, 23rd Symposium, ASTM. (1992).

111 F. Erdogan and G.C. Sih, "On the Crack Extension in plates under plane loading and transverse shear," *J. Basic Eng.*, 85, 519-527 (1963).

112. Z.K. Guo, A Ph.D. dissertation to be submited to the University of Washington in August 1993.

APPENDIX A

VERIFICATION OF NODAL RELEASE MECHANISM

The nodal force releasing algorithm in the dynamic FEM model was checked by comparing the results with a known analytical solution for a crack propagating at a constant crack velocity in an infinite plate with an applied remote stress boundary condition. The dynamic energy release rate derived by Freund [156] is

$$G_D = g(V)G \tag{A-1}$$

where G_D is the dynamic energy release rate, G is its static counterpart, and g(V) is a universal function of crack speed, V. The latter function is given to a close approximation by

$$g(V) = 1 - \frac{V}{C_R} \tag{A-2}$$

where C_R is the Rayleigh wave velocity. Although this solution is derived for a crack in an infinite plate, the relation holds for a finite plate until the stress wave reflects back to the crack tip from the boundary.

Figure A-1 shows the mesh and boundary conditions of the verification model. The dynamic total work, strain energy and kinetic energy are directly computed in the FEM code. The dissipation energy is the difference between the total work and the sum of strain energy and kinetic energy. The static total work is calculated for a static crack with the same boundary conditions. Figure A-2 illustrates the energy partition with crack extension. Figure A-3 shows the energy rates by differentiating the curve in Figure A-2 for unit crack extension. The energy release rate curve, calculated directly from the dynamic FEM analysis, matched with the energy release rate computed from Eq. (28), until the stress waves reflected from the boundaries. This program validates the nodal force releasing mechanism of the dynamic FEM model.

ASK/cm/2/8/93

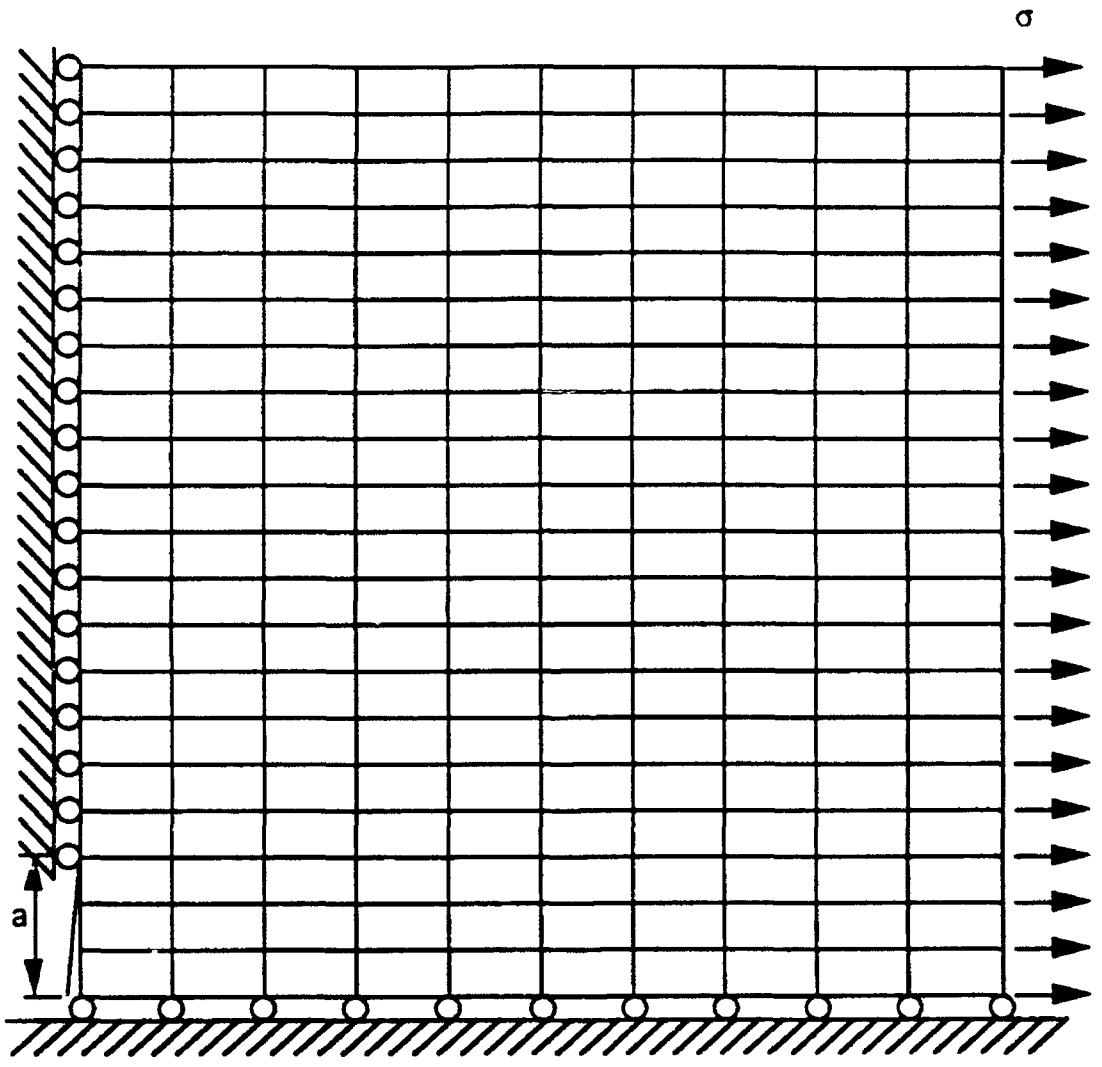

Figure A-1. Mesh and Boundary Conditions of Test Program.

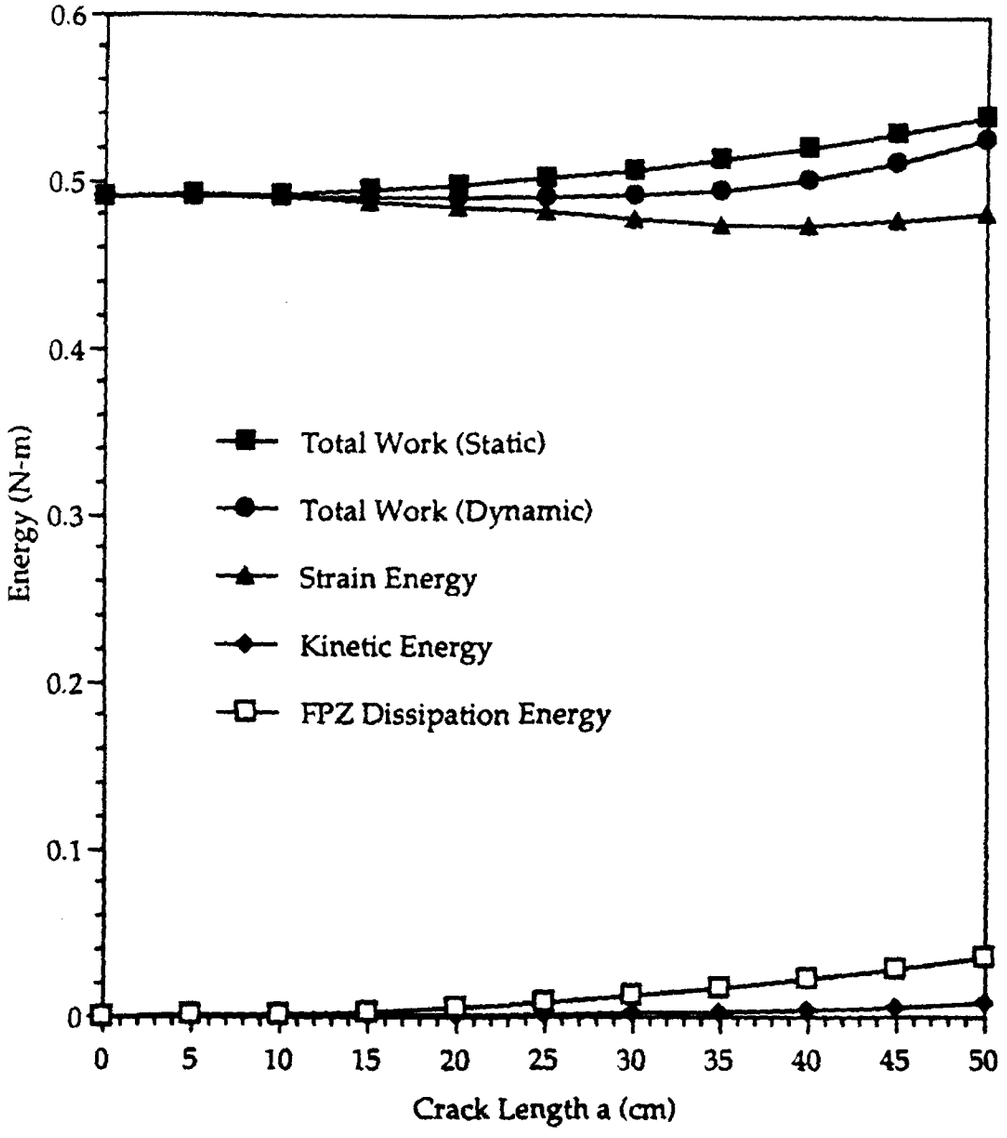

Figure A-2 Energy Partition of Verification Program.

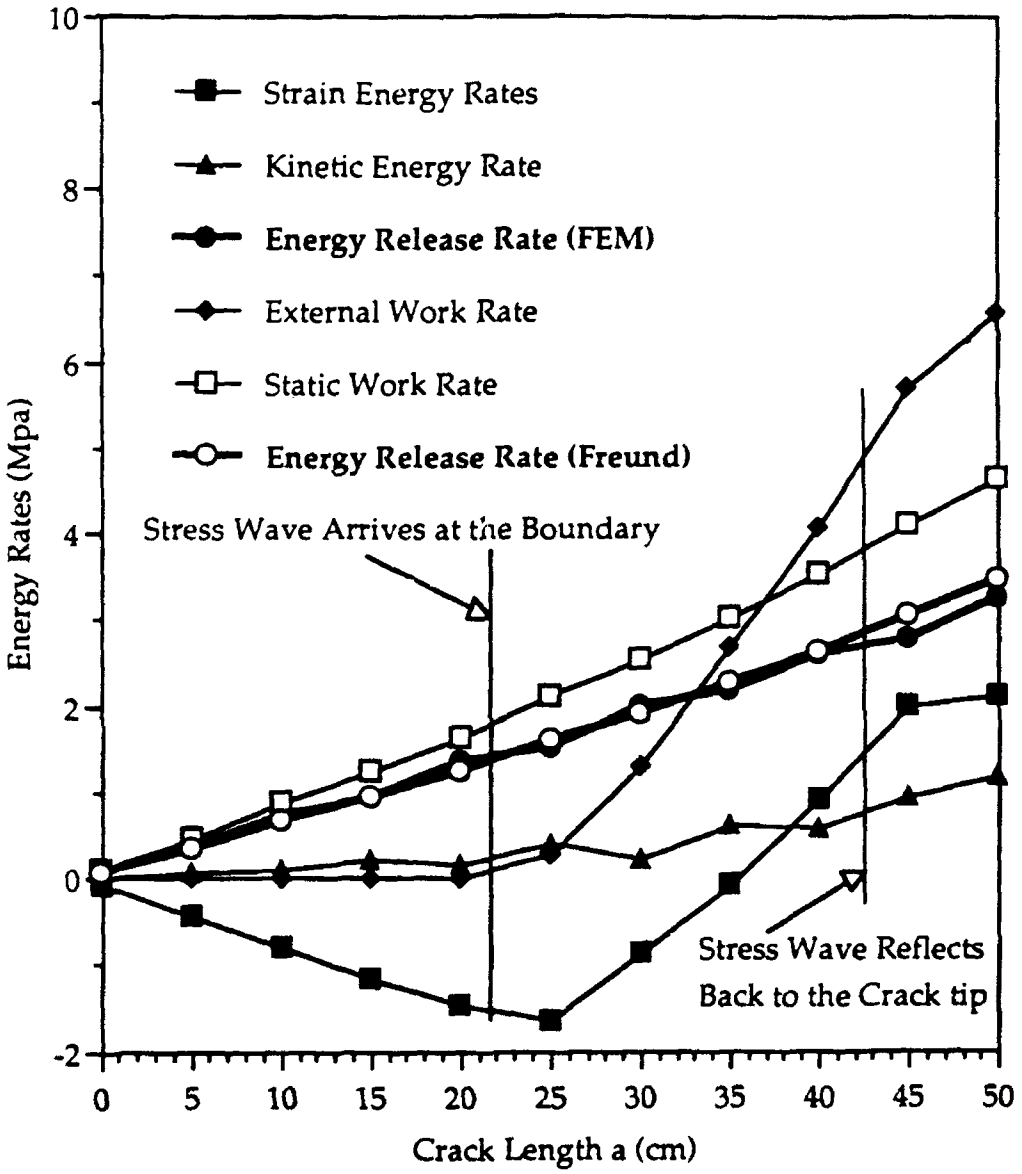

Figure A-3. Energy Rates for Verification Program.